Spring 5-3-2024

Optimization-based Integrated Voltage and Frequency Support for Microgrids using Energy Storage Systems

Niranjan Bhujel
niranjan.bhujel@maine.edu

OPTIMIZATION-BASED INTEGRATED VOLTAGE AND FREQUENCY SUPPORT FOR MICROGRIDS USING ENERGY STORAGE SYSTEMS

By

Niranjan Bhujel

A DISSERTATION

Submitted in Partial Fulfillment of the

Requirements for the Degree of

Doctor of Philosophy

(in Electrical Engineering)

The Graduate School

The University of Maine

May 2024

Advisory Committee:

Dr. Reinaldo Tonkoski, Advisor

Dr. Donald Hummels, Committee Chair

Dr. Yifeng Zhu, Professor at University of Maine

Dr. Timothy M. Hansen, Professor at South Dakota State University

Dr. Ujjwol Tamrakar, Senior Member of Technical Staff at Sandia National Laboratories

OPTIMIZATION-BASED INTEGRATED VOLTAGE AND FREQUENCY SUPPORT FOR MICROGRIDS USING ENERGY STORAGE SYSTEMS

By Niranjan Bhujel

Dissertation Advisor: Dr. Reinaldo Tonkoski

An Abstract of the Dissertation Presented
in Partial Fulfillment of the Requirements for the
Degree of Doctor of Philosophy
(in Electrical Engineering)
May 2024

Microgrids have emerged as a promising solution for ensuring the reliability and resilience of future grids, especially with the increasing integration of distributed energy resources (DERs) such as solar, wind, and energy storage systems (ESSs). However, this integration presents significant challenges in the dynamic control of voltage and frequency. Microgrids exhibit a distinctive characteristic marked by a high R/X ratio, resulting in voltage sensitivity to both active and reactive power, while frequency sensitivity is confined to active power. This unique attribute often leads to interference between voltage and frequency support schemes, potentially triggering protection mechanisms and causing localized or cascaded power outages.

To address these challenges, this dissertation introduces a novel approach based on moving horizon estimation (MHE), model predictive control (MPC), and droop control. MHE provides online estimates of microgrid parameters and dynamic states from noisy measurements, which then serve as inputs for MPC and droop control for the computation of reference inverter currents. The integrated MHE-MPC-droop framework is designed to provide dynamic voltage and frequency support, coupled with steady-state frequency support. Notably, the secondary controller ensures that steady-state frequency support is unnecessary, as it consistently maintains the frequency at the nominal value in steady-state conditions.

One of the strengths of the proposed approach lies in its flexibility, allowing for the tuning of performance based on specific requirements. The simulation study conducted on Cordova microgrid benchmark from Alaska demonstrates the effectiveness of this approach in providing near-optimal voltage and frequency support while accommodating the physical constraints inherent in ESSs. Different case studies show that the proposed approach reduces the voltage and frequency deviation as well as provide flexibility to prioritize different aspects of voltage and frequency support. Further, assessment of computational traceability shows that it is real-time applicable and robust against computational delay. The research contributes to the advancement of microgrid operations, particularly in the context of the growing penetration of renewable DERs. By mitigating the challenges associated with dynamic voltage and frequency control, the proposed approach offers a robust solution for achieving reliable and resilient microgrids of the future.

DEDICATION

In heartfelt dedication to my dearest mother, Pramila Bhujel, my revered father, Arjun Bhujel, and my cherished sister, Nima Bhujel. This journey would have remained elusive without their boundless love and unwavering support.

ACKNOWLEDGEMENTS

I extend my heartfelt appreciation to my esteemed research advisor, Dr. Reinaldo Tonkoski, for his unwavering guidance and invaluable insights throughout my Ph.D. journey. Without his mentorship, this dissertation would not have come to fruition.

I am also deeply grateful to Dr. Donald Hummels and Dr. Timothy Hansen for their keen interest in and valuable contributions to my work. Special thanks to Dr. Yifeng Zhu for his insightful guidance on specific aspects of my research. My sincere appreciation extends to Dr. Ujjwol Tamrakar for his consistent support and mentorship both during my Ph.D. studies and my internship at Sandia National Laboratories.

I am fortunate to have had the support of my peers and colleagues in the Electrical Engineering Departments of South Dakota State University and the University of Maine. Astha Rai from the University of Maine and Nischal Guruwacharya from South Dakota State University deserve special mention for their invaluable suggestions and assistance.

The success of this research endeavor was made possible through the generous support of the National Science Foundation under grant numbers #MRI-1726964, #OAC-1924302, and 2316399, as well as the U.S. Department of Energy under grant number #DE-SC0020281. I extend my gratitude to Sandia National Laboratories, Energy Storage Technology and Systems for hosting me as an intern during my Ph.D.

TABLE OF CONTENTS

DEDICATION iii

ACKNOWLEDGEMENTS iv

LIST OF TABLES xi

LIST OF FIGURES xii

LIST OF ABBREVIATIONS xv

1. INTRODUCTION 1

    1.1 Power Coupling in Microgrid and Multiple Timescales of Voltage-Frequency Dynamics 2

    1.2 Recent Trends and Voltage-Frequency Events 3

    1.3 Standard on Voltage-Frequency Limits on Microgrids 3

        1.3.1 Standards for grid-connected microgrid 4

        1.3.2 Standards for islanded/isolated microgrid 4

    1.4 Concept of Fast Voltage-Frequency Support 5

    1.5 Energy Storage Systems for Voltage-Frequency Support 6

    1.6 Motivation and Objectives 7

    1.7 Outline and Contributions 7

2. STATE OF THE ART VOLTAGE AND FREQUENCY SUPPORT 9

2.1 Chapter Objectives and Contributions 9

2.2 Approaches for Voltage and Frequency Support 9

2.2.1 Droop Based Control 9

2.2.2 PID Based Control 10

2.2.3 Reinforcement Learning Based 11

2.2.4 LQR and MPC Based Approach 13

2.3 Approaches for Combined Voltage-Frequency Support 15

2.4 State Estimator 16

2.5 Approaches for States and Parameter Estimation 17

2.5.1 Luenberger Observer 18

2.5.2 Kalman Filter 18

2.5.3 Extended Kalman Filter 20

2.5.4 Unscented Kalman Filter 20

2.6 Machine Learning Based State Estimator 22

2.7 Moving Horizon Estimation 22

2.8 Chapter Conclusions 23

3. MODEL DEVELOPMENT FOR MICROGRID VOLTAGE AND FREQUENCY DYNAMICS 24

3.1 Chapter Objectives and Contributions 24

3.2 Voltage Dynamics Model 24

3.2.1 Derivation 24

3.2.2 Validation 27

3.2.3 Time Constant of Voltage Dynamics 29
3.3 Frequency Dynamics Model 29
3.3.1 Derivation 30
3.3.2 Validation 31
3.3.3 Time Constant of Frequency Dynamics 33
3.4 Benchmark Description 33
3.5 Chapter Conclusions 34
4. MOVING HORIZON ESTIMATION BASED STATE AND PARAMETER ESTIMATION OF MICROGRIDS FOR VOLTAGE AND FREQUENCY DYNAMICS 36
4.1 Chapter Objectives and Contributions 36
4.2 Parameter Identifiability Analysis 37
4.3 Moving Horizon Estimation 38
4.3.1 General Formulation of MHE 39
4.3.2 Arrival Cost in MHE 40
4.3.3 Weight Selection in MHE 42
4.4 Implementation of MHE 44
4.5 State/Parameter Estimation for Voltage Dynamics 45
4.5.1 Simulation Setup 46
4.5.2 Results and Analysis 46
4.5.2.1 Identifiability Analysis 47
4.5.2.2 Weight Selection 47
4.5.2.3 States and Parameter Estimation 49

4.6 State/Parameter Estimation for Frequency Dynamics 49
4.6.1 Simulation Setup 49
4.6.2 Results and Analysis 50
4.6.2.1 Identifiability Analysis 50
4.6.2.2 Weight Selection 50
4.6.2.3 States and Parameter Estimation 51
4.6.2.4 Effects of Noise 52
4.7 Computational Tractability 53
4.8 Chapter Conclusions 54
5. MODEL PREDICTIVE CONTROL BASED DYNAMIC VOLTAGE SUPPORT 55
5.1 Chapter Objectives and Contributions 55
5.2 Proposed MHE-MPC Framework 56
5.3 Model Predictive Control 56
5.3.1 Formulation of MPC 57
5.3.2 Terminal Cost 59
5.3.3 External Controller 61
5.4 Simulation Setup 62
5.5 Results and Analysis 63
5.5.0.1 Performance of Voltage Support 63
5.5.0.2 External Dispatch Controller 65
5.5.1 Effects of Arrival Cost 65
5.5.2 Effects of Terminal Cost 66
5.5.3 Computational Performance 67

5.5.4 Effect of Computational Delay 67
5.6 Chapter Conclusions 68
6. INTEGRATED VOLTAGE-FREQUENCY SUPPORT FOR MICROGRIDS 69
6.1 Chapter Objectives and Contributions 70
6.2 Preliminary Study on Integrated Voltage-Frequency Support 70
6.3 Proposed Framework 72
6.4 Droop Control 72
6.5 Model Predictive Control 73
6.5.1 Steady State Voltage Behavior 73
6.5.2 Formulation of MPC 74
6.6 Simulation Setup 75
6.7 Results and Analysis 77
6.7.1 Design of Droop 77
6.7.2 Performance of Voltage-Frequency Support 77
6.7.3 Constraints Handling 79
6.7.4 Computational Performance 80
6.7.5 Effect of Computational Delay 80
6.8 Chapter Conclusions 80
7. CONCLUSIONS AND FUTURE RESEARCH DIRECTION 84
7.1 Conclusions 84
7.2 Future Research Directions 88
REFERENCES 89

LIST OF PUBLICATIONS DURING PH.D. STUDY 93

BIOGRAPHY OF THE AUTHOR 96

LIST OF TABLES

Table 3.1 Summary of generator parameters. 34

Table 6.1 Summary of the results 79

LIST OF FIGURES

Figure 1.1 Transition of the power system from synchronous generators-based resources towards converter-dominated. 2

Figure 1.2 Frequency/voltage standards for microgrid systems. 5

Figure 1.3 Block diagram representing the concept of Energy Storage System (ESS) based voltage-frequency support. 6

Figure 2.1 Generic droop curve for voltage/frequency support: a) linear droop curve b) droop with deadband and saturation. 9

Figure 2.2 Diagram representing basic of reinforcement learning. 12

Figure 2.3 Piecewise linear-elliptical droop curve. 15

Figure 2.4 Diagram representing loss calculation for neural state estimator. 22

Figure 3.1 Representation of grid by Thevenin equivalent model and ESS by controlled current source. 25

Figure 3.2 Simplified model used to validate the developed model. 27

Figure 3.3 Comparison of response from simulation model and mathematical model. 28

Figure 3.4 General diagram of the isolated power system illustrating the generator dynamics and the primary frequency control loop. 30

Figure 3.5 Simulink model used to validate the developed frequency dynamics model. 32

Figure 3.6 Comparison of response from Simulink generator model and mathematical model. 32

Figure 3.7 Modified benchmark from Cordova, Alaska. 34

Figure 4.1 Basic concept of Moving Horizon Estimation (MHE). 38

Figure 4.2 Setup of microgrid benchmark for V-MHE. 46

Figure 4.3 Estimation of state variables and estimated parameters. The time domain plot of state variables is shown whereas a histogram of estimated parameters is shown. 48

Figure 4.4 Setup of microgrid benchmark for F-MHE. 50

Figure 4.5 Estimation of state variables and estimated parameters. The time domain plot of state variables is shown whereas a histogram of estimated parameters is shown. 52

Figure 4.6 Estimation of state variables and estimated parameters when noise covariance is increased by 10 times. 53

Figure 5.1 Proposed MHE-MPC framework for voltage support. The MHE provides estimates of states and MPC provides ESS control signals. 56

Figure 5.2 Illustration of MPC concept. 57

Figure 5.3 Structure of external controller. 61

Figure 5.4 Simulation setup of MHE-MPC based dynamic voltage support. 62

Figure 5.5 Plot showing the performance of Model Predictive Control (MPC) under difference scenarios. Scenarios with different values of weight and limits on ESS currents are considered. 63

Figure 5.6 Response of voltage support for different value of external controller gain. 64

Figure 5.7 Performance of MPC when arrival cost is activated and deactivated. 66

Figure 5.8 Performance of MPC when terminal cost is activated and deactivated. 66

Figure 5.9 Plot showing effect of computational delay on the performance of voltage support. 67

Figure 6.1 Comparison of voltage and frequency support for different weighting parameters. 71

Figure 6.2 Proposed MHE-Droop-MPC framework for voltage support. The MHE provides estimates of states and MPC provides ESS control signals. 72

Figure 6.3 Simulation setup for integrated voltage and frequency support using droop and MPC on modified Cordova benchmark. 75

Figure 6.4 Root-locus plot for $G_d(s)$ and $G_q(s)$. 76

Figure 6.5 Comparison of voltage and frequency support for different cases (different weighting parameters) 81

Figure 6.6 Comparison of performance with unconstrained and constrained inverter currents. 82

Figure 6.7 Comparison of performance with computational delay. 83

LIST OF ABBREVIATIONS

ANN	Artificial Neural Network
BESS	Battery Energy Storage System
DER	Distributed Energy Resources
ERCOT	Electric Reliability Council of Texas
ESS	Energy Storage System
FERC	Federal Energy Regulatory Commission
KF	Kalman Filter
MSE	Mean Squared Error
MHE	Moving Horizon Estimation
MPC	Model Predictive Control
NERC	North American Reliability Corporation
NRMSE	Normalized Root Mean Square Error
RMSE	Root Mean Square Error
ROCOF	Rate of Change of Frequency
SI	Système International
UFLS	Under Frequency Load Shedding
pu	per unit
LQR	Linear Quadratic Regulator
FLC	Fuzzy Logic Control
NSE	Neural State Estimator
KF	Kalman Filter
PID	Proportional-Integral-Derivative

QP	Quadratic Programming
PCC	Point of Common Coupling
PLL	Phase Locked Loop
GGN	Generalized Gauss-Newton
QoS	Quality of Service
SoC	State of Charge

CHAPTER 1

INTRODUCTION

Microgrids have emerged as a promising solution to ensure the reliability and resilience of future power grids. They offer numerous advantages, including resilience, autonomous operation, enhanced efficiency, integration of renewable energy, and energy security. The popularity of microgrids has been on the rise. As of the beginning of 2023, the United States had installed 692 microgrids with a total capacity of 4.4 GW [1].

With the growing prevalence of converter-based generation in microgrids, the system's inertia and voltage sensitivity are subject to variation, depending on different grid configurations and the mix of generation. This variation has introduced challenges in controlling voltage and frequency. Synchronous generators are commonly employed in isolated or islanded microgrids to regulate the system's voltage and frequency. Additionally, Distributed Energy Resources (DERs), such as photovoltaic, wind, and Energy Storage Systems (ESSs), can serve as secondary support for voltage and frequency control. However, the large-scale integration of renewable DERs in a microgrid introduces several challenges in terms of dynamic voltage and frequency regulation.

Microgrids are distinct from conventional interconnected power systems in several aspects. These include size, feeder type, high cross-coupling between voltage and frequency dynamics [2], a potential high share of converter-based renewable sources, and low-inertia [3]. Traditionally, voltage and frequency controllers have been designed separately, under the assumption that the system's voltage and frequency dynamics are decoupled [4]. In contrast, microgrids are typically operated at low to medium voltage levels, resulting in a relatively high R/X ratio [5]. Moreover, due to the small size of microgrids, changes in the system voltage are often reflected as changes in the system load [2, 6, 3]. Compared to conventional grids, these factors result in a closer coupling between voltage and frequency dynamics in microgrids.

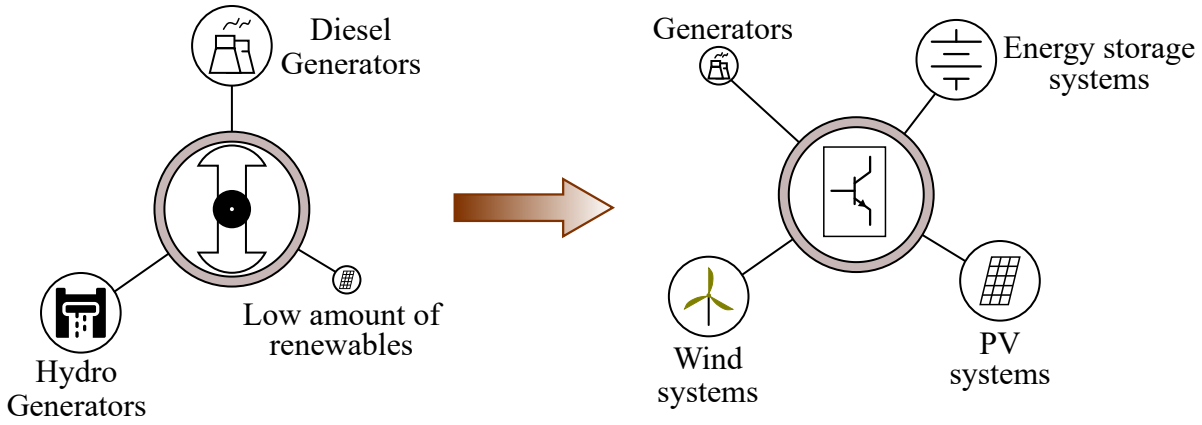

Figure 1.1. Transition of the power system from synchronous generators-based resources towards converter-dominated.

1.1 Power Coupling in Microgrid and Multiple Timescales of Voltage-Frequency Dynamics

Microgrids possess a unique characteristic where voltage and frequency are coupled via active power. The sensitivity of voltage to active power depends upon the R/X ratio, with a higher ratio leading to increased sensitivity as demonstrated in [7]. In a conventional power system, the R/X ratio is typically small, resulting in voltage being primarily sensitive to reactive power and frequency being sensitive to active power. This allows for the development of independent voltage and frequency support/control techniques. However, this does not apply to microgrids. Characterized by a high R/X ratio, microgrids exhibit voltage sensitivity to both active and reactive power, while frequency remains predominantly sensitive to active power. This presents a significant challenge to voltage and frequency support as they are coupled, rendering independent control/support techniques unsuitable. Furthermore, the timescales of voltage and frequency dynamics differ significantly. Voltage dynamics possess a time constant on the order of a few milliseconds, whereas frequency dynamics have a time constant on the order of a few seconds. Consequently, the time resolution (also referred to as step time or sample time) should be based on the time constant of voltage dynamics, and the time horizon should be based on the time constant of frequency dynamics. The number of timesteps in the integrated voltage-frequency support would be exceedingly large, leading to a substantial computational burden. Therefore, the classical approach

to developing/designing integrated controllers is no longer suitable for microgrids, necessitating a novel multi-timescale approach.

1.2 Recent Trends and Voltage-Frequency Events

Recent reports and studies have shown that voltage and frequency stability to be a matter of significant concern. Recently, there have been several power system outages reported due to frequency events in the power system. In some power systems, power quality issues have also been reported. For example, on August 9th, 2019 a power outage in Great Britain affected around 1 million people for 15-45 minutes [8]. Two large generation losses caused the frequency of the system to dip below the Under Frequency Load Shedding (UFLS) setting. This leads to more generation tripping (since protection schemes are designed to protect generation). This affected critical infrastructure like hospitals, rail transit systems, city traffic lights, etc. Similarly, in 28th September 2016, there was a power outage in Southern Australia that affected 850,000 people [9].

Honolulu rail transit system caused power quality issues in Honolulu, Hawaii, USA [10]. Power outages and brownouts were reported because bursts of power are required to start moving trains. This sudden burst of power causes instantaneous voltage to dip. One potential solution is to install STATCOM which is typically expensive.

1.3 Standard on Voltage-Frequency Limits on Microgrids

Microgrids can be operated in three modes: grid-connected, islanded, or isolated mode. In grid-connected mode, a microgrid is connected to the main grid. In this case, frequency is controlled by the main grid. Voltage is also controlled by the main grid up to a certain extent. Voltage variation due to line impedance and integration of renewables still exists. In islanded mode, the microgrid is disconnected from the main grid (in a planned or due to a fault in the main grid) whereas in the isolated mode of operation, the microgrid is designed to never be connected to the main grid. Regardless of whether the microgrid is in islanded or isolated mode, it needs to control its voltage and frequency since the microgrid does not receive any support from the main grid. Owing to their

smaller size and reduced inertia, they experience large frequency and voltage deviation that might be outside the standard limits compromising the stability of the system. Following are the existing standards for power systems:

1.3.1 Standards for grid-connected microgrid

The Electric Reliability Council of Texas (ERCOT) has defined specific parameters for frequency regulation in the power grid. The maximum allowable deadband, or the range within which the system frequency can fluctuate without triggering a response from the governors, is set at ±0.036 Hz. This means that the governors are required to respond when the system frequency deviates outside this range from the nominal value. In addition to this,ERCOT has also specified UFLS levels. These are set at 59.5 Hz, 58.9 Hz, and 58.5 Hz, corresponding to load shedding levels of 5%, 15%, and 25% respectively.

Similarly, the North American Reliability Corporation (NERC) recommends that the first stage of UFLS should be triggered within the frequency range of 59.5 Hz to 59.3 Hz. This highlights the importance of maintaining frequency stability in the power grid and the role of regulatory bodies in setting these standards.

The ERCOT and NERC recommend the voltage limits of 0.95 per unit (pu)-1.05 pu in the pre-contingency state. This limit is extended to the range 0.90 pu-1.10 pu for the post-contingency state. This wider range allows the system to accommodate the larger voltage fluctuations that can occur after contingency. Please note that the voltage limits are defined for steady-state operation. No standard limits are defined for dynamic voltage.

1.3.2 Standards for islanded/isolated microgrid

There are no specific standards defined for isolated/islanded microgrid systems. While IEEE 2030.7 provides specifications for microgrid controllers, it does not offer specific guidelines on the operation limits of microgrids. It merely recommends adhering to the one prescribed by grid codes. However, isolated/islanded microgrids often experience significant voltage and frequency excursions due to their standalone nature and the variability of renewable energy sources. These

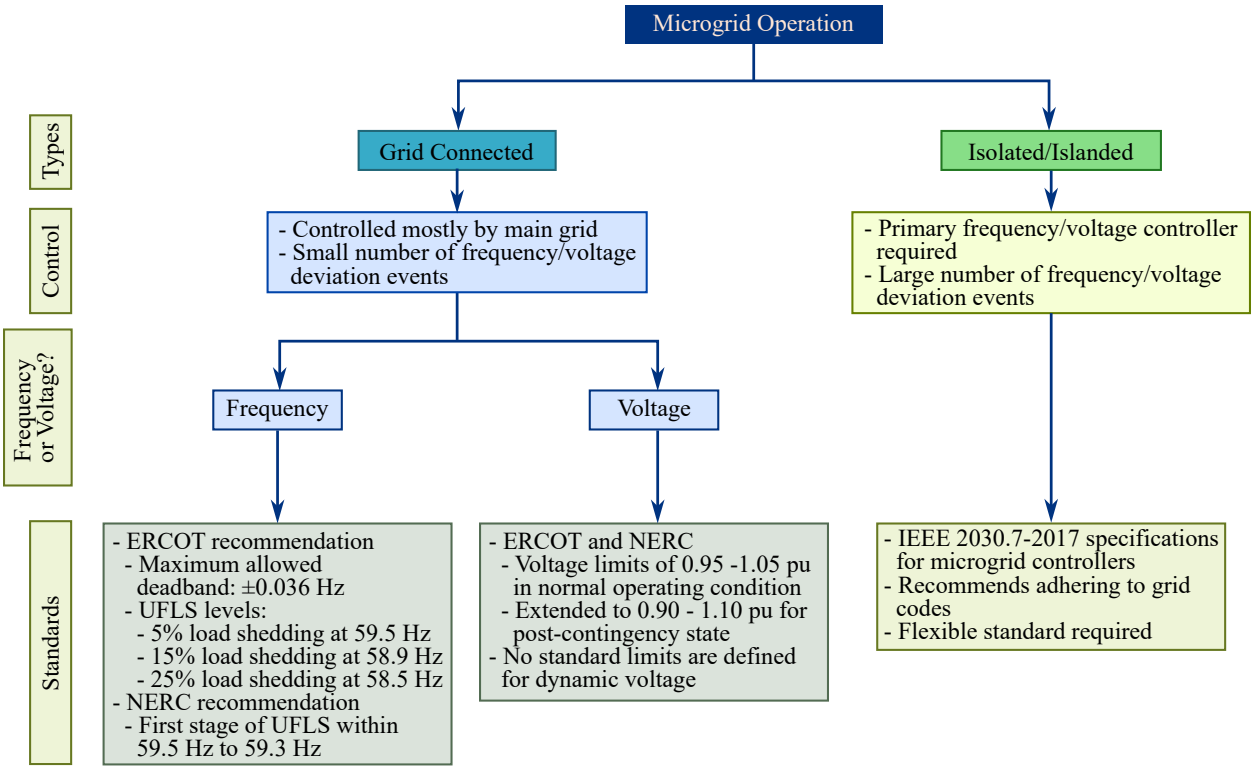

Figure 1.2. Frequency/voltage standards for microgrid systems.

fluctuations can exceed the standard limits set for grid-connected operations. Therefore, there is a need for more flexible standards that take into account the unique conditions of isolated microgrids. These standards should allow for larger voltage and frequency deviations compared to grid-connected systems, while still ensuring the stability and reliability of the microgrid. The development of such standards would require a thorough understanding of the dynamics of isolated microgrids, as well as extensive testing and validation to ensure their effectiveness and safety. It is an area that certainly warrants further research and development. The standards are summarized in Fig. 1.2.

1.4 Concept of Fast Voltage-Frequency Support

In any power system, fluctuations in power –due to changes in load, generation, or reconfiguration –result in deviations from the nominal voltage and frequency. Various mechanisms exist to counteract these deviations. However, these mechanisms are predominantly mechanical and thus

exhibit a slow response time. Despite their slow response, they are capable of restoring the system to its nominal state in steady-state conditions. Nevertheless, transient deviations can be substantial. In certain instances, these deviations may surpass the prescribed limits, triggering the protection scheme to disconnect various generators. This could potentially lead to system instability and, as previously discussed, a blackout.

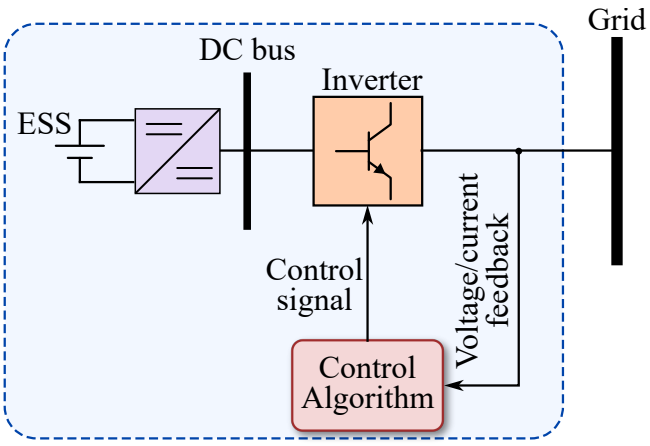

Figure 1.3. Block diagram representing the concept of ESS based voltage-frequency support.

The term 'fast voltage/frequency support' refers to the mechanism designed to minimize transient deviations. Given that the timescale of voltage dynamics is on the order of milliseconds, the support mechanism must be capable of adjusting power within this same timescale. A Battery Energy Storage System (BESS) is an optimal choice for this mechanism. Fig. 1.3 depicts a general block diagram of a BESS-based voltage-frequency support system.

1.5 Energy Storage Systems for Voltage-Frequency Support

ESS are versatile entities that can provide various ancillary services, including load leveling, energy arbitrage, voltage support, and frequency support, among others. These services operate on various timescales, each with its unique requirements and impacts on the ESS.

Services that operate on very short timescales, such as dynamic voltage support, and those on short timescales, like frequency support and steady-state voltage support, necessitate power exchanges in brief time intervals. This rapid exchange of power can significantly affect the

lifespan of an ESS, necessitating careful management and compensation strategies. Recognizing the importance of these services and the strain they place on ESS, the Federal Energy Regulatory Commission (FERC) has issued several orders, specifically FERC Order No. 755, 784, and 890. These orders permit ESS to participate in ancillary services, thereby acknowledging their crucial role in maintaining grid stability and reliability. Furthermore, these orders facilitate the creation of a market structure that compensates for these shorter timescales for ancillary services. This structure ensures that ESS are adequately compensated for their services, promoting their continued operation and contribution to grid stability.

1.6 Motivation and Objectives

Dynamic voltage-frequency support is a power-intensive service and might require large power demands and ramp rates from the energy source. The ESS should be able to operate in a fraction of the millisecond range. Further, ESS has physical constraints on maximum inverter currents and/or ramp rates.

The objective of this dissertation is to develop a dynamic voltage and frequency support along with a steady state voltage support framework for microgrids using ESS. The developed framework should be:

- *Flexible* to tune performance based on available resources
- *Able to incorporate physical constraints* of the ESS such as maximum currents, ramp rate limits, etc.
- *Adaptable* to change in microgrid parameters (line impedance, inertia, damping, etc)

1.7 Outline and Contributions

The dissertation is divided into three major chapters. **Chapter 2** introduces the basic concept of voltage and frequency support. A review of existing methods for voltage and frequency support is presented. A detailed comparison between different existing techniques is also presented.

Chapter 3 presents the development of a model that represents the voltage and frequency dynamics of microgrids. These models will be utilized in later chapters for state/parameter estimation and predictive control. Validation (partial) of developed models is also presented. **Chapter 4** introduces a novel mechanism for online estimation of microgrid parameters. The microgrid parameters may change with time based on the number of generations that are online. The estimate of microgrid parameters will allow for improved control strategy as well as protection schemes. Parameter identifiability analysis and design of perturbation signal for parameter estimation is also presented. **Chapter 5** presents MPC based dynamic voltage support for microgrids. The state and parameter estimation from chapter 4 is combined with MPC. Finally, **Chapter 6** presents droop control combined with MHE and MPC to provide dynamic voltage and frequency support along with steady state voltage support. Note that steady-state frequency support is not required since the secondary power controller takes care of steady-state frequency response. The conclusions of the dissertation are summarized in **Chapter 7**.

The main contributions of this dissertation are as follows:

- MHE based approach for online states and parameter estimation for microgrid voltage and frequency dynamics using noisy local measurements[11].
- MPC based approach to provide dynamic voltage support. The mechanism provides flexibility to provide desired performance as well as incorporate physical constraints within the control formulation[12].
- Droop-MHE-MPC based framework to provide dynamic voltage and frequency support and steady-state voltage support.

CHAPTER 2

STATE OF THE ART VOLTAGE AND FREQUENCY SUPPORT

Voltage-Frequency support is a combination of control algorithm, ESSs, and power electronics converter that absorbs/supplies power during the transient to reduce voltage and frequency deviation. For the voltage and frequency support, multiple possible control algorithms have been used in the real world and proposed in the literature.

2.1 Chapter Objectives and Contributions

The main objective of this chapter is to provide a detailed literature review of the current state-of-the-art voltage and frequency support approaches in power systems.

2.2 Approaches for Voltage and Frequency Support

In this section, different approaches for voltage and frequency support are discussed. It should be noted that some are applicable for either voltage or frequency support only.

2.2.1 Droop Based Control

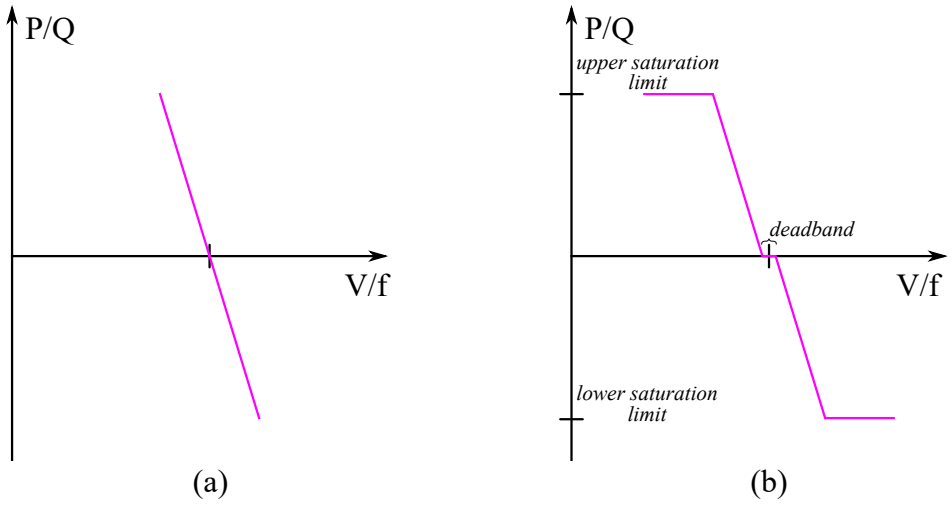

Figure 2.1. Generic droop curve for voltage/frequency support: a) linear droop curve b) droop with deadband and saturation.

Droop is the simplest control strategy for voltage and frequency support. The power injected into the grid is proportional to the control error in the voltage and frequency i.e.,

$$\Delta q = K_v(v_{ref} - v), \text{ and } \Delta p = K_\omega(\omega_{ref} - \omega). \tag{2.1}$$

In other words, droop control is a proportional controller. When there is a control error in the voltage or frequency, the proportional amount of power (active and reactive) is injected/absorbed. Since the powers cannot be zero when voltage/frequency support is required, the control error cannot be exactly zero. This is advantageous since this allows coordination between multiple resources without extra communication to provide voltage/frequency support. The disadvantages of this approach are

1. Less precise control: there is always steady-state control error which has to be eliminated by secondary control

2. Reduced system stability: with droop, there is not much flexibility for pole placement and as a result, might cause stability concern

3. Poor performance for non-linear and/or asymmetrical loads

Other than the above-mentioned disadvantages, they are designed assuming the voltage is affected by reactive power only and frequency is affected by active power only. This assumption becomes weak in the microgrid as voltage is affected by active power as well. As a result, both voltage and frequency support cannot be provided simultaneously by droop control only.

2.2.2 PID Based Control

Proportional-Integral-Derivative (PID) control-based approach has also been popular. In this approach, a control signal is given as:

$$u(t) = K_p e(t) + K_i \int e(t)dt + K_d \frac{de(t)}{dt}. \tag{2.2}$$

The controller gains K_p, K_i, and K_d are chosen based on the pole placement method or bode-plot method. Both approach requires a linear or linearized model of the system along with the

parameters. PID control provides greater accuracy as compared to just proportional (or droop) control as it has more flexibility (three tunable parameters). As compared to other advanced methods, the computational requirement is also low. The main disadvantages are:

1. Nonlinear systems: tuning nonlinear systems can be complex and in fact, might perform worse for highly nonlinear systems.

2. Adaptability issues: no inherent adaptability.

In [13], an adaptive way to adjust the K_p and K_i is proposed for frequency control of the islanded microgrids. An Artificial Neural Network (ANN) is used whose inputs are power changes, frequency deviation, etc and outputs are the value of K_p and K_i. The training of the ANN is done online such that Mean Squared Error (MSE) of the control error (frequency deviation) is minimized. After training, the values of K_p and K_i are updated online. In this approach, no voltage support is considered.

In [14], a model reference adaptive PID control-based approach for voltage control of islanded microgrid is proposed. In this approach, the model of a reference plant is considered. The reference plant refers to the plant whose response is used as a reference for real plants. The error between the response of the reference plant and the actual plant is used to adjust the gain of the controllers.

2.2.3 Reinforcement Learning Based

Reinforcement learning is the training of a model to make a sequence of decisions. The agent interacts with the environment to learn the control policy as shown in Fig. 2.2. The policy maps states of the environment to the control action. A reward is a scalar value that represents how the agent is performing. A reward is collected every time the agent interacts with the environment. Q-value, represented mathematically as $Q^{\pi}(s_t, a_t)$ represents the predicted value of an accumulated reward an agent would collect over the future when the agent takes action a_t at the current timestep and policy π thereafter. The agent learns to approximate the Q-value, which is often represented by a neural network. In RL, the objective is to maximize accumulated reward. Thus, the optimal

control action is:

$$a_t^* = \underset{a_t}{\text{argmax}}\, Q^{\pi}(s_t, a_t). \tag{2.3}$$

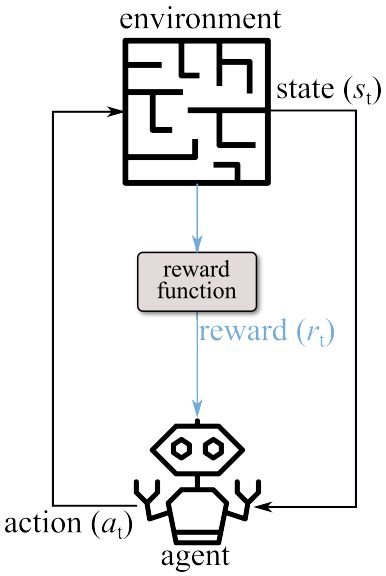

Figure 2.2. Diagram representing basic of reinforcement learning.

The main advantage of a reinforcement-learning approach is that it does not require a mathematical model of the system. This is useful when the system is complex and a simple mathematical model cannot accurately represent the system. The major drawbacks of reinforcement learning are:

- Sample inefficiency: they require a large number of samples to learn effectively
- Computationally intensive: The training process in reinforcement learning is computationally expensive
- Real-world training: they require interaction with the environment to learn which is challenging to perform safely in the real world. This becomes more of a concern in power systems where reliability and safety are of utmost importance.

In literature, several methodologies have been proposed that leverage reinforcement learning and adaptive dynamic programming. These methodologies involve learning from data without the

need for a predefined model. A notable drawback of this approach is the extensive interaction required between the agent and the system, the duration of which is contingent on the system's complexity.

The paper [15] employed a deep-deterministic policy gradient (DDPG) approach to tackle the voltage control problem in medium-voltage distribution networks. The DDPG methodology utilizes two neural networks: an actor network, which maps the system's state variables to a control variable, and a critic network, which predicts the future accumulated reward. The controller developed in this study is adaptive, enabling the agent to adjust its behavior in response to varying conditions. Similarly, [16] proposed a dynamic voltage support based on a soft actor critic. This approach was successful in reducing voltage deviation by a factor of 2.5 to 4.5 times and demonstrated computational efficiency post-training.

The paper in [17] proposed a reinforcement learning-based control scheme for optimal frequency synchronization in a lossy inverter-based microgrid. This scheme can be utilized to minimize frequency deviations across multiple inverters. In a similar vein, This paper [18] developed a fast frequency support based on a soft actor critic. This study also compared the performance of the soft actor critic-based approach with that of a Model Predictive Control (MPC). Although the soft actor critic-based approach reduced frequency deviation more than the MPC, the Rate of Change of Frequency (Rate of Change of Frequency (ROCOF)) was still larger compared to that of the MPC. Furthermore, due to the multi-timescale nature of frequency dynamics, the episode length was significantly large, leading to a substantial increase in training time.

However, to the best of my knowledge, no work has been done leveraging reinforcement learning based approach for integrated voltage and frequency support.

2.2.4 LQR and MPC Based Approach

Linear Quadratic Regulator (LQR) and MPC are popular model-based optimal control approach. In these approaches, a cost function is defined which is minimized over finite (or infinite horizon) subject to the mathematical model of the systems. For LQR, the cost function has to be quadratic

and the mathematical model to be linear. No other constraints are supported. The discrete-time LQR can be formulated as:

$$\min_{x_{0:N+1},\, u_{0:N}} \sum_{k=0}^{N-1} \left(x_k^\top Q x_k + u_k^\top R u_k + 2x_k^\top S u_k\right) + x_N^\top Q_N x_N \tag{2.4a}$$

subject to

$$x_{k+1} = Ax_k + Bu_k \;\; \forall\, k \in \{0, 1, ..., N-1\} \tag{2.4b}$$

where N represents horizon length of LQR. Since the cost is quadratic and is subject to only linear equality constraints, it is possible to get analytical solutions. The main advantage of this approach is that it is simple and computationally efficient. However, it is limited to linear systems and operational constraints cannot be imposed.

LQR based approach for frequency control has been proposed in the literature. In [19], LQR based virtual inertia is proposed. LQR was able to reduce frequency deviations and ROCOF when parameters are known accurately. When errors in the parameters were introduced, the performance was drastically compromised especially in terms of reducing ROCOF. In [20], LQR is compared with Fuzzy Logic Control (FLC) for load frequency control of three area power system. A state-space model of three area power system is developed which is used as a prediction model for LQR. However, there are always model uncertainties and disturbances. Thus, they propose fuzzy logic control. The paper concludes that LQR performs better in terms of most quality measures (percentage overshoot, energy consumption, etc). However, FLC performs better in terms of model uncertainties and disturbances.

MPC is another model based optimal control approach. MPC is very similar to LQR except MPC can handle nonlinear system as well along with physical constraints. In [21, 22], MPC based frequency control of low inertia power grids is proposed. The paper presents the performance of MPC at different values of weights. The paper also evaluates the effect of imposing physical constraints. The paper also proposes MHE based state and parameter estimation approach that can be used to make MPC adaptive with changing grid condition.

2.3 Approaches for Combined Voltage-Frequency Support

Historically, voltage and frequency support mechanisms have been designed independently. Specifically, voltage has been assumed to be influenced solely by reactive power, while frequency has been assumed to be affected exclusively by active power. In the study [23], a droop control method is utilized, wherein active and reactive power are employed to regulate frequency and voltage, respectively. Although this approach is suitable for conventional power systems, it is not applicable to microgrids. Similarly, in [24], a piecewise linear-elliptic droop control scheme is proposed for voltage and frequency support. The drooping curve of piecewise linear-elliptical droop is shown in Fig. 2.3. For smaller variations in voltage/frequency, the droop curve behaves as a linear droop. For large variations, an elliptical function is employed. Piecewise linear-elliptic droop control has performed better in terms of reduction of the voltage/frequency deviation as well as oscillations. However, in this paper as well, frequency support is achieved through active power only, and voltage support is achieved through reactive power only. The coupling is not considered and as a result, significant oscillation is still observed in the voltage and frequency response.

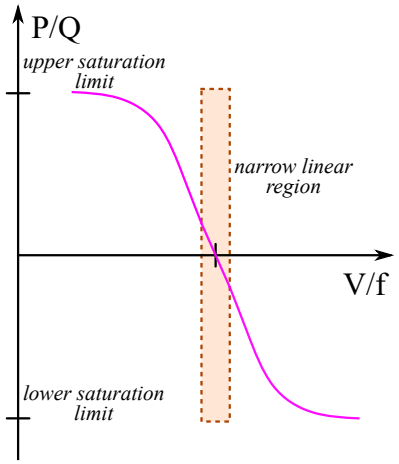

Figure 2.3. Piecewise linear-elliptical droop curve.

In the paper [2], a frequency control method based on voltage modulation is proposed. This method is particularly effective when the majority of the load power is sensitive to voltage deviations. However, a voltage-based frequency controller often interferes with a voltage controller, thereby complicating the simultaneous achievement of both controls.

In a more recent study [25], an integrated voltage and frequency support for microgrids based on Model Predictive Control (MPC) is proposed. The study demonstrates the feasibility of achieving simultaneous voltage and frequency control. Nevertheless, a significant challenge associated with this approach is the multi-timescale nature of the system. Given that the timescale of voltage dynamics is on the order of milliseconds and that frequency dynamics is on the order of seconds, the MPC will have an exceedingly large horizon length, which significantly increases computational time.

The above discussion regarding different existing approaches directs us to use MPC. However, because of large computational time, MPC cannot be used for dynamic voltage as well as frequency support. Thus, we propose to combine droop and MPC for dynamic voltage and frequency support. Droop control provides dynamic voltage support.

MPC requires a value of state variables at a given timestep which is not readily available. This is because not all state variables are directly measurable. Even if, in some cases, it is possible to measure all state variables, it might not be economical to put the sensor in the system for all state variables. Even if, in some cases, it is economical, the sensor still introduces some noise which needs to be filtered out. The state estimator provides an estimate of the state variable using input and output measurements of the system. Further, a state estimator can also be used to provide an online estimate of the parameters of the system. The following section provides a review of different approaches for state/parameter estimation.

2.4 State Estimator

State estimator usually combines two different information: measurement from the system and mathematical model of the system. Measurement represents actual behavior of the system and mathematical model represents how different state variable are related and how they evolve with time. However, neither of them are 100% accurate. Measurement is always corrupted by sensor noise. Similarly, mathematical model of the system is also approximated since simpler model are desired because of computational constraint. Thus, we consider following as mathematical model

for the dynamics and measurement of the system:

$$\boldsymbol{x}_{k+1} = \boldsymbol{f}(\boldsymbol{x}_k, \boldsymbol{u}_k) + \boldsymbol{w}_k \tag{2.5a}$$

$$\boldsymbol{y}_k = \boldsymbol{h}(\boldsymbol{x}_k) + \boldsymbol{v}_k \tag{2.5b}$$

where x_k, u_k, w_k and v_k represent state variable, input variable, error in dynamic model (process noise), and error in measurement (measurement/sensor noise) respectively.

When parameter estimations are also required, the following is used:

$$\boldsymbol{x}_{k+1} = \boldsymbol{f}(\boldsymbol{x}_k, \boldsymbol{u}_k, \boldsymbol{p}_k) + \boldsymbol{w}_k \tag{2.6a}$$

$$\boldsymbol{y}_k = \boldsymbol{h}(\boldsymbol{x}_k, \boldsymbol{p}_k) + \boldsymbol{v}_k \tag{2.6b}$$

such that $\boldsymbol{p}_{k+1} = \boldsymbol{p}_k + \bar{\boldsymbol{w}}_k$ (assumptions of constant parameters) where $\boldsymbol{p}$ represents parameters to be estimated and $\bar{\boldsymbol{w}}_k$ represents small allowed variablity in the parameter [26]. This allows the state estimator to be able to track changes in the parameters. Almost all of the state estimators are formulated considering the model of the form (2.5). There exists a way to transform the mathematical model of form (2.6) into form (2.6). This can be achieved by augmenting original states and parameters into a new state vector as $\tilde{\boldsymbol{x}}_k = \begin{bmatrix} \boldsymbol{x}_k & \boldsymbol{p}_k \end{bmatrix}^\top$ and augmenting original state equation with constantness of parameters as:

$$\tilde{\boldsymbol{x}}_{\boldsymbol{k+1}} = \begin{bmatrix} \boldsymbol{f}(\boldsymbol{x}_k, \boldsymbol{u}_k) + \boldsymbol{w}_k \\ \boldsymbol{p}_k + \bar{\boldsymbol{w}}_k \end{bmatrix} = \tilde{\boldsymbol{f}}(\tilde{\boldsymbol{x}}_k, \boldsymbol{u}_k) + \tilde{\boldsymbol{w}}_k \tag{2.7}$$

as shown in [27]. This allows us to use a state estimator formulated in the form (2.5) to estimate parameters as well. Further, we will assume that $\boldsymbol{w}_k$, $\bar{\boldsymbol{w}}_k$ and $\boldsymbol{v}_k$ follows Gaussian distribution with zero mean and covariance of $\boldsymbol{Q}_w$, $\bar{\boldsymbol{Q}}_w$ and $\boldsymbol{R}_v$ respectively.

2.5 Approaches for States and Parameter Estimation

Different types of state estimators have been discussed in the literature.

2.5.1 Luenberger Observer

The simplest one is the Luenberger observer. Luenberger observer requires a linear model of the system. Linearized form of (2.5) can be written as

$$\boldsymbol{x}_{k+1} = \boldsymbol{A}\boldsymbol{x}_k + \boldsymbol{B}\boldsymbol{u}_k \tag{2.8a}$$

$$\boldsymbol{y}_k = \boldsymbol{C}\boldsymbol{x}_k. \tag{2.8b}$$

Here, the effects of noises are ignored. The dynamics of the estimated variable are represented as

$$\hat{\boldsymbol{x}}_{k+1} = \boldsymbol{A}\hat{x}_k + \boldsymbol{B}\boldsymbol{u}_k + \boldsymbol{L}(\boldsymbol{y}_k - \hat{\boldsymbol{y}}_k) \tag{2.9a}$$

$$\hat{\boldsymbol{y}}_k = \boldsymbol{C}\hat{\boldsymbol{x}}_k \tag{2.9b}$$

where L represents observer gain. All variable with $\hat{\cdot}$ represents estimated corresponding variable. The error is defined as $e_k = \hat{x}_k - x_k$ from which error dynamics can be written as

$$\boldsymbol{e}_{k+1} = (\boldsymbol{A} - \boldsymbol{L}\boldsymbol{C})\boldsymbol{e}_k. \tag{2.10}$$

The error dynamics is an autonomous (no external input) linear system. This observer is stable if and only if all the eigenvalues of $A - LC$ are within the unit circle. If the observer is stable, the error e_k goes to zero in a steady state. Further, if there is no model mismatch (ideal scenario), the value of e_k remains at zero for all time once it reaches zero. However, in the real words, there is always some mismatch in the model, and hence, (2.10) will also have some extra residual term that acts like external input. Thus, the value of e_k does not necessarily stay at zero, and hence some error between true and estimated states variable should be expected.

2.5.2 Kalman Filter

[1] Kalman filter is an optimal state estimator that considers the effects of noises thus making it superior as compared to Luenberger observer. Linearized form of (2.5) can be written as

$$\boldsymbol{x}_{k+1} = \boldsymbol{A}\boldsymbol{x}_k + \boldsymbol{B}\boldsymbol{u}_k + \boldsymbol{w}_k \tag{2.11a}$$

$$\boldsymbol{y}_k = \boldsymbol{C}\boldsymbol{x}_k + \boldsymbol{v}_k. \tag{2.11b}$$

[1]The discussion of Kalman filter and its variants have been extracted from [28] where the candidate collaborated.

The KF operates recursively, i.e., it combines estimates from the previous discrete time with a prediction model and current discrete-time measurement to provide the estimate at the current discrete time. The process consists of two steps: the prediction step and the update step. In the prediction step, the states and their respective covariance (which are estimated at the previous discrete time instant) are passed through the state equation to compute the prior states and their covariance [29]. This occurs in the following two equations:

$$\hat{\boldsymbol{x}}_k^- = \boldsymbol{A}\hat{\boldsymbol{x}}_{k-1} + \boldsymbol{B}\boldsymbol{u}_{k-1} \tag{2.12a}$$

$$\hat{\boldsymbol{P}}_k^- = \boldsymbol{A}\hat{\boldsymbol{P}}_{k-1}\boldsymbol{A}^\top + \boldsymbol{Q} \tag{2.12b}$$

where at discrete time instant k (and $k-1$ indicates the previous timestep/estimate), $\hat{\boldsymbol{x}}_{k-1}$ and $\hat{\boldsymbol{P}}_{k-1}$ represent the previous estimated states and their covariance matrices, respectively, and $\hat{\boldsymbol{x}}_k^-$ and $\hat{\boldsymbol{P}}_k^-$ are the prior estimate of states and their covariance matrices, respectively.

In the update step, these prior states and their covariances are combined with the measurement to calculate the Kalman gain ($\boldsymbol{K}_k$). Using the Kalman gain, the posterior states and their covariance are calculated:

$$\boldsymbol{K}_k = \hat{\boldsymbol{P}}_k^-\boldsymbol{C}^\top(\boldsymbol{C}\hat{\boldsymbol{P}}_k^-\boldsymbol{C}^\top + \boldsymbol{R})^{-1} \tag{2.13a}$$

$$\hat{\boldsymbol{x}}_k = \hat{\boldsymbol{x}}_k^- + \boldsymbol{K}_k(\boldsymbol{y}_k - \boldsymbol{C}\hat{\boldsymbol{x}}_k^-) \tag{2.13b}$$

$$\hat{\boldsymbol{P}}_k = (\boldsymbol{I} - \boldsymbol{K}_k\boldsymbol{C})\hat{\boldsymbol{P}}_k^- \tag{2.13c}$$

where $\boldsymbol{I}$ is a unit identity matrix, and $\hat{\boldsymbol{x}}_k$ and $\hat{\boldsymbol{P}}_k$ are the estimate of posterior state and their covariance matrices, respectively. Because the Kalman filter is based on a Bayesian framework, which is a recursive process, the posterior states and their covariance are used as the prior time step states and covariance for the next step.

Because of its simplicity and yet effective estimation, Kalman Filter (KF) has been used in a lot of applications. In [30], KF was used to provide state estimates for MPC to provide frequency support in power systems. A simplified third-order model was used as a prediction model for KF and MPC. Similarly, in [31], the data-driven model is first developed and used as a prediction model for KF and MPC for fast frequency support.

2.5.3 Extended Kalman Filter

The extended Kalman filter is very similar to the Kalman filter. The nonlinear model is linearized to obtain the matrix A and C. The linearized equations are used except for (2.12b) and (2.13b) where original nonlinear equations are used.

2.5.4 Unscented Kalman Filter

The unscented Kalman filter uses an unscented transformation that allows us to estimate the result of applying a nonlinear transformation to a probability distribution. Unscented transformation uses a set of sigma points which are a set of deterministic points from a distribution. These sigma points are passed through a nonlinear function to get the resulting distribution. Since Gaussian distribution is assumed, estimating mean and covariance is sufficient since any Gaussian distribution can be completely characterized by its mean and covariance.

Let $(\cdot)^{(i)}$ represent the i^{th} column of a matrix, and $(\hat{\boldsymbol{\mathcal{X}}}_{k-1}) \in \mathbb{R}^{n_x \times (2n_x+1)}$ represent the matrices of sigma points. Then generate $2n_x + 1$ sigma points from $\hat{\boldsymbol{x}}_{k-1}$ as below [32, 27]:

$$\hat{\boldsymbol{\mathcal{X}}}_{k-1}^{(i)} = \begin{cases} \hat{\boldsymbol{x}}_{k-1} & \text{for } i = 0 \\ \hat{\boldsymbol{x}}_{k-1} + \left(\sqrt{\alpha^2(n_x+\kappa)}\hat{\boldsymbol{P}}_{k-1}{}^{1/2}\right)^{(i)} & \text{for } i = 1, 2, ..., n_x \\ \hat{\boldsymbol{x}}_{k-1} - \left(\sqrt{\alpha^2(n_x+\kappa)}\hat{\boldsymbol{P}}_{k-1}^{1/2}\right)^{(i-n_x)} & \text{for } i = n_x+1, n_x+2, ..., 2n_x \end{cases} \tag{2.14}$$

where α and κ are the parameters that determine the spread of sigma points around the mean value.

Now, these sigma points are transferred through (2.5) to obtain modified sigma points $\hat{\boldsymbol{\mathcal{X}}}_k^- \in \mathbb{R}^{n_x \times (2n_x+1)}$ for estimating prior states and its covariance matrix as:

$$\hat{\boldsymbol{\mathcal{X}}}_k^{(i)^-} = \boldsymbol{f}_{k-1}(\hat{\boldsymbol{\mathcal{X}}}_{k-1}^{(i)}, \boldsymbol{u}_{k-1}), \text{ for } i = 0, 1, ..., 2n_x \tag{2.15}$$

The prediction step from the prior KF type estimators is then replaced as:

$$\hat{\boldsymbol{x}}_k^- = \sum_{i=0}^{2n_x} w_m^{(i)} \hat{\boldsymbol{\mathcal{X}}}_k^{(i)^-} \tag{2.16}$$

$$\hat{\boldsymbol{P}}_k^- = \sum_{i=0}^{2n_x} w_c^{(i)} (\hat{\boldsymbol{\mathcal{X}}}_k^{(i)^-} - \hat{\boldsymbol{x}}_k^-)(\hat{\boldsymbol{\mathcal{X}}}_k^{(i)^-} - \hat{\boldsymbol{x}}_k^-)^\top + \boldsymbol{Q} \tag{2.17}$$

where

$$w_m^{(i)} = \begin{cases} 1 - \frac{n_x}{\alpha^2(n_x+\kappa)} & \text{for } i = 0 \\ \frac{1}{2\alpha^2(n_x+\kappa)} & \text{for } i = 1, 2, ..., 2n_x \end{cases} \tag{2.18}$$

$$w_c^{(i)} = \begin{cases} (2 - \alpha^2 + \beta) - \frac{n_x}{\alpha^2(n_x+\kappa)} & \text{for } i = 0 \\ \frac{1}{2\alpha^2(n_x+\kappa)} & \text{for } i = 1, 2, ..., 2n_x. \end{cases} \tag{2.19}$$

In the above equations, β is the parameter to incorporate prior knowledge of the distribution of the state. For a Gaussian distribution, β=2 is optimal, and $w_m^{(i)}$ and $w_c^{(i)}$ are the constant weights for calculation of mean and covariance, respectively [32].

Generate $2n_x + 1$ new sigma points $\hat{\boldsymbol{X}}_k \in \mathbb{R}^{n_x \times (2n_x+1)}$ from $\hat{\boldsymbol{x}}_k^-$ following the same procedure of generating sigma points as mentioned above. Propagate those sigma points through the measurement model below:

$$\hat{\boldsymbol{y}}_k^{(i)} = \boldsymbol{h}_k(\hat{\boldsymbol{X}}_k^{(i)}) \text{ for } i = 0, 1, ..., 2n_x \tag{2.20}$$

Compute prior mean $(\hat{\boldsymbol{m}}_k^-) \in \mathbb{R}^{n_y}$ and prior covariance $(\hat{\boldsymbol{S}}_k) \in \mathbb{R}^{n_y \times n_y}$ of the measurement, and then cross-covariance of states and measurement $(\hat{\boldsymbol{Z}}_k) \in \mathbb{R}^{n_x \times n_y}$ as below:

$$\hat{\boldsymbol{m}}_k^- = \sum_{i=0}^{2n_x} w_m^{(i)} \hat{\boldsymbol{y}}_k^{(i)} \tag{2.21}$$

$$\hat{\boldsymbol{S}}_k = \sum_{i=0}^{2n_x} w_c^{(i)} (\hat{\boldsymbol{y}}_k^{(i)} - \hat{\boldsymbol{m}}_k^-)(\hat{\boldsymbol{y}}_k^{(i)} - \hat{\boldsymbol{m}}_k^-)^\top + \boldsymbol{R} \tag{2.22}$$

$$\hat{\boldsymbol{Z}}_k = \sum_{i=0}^{2n_x} w_c^{(i)} (\hat{\boldsymbol{X}}_k^{(i)^-} - \hat{\boldsymbol{x}}_k^-)(\hat{\boldsymbol{y}}_k^{(i)} - \hat{\boldsymbol{m}}_k^-)^\top \tag{2.23}$$

The update step is replaced with:

$$\boldsymbol{K}_k = \hat{\boldsymbol{Z}}_k \hat{\boldsymbol{S}}_k^{-1} \tag{2.24}$$

$$\hat{\boldsymbol{x}}_k = \hat{\boldsymbol{x}}_k^- + \boldsymbol{K}_k(\boldsymbol{y}_k - \hat{\boldsymbol{m}}_k^-) \tag{2.25}$$

$$\hat{\boldsymbol{P}}_k = \hat{\boldsymbol{P}}_k^- - \boldsymbol{K}_k \hat{\boldsymbol{S}}_k \boldsymbol{K}_k^\top \tag{2.26}$$

2.6 Machine Learning Based State Estimator

Several methodologies that incorporate machine learning have been proposed in the literature. The primary advantage of these machine learning-based approaches is that they allow for the development of a state estimator without necessitating the system's model.

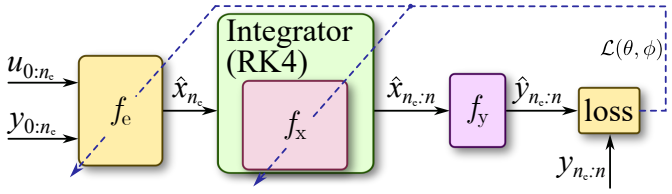

Figure 2.4. Diagram representing loss calculation for neural state estimator.

In [33], a Neural State Estimator (Neural State Estimator (NSE)) is proposed to estimate the states of power system frequency dynamics. The paper presents various scenarios where different levels of model information are available, including full information on the model and parameters, availability of the model but not the parameters, and unavailability of both the model and its parameters. The general block diagram of the NSE is depicted in Fig. 2.4.

The paper also conducts a comparative analysis of NSE and Moving Horizon Estimator (MHE) in terms of estimation accuracy and computation time. The study concludes that the performance of NSE and MHE is quite similar in terms of accuracy, but NSE is computationally more efficient. However, a significant drawback of NSE is that it requires data from the actual system with proper perturbation, and NSE must be trained offline initially to be utilized online.

2.7 Moving Horizon Estimation

The MHE is an optimization-based technique that utilizes the horizon of the most recent input and output measurements to estimate the states of a system. Unlike Kalman filters, MHE is capable of handling nonlinear systems and estimating parameters without state augmentation. Moreover, MHE allows for constraints to be imposed on estimated states and parameters, thereby enhancing stability compared to Kalman filters.

However, MHE necessitates more computational resources than Kalman filters, making it a viable choice only when the computational requirement can be justified. In [34], MHE was used for state and parameter estimation for power system frequency dynamics. Similarly, [11] employed MHE for states and parameter estimation for voltage and frequency dynamics of microgrids.

In a comparative analysis of different Kalman filters and moving horizon estimators for power system frequency dynamics conducted in [28], it was concluded that MHE outperforms Kalman filters in terms of estimation accuracy. Therefore, despite the larger computational requirements, MHE is employed in this work. Further details of MHE and a justification for its computational time are provided in the subsequent chapter.

2.8 Chapter Conclusions

This chapter provided a review of different existing methods of control and estimation encountered in power systems. A brief introduction of the approach along with its advantages and disadvantages were highlighted.

CHAPTER 3

MODEL DEVELOPMENT FOR MICROGRID VOLTAGE AND FREQUENCY DYNAMICS

The model of a power system plays a significant role in its study, stability analysis, etc. Utilizing MPC and MHE also requires a prediction model of the system. The prediction model should be simple so that the MPC and MHE problems can be solved in real-time. This chapter will be devoted to developing and validating a simplified prediction model of voltage and frequency dynamics of microgrids.

3.1 Chapter Objectives and Contributions

The main objective of this chapter is to develop a model of voltage and frequency dynamics. The specific contributions are:

- development of a model that represents voltage dynamics of microgrids
- development of a model that represents frequency dynamics of microgrids
- Validation (partial) of above developed models

3.2 Voltage Dynamics Model

The voltage dynamics model represents how voltage and related state variables vary with time. Voltage dynamics can have different timescales based on the source of variation. The changes in power (load/generation) may cause changes in variation via network dynamics, or via the response of the excitation system of the generation or there might be another source. In this work, the variation due to network dynamics is considered.

3.2.1 Derivation

Any complex power grid when observed from one bus, where an ESS is connected, can be represented by the Thevenin equivalent model as shown in Fig. 3.1 where R, L and v_{g} represents line

resistance, inductance, and Thevenin voltage respectively. Similarly, the ESS (which we assume has grid-following inverter) can be represented as a controlled current source with i_{inv} being the injected current and C being the capacitance of the inverter filter.

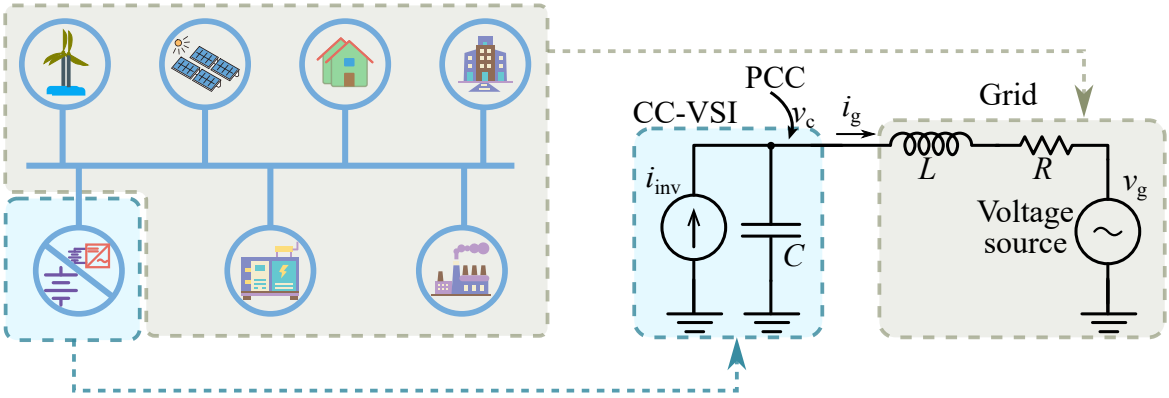

Figure 3.1. Representation of grid by Thevenin equivalent model and ESS by controlled current source.

Using Kirchhoff's current and voltage law, we can write the differential equation of the simplified model as :

$$\frac{di_{\text{g,abc}}}{dt} = \frac{v_{\text{c,abc}} - v_{\text{g,abc}} - i_{\text{g,abc}}R}{L} \tag{3.1a}$$

$$\frac{dv_{\text{c,abc}}}{dt} = \frac{i_{\text{inv,abc}} - i_{\text{g,abc}}}{C}. \tag{3.1b}$$

Any three phase quantity λ_{abc} can be transformed to dq0 frame as:

$$\lambda_{\text{dq0}} = T\lambda_{\text{abc}} \tag{3.2}$$

where $T = \frac{2}{3}\begin{bmatrix} \cos(\omega t) & \cos\left(\omega t - \frac{2\pi}{3}\right) & \cos\left(\omega t + \frac{2\pi}{3}\right) \\ -\sin(\omega t) & -\sin\left(\omega t - \frac{2\pi}{3}\right) & -\sin\left(\omega t + \frac{2\pi}{3}\right) \\ \frac{1}{2} & \frac{1}{2} & \frac{1}{2} \end{bmatrix}$ is the transformation matrix. Differentiating (3.2) with respect to time t, we get

$$\frac{d\lambda_{\text{dq0}}}{dt} = T\frac{d\lambda_{\text{abc}}}{dt} + \frac{dT}{dt}\lambda_{\text{abc}}. \tag{3.3}$$

Now, $\frac{dT}{dt}$ can be written as

$$\frac{dT}{dt} = \frac{2}{3}\omega \begin{bmatrix} -\sin(\omega t) & -\sin\left(\omega t - \frac{2\pi}{3}\right) & -\sin\left(\omega t + \frac{2\pi}{3}\right) \\ -\cos(\omega t) & -\cos\left(\omega t - \frac{2\pi}{3}\right) & -\cos\left(\omega t + \frac{2\pi}{3}\right) \\ 0 & 0 & 0 \end{bmatrix}$$

$$\frac{dT}{dt} = -\omega \begin{bmatrix} 0 & -1 & 0 \\ 1 & 0 & 0 \\ 0 & 0 & 0 \end{bmatrix} \frac{2}{3} \begin{bmatrix} \cos(\omega t) & \cos\left(\omega t - \frac{2\pi}{3}\right) & \cos\left(\omega t + \frac{2\pi}{3}\right) \\ -\sin(\omega t) & -\sin\left(\omega t - \frac{2\pi}{3}\right) & -\sin\left(\omega t + \frac{2\pi}{3}\right) \\ \frac{1}{2} & \frac{1}{2} & \frac{1}{2} \end{bmatrix}$$

$$\frac{dT}{dt} = -\omega T_r T \tag{3.4}$$

where

$$T_r = \begin{bmatrix} 0 & -1 & 0 \\ 1 & 0 & 0 \\ 0 & 0 & 0 \end{bmatrix}$$

is the 90° rotation matrix from d-axis to q-axis.

Substituting the value of $\frac{dT}{dt}$ in (3.3), we get

$$T\frac{d\lambda_{\text{abc}}}{dt} = \frac{d\lambda_{\text{dq0}}}{dt} + \omega T_r T \lambda_{\text{abc}}$$

$$T\frac{d\lambda_{\text{abc}}}{dt} = \frac{d\lambda_{\text{dq0}}}{dt} + \omega T_r \lambda_{\text{dq0}} \tag{3.5}$$

Now, we can multiply on both sides of (3.1) by T and use (3.5) to obtain

$$\frac{di_{\text{g,dq0}}}{dt} + \omega T_r i_{\text{g,dq0}} = \frac{v_{c,dq0} - v_{g,dq0} - i_{g,dq0}R}{L} \tag{3.6a}$$

$$\frac{dv_{\text{c,dq0}}}{dt} + \omega T_r v_{\text{c,dq0}} = \frac{i_{\text{inv,dq0}} - i_{\text{g,dq0}}}{C}. \tag{3.6b}$$

The above equation with some simplification can be written as:

$$\frac{di_{\text{gd}}}{dt} = -\frac{R}{L}i_{\text{gd}} + \omega i_{\text{gq}} + \frac{v_{\text{cd}}}{L} - \frac{v_{\text{gd}}}{L} \tag{3.7a}$$

$$\frac{di_{\text{gq}}}{dt} = -\omega i_{\text{gd}} - \frac{R}{L}i_{\text{gq}} + \frac{v_{\text{cq}}}{L} - \frac{v_{\text{gq}}}{L} \tag{3.7b}$$

$$\frac{dv_{\text{cd}}}{dt} = -\frac{i_{\text{gd}}}{C} + \omega v_{\text{cq}} + \frac{i_{\text{invd}}}{C} \tag{3.7c}$$

$$\frac{dv_{\text{cq}}}{dt} = -\frac{i_{\text{gq}}}{C} - \omega v_{\text{cd}} + \frac{i_{\text{invq}}}{C} \tag{3.7d}$$

The above equation can be converted to pu to obtain the following:

$$\frac{di_{gd}}{dt} = \omega_0 \left(-\frac{R}{L} i_{gd} + \omega i_{gq} + \frac{v_{cd}}{L} - \frac{v_{gd}}{L} \right) \tag{3.8a}$$

$$\frac{di_{gq}}{dt} = \omega_0 \left(-\omega i_{gd} - \frac{R}{L} i_{gq} + \frac{v_{cq}}{L} - \frac{v_{gq}}{L} \right) \tag{3.8b}$$

$$\frac{dv_{cd}}{dt} = \omega_0 \left(-\frac{i_{gd}}{C} + \omega v_{cq} + \frac{i_{invd}}{C} \right) \tag{3.8c}$$

$$\frac{dv_{cq}}{dt} = \omega_0 \left(-\frac{i_{gq}}{C} - \omega v_{cd} + \frac{i_{invq}}{C} \right) \tag{3.8d}$$

In (3.8), all the quantities are in pu except for ω_0 (nominal frequency in rad/s) which is in Système International (SI) unit.

3.2.2 Validation

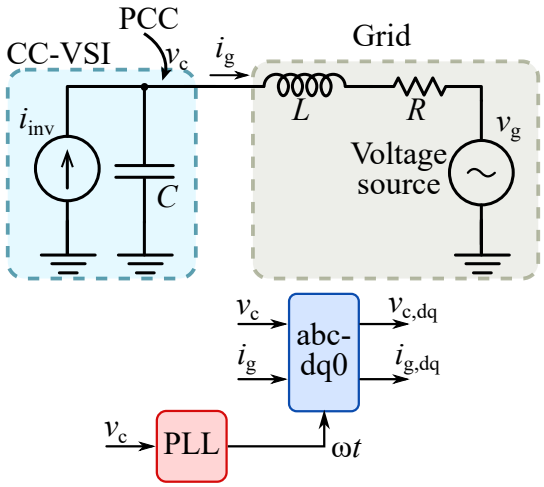

Figure 3.2. Simplified model used to validate the developed model.

To validate the developed voltage dynamics model, a simplified Thevenin model will be utilized in this chapter. A detailed model requires estimation of Thevenin equivalent parameters (impedance, voltage, etc) and hence, it will be validated in Chapter 4. We consider a model shown in Fig. 3.2 in MATLAB/Simulink simulation environment. The system being considered is assumed to be a 100 kVA, 208 V system. The value of R, L, and C are chosen to be 0.08 Ω, 0.22 mH and 220 μF respectively.

In order to access the dynamic performance of the model, the grid voltage v_g is perturbed with a step change (from 1.00 pu to 1.05 pu) at t=1 s. Further, d and q components of inverter current are perturbed with a step change (from 0.0 pu to 0.05 pu and from 0.0 pu to 0.10 pu respectively) at t=1.010 s and t=1.015 s respectively. Note that any reasonable random changes can be used to assess the accuracy of the model. Further, we will consider PCC voltage (v_c) as a reference to transform voltages and currents from abc to dq. The values of $v_{\text{g,dq}}$ and $i_{\text{inv,dq}}$ from the Simulink model were passed to the mathematical model to solve for i_{gd}, i_{gq}, v_{cd} and v_{cq}. Their comparison is shown in Fig. 3.3.

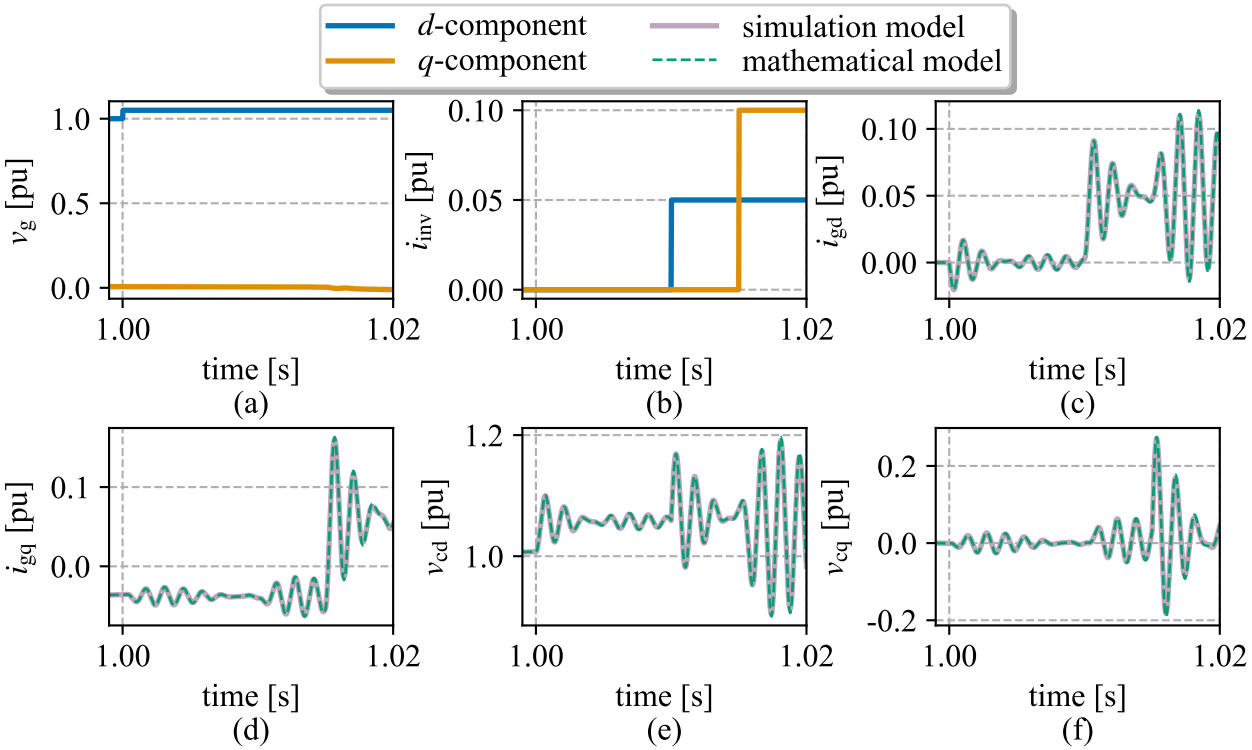

Figure 3.3. Comparison of response from simulation model and mathematical model.

To assess how close the mathematical model is to the Simulink model, Normalized Root Mean Square Error (NRMSE) is used which is given by

$$\text{NRMSE}(y) = \frac{\left\|y_{\text{true}} - y\right\|_2}{\left\|y_{\text{true}} - \text{mean}(y_{\text{true}})\right\|_2} \times 100\% \tag{3.9}$$

which calculates NRMSE of y against y_{true}. Using the formula, the NRMSE of i_{gd}, i_{gq}, v_{cd} and v_{cq} are found to be 2.58%, 2.50%, 3.97% and 4.99% respectively.

3.2.3 Time Constant of Voltage Dynamics

The time constant of a system gives important information about how fast or slow the dynamics are. It also provides a good idea of the magnitude of sample time to be used in the controller. In order to find the time constant of voltage dynamics, the eigenvalue of the state matrix of state equation (3.8) is required [25]. The time constant is the negative inverse of the real part of the eigenvalue. The state matrix from (3.8) is given by

$$A_{\mathrm{v}} = \omega_0 \begin{bmatrix} -\frac{R}{L} & \omega & \frac{1}{L} & 0 \\ -\omega & -\frac{R}{L} & 0 & \frac{1}{L} \\ -\frac{1}{C} & 0 & 0 & \omega \\ 0 & -\frac{1}{C} & -\omega & 0 \end{bmatrix}. \tag{3.10}$$

The eigenvalues of A_{v} is given by

$$\mathrm{eig}(A_v) = \omega_0 \left(-\frac{R}{2L} \pm \frac{\sqrt{R^2 - \frac{4L}{C} - 4\omega^2 L^2 \pm 4\omega L \sqrt{\frac{4L}{C} - R^2}}}{2L} \right). \tag{3.11}$$

Generally, $\frac{4L}{C} \gg R^2$, and thus the voltage dynamics time constant can be calculated by

$$T_{\mathrm{v}} = \frac{2L}{\omega_0 R}. \tag{3.12}$$

Note that R and L are in pu. For a typical value used in Subsection 3.2.2, we get a time constant value of 5.5 ms approximately. The formula also shows that a higher R/X ratio leads to a smaller time constant. For a R/X ratio of 5 (typical higher range), the time constant is approximately 1.06 ms.

3.3 Frequency Dynamics Model

The frequency dynamics of a power system refers to the changes in the frequency of the system when there is a change in power (load/generation). The inertia of the system is primarily responsible for maintaining the frequency of the system. Lower inertia corresponds to a higher frequency deviation. After inertia, the governor with droop control is responsible for maintaining

frequency. These controller response times are generally within 10 seconds. The secondary control also exists whose goal is to bring the frequency back to nominal value. This controller is very slow whose response time is in the order of a few tens of seconds to a few minutes.

3.3.1 Derivation

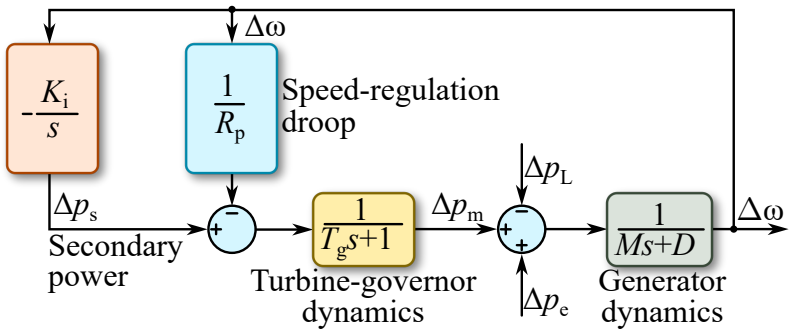

Figure 3.4. General diagram of the isolated power system illustrating the generator dynamics and the primary frequency control loop.

In a power system, multiple generators can be represented by a single generator with equivalent parameters. Consequently, the frequency dynamics of the power system can be modeled using the swing equation and the differential equation representing the turbine-governor dynamics, as illustrated in Fig. 3.4. The block diagram also includes a secondary power control loop; nevertheless, this secondary power control loop is disregarded, as our primary focus is on fast frequency support, and the dynamics of secondary power are considerably slower compared to inertial and droop responses. The following differential equations define the linearized frequency dynamics of the system:

$$M\dot{\Delta\omega} + D\Delta\omega = \Delta p_\mathrm{m} + \Delta p_\mathrm{e} - \Delta p_\mathrm{L} \tag{3.13a}$$

$$T_\mathrm{g}\dot{\Delta p}_\mathrm{m} + \Delta p_\mathrm{m} = \Delta p_s - R_\mathrm{p}^{-1}\Delta\omega \tag{3.13b}$$

$$\dot{\Delta p}_\mathrm{s} = -K_\mathrm{i}\Delta\omega \tag{3.13c}$$

where M, D, R_p, T_g and K_i represent the equivalent inertia, damping, droop coefficient, governor time constant, and secondary controller gain respectively. $\Delta\omega$, $\dot{\Delta\omega}$, Δp_m, Δp_e, and Δp_L represent

the frequency deviation, ROCOF, changes in mechanical power, ESS power, and load power. The above equations can be rearranged to obtain:

$$\frac{d\Delta\omega}{dt} = -\frac{D}{M}\Delta\omega + \frac{1}{M}\Delta p_{\mathrm{m}} + \frac{1}{M}\Delta p_{\mathrm{e}} - \frac{1}{M}\Delta p_{\mathrm{L}} \tag{3.14a}$$

$$\frac{d\Delta p_m}{dt} = -\frac{1}{R_{\mathrm{p}}T_{\mathrm{g}}}\Delta\omega - \frac{1}{T_{\mathrm{g}}}\Delta p_{\mathrm{m}} + \frac{1}{T_{\mathrm{g}}}\Delta p_{\mathrm{s}} \tag{3.14b}$$

$$\frac{d\Delta p_{\mathrm{s}}}{dt} = -K_{\mathrm{i}}\Delta\omega. \tag{3.14c}$$

Further, the dynamics of secondary power can be neglected as it is slower compared to inertial and governor response. Thus, we can set $\frac{d\Delta p_s}{dt} = 0$. Further, we define $\Delta p_m^* = \Delta p_m - \Delta p_s$. Then,

$$\frac{dp_m^*}{dt} = \frac{dp_m}{dt} - \frac{dp_s}{dt} = \frac{dp_m}{dt}. \tag{3.15}$$

Then (3.14) can be written as:

$$\frac{d\Delta\omega}{dt} = -\frac{D}{M}\Delta\omega + \frac{1}{M}\Delta p_{\mathrm{m}}^* + \frac{1}{M}\Delta p_{\mathrm{s}} + \frac{1}{M}\Delta p_{\mathrm{e}} - \frac{1}{M}\Delta p_{\mathrm{L}} \tag{3.16a}$$

$$\frac{d\Delta p_m^*}{dt} = -\frac{1}{R_{\mathrm{p}}T_{\mathrm{g}}}\Delta\omega - \frac{1}{T_{\mathrm{g}}}\Delta p_{\mathrm{m}}^* \tag{3.16b}$$

which can be rewritten as

$$\frac{d\Delta\omega}{dt} = -\frac{D}{M}\Delta\omega + \frac{1}{M}\Delta p_{\mathrm{m}}^* + \frac{1}{M}\Delta p_{\mathrm{e}} - \frac{1}{M}\Delta p_{\mathrm{L}}^* \tag{3.17a}$$

$$\frac{d\Delta p_m^*}{dt} = -\frac{1}{R_{\mathrm{p}}T_{\mathrm{g}}}\Delta\omega - \frac{1}{T_{\mathrm{g}}}\Delta p_{\mathrm{m}}^* \tag{3.17b}$$

where $\Delta p_L^* = \Delta p_L - \Delta p_s$. It should be noted that the value of Δp_L^* cannot be measured directly and hence should be treated as a disturbance.

3.3.2 Validation

To validate the developed frequency dynamics model, a detailed generator model from Simulink is considered. The generator has an inertia of 3.3 s, and a damping constant of 1.0. A governor with a time constant of 0.2 and droop control of $R_{\mathrm{p}} = 0.05$ are added. Finally, a secondary control of gain 2.0 is added. The generator is connected with a load of 0.7 pu which is connected to ESS. The value of the load is kept constant. Perturbation is created by active power injection via ESS. The perturbation signal is a square wave of 0.025 pu with a frequency of 0.5 Hz.

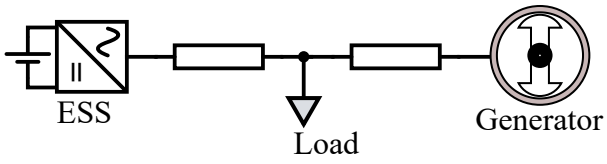

Figure 3.5. Simulink model used to validate the developed frequency dynamics model.

The response of the Simulink model is compared with the developed third and second-order models. The response of the mathematical model is very close to the Simulink model. The

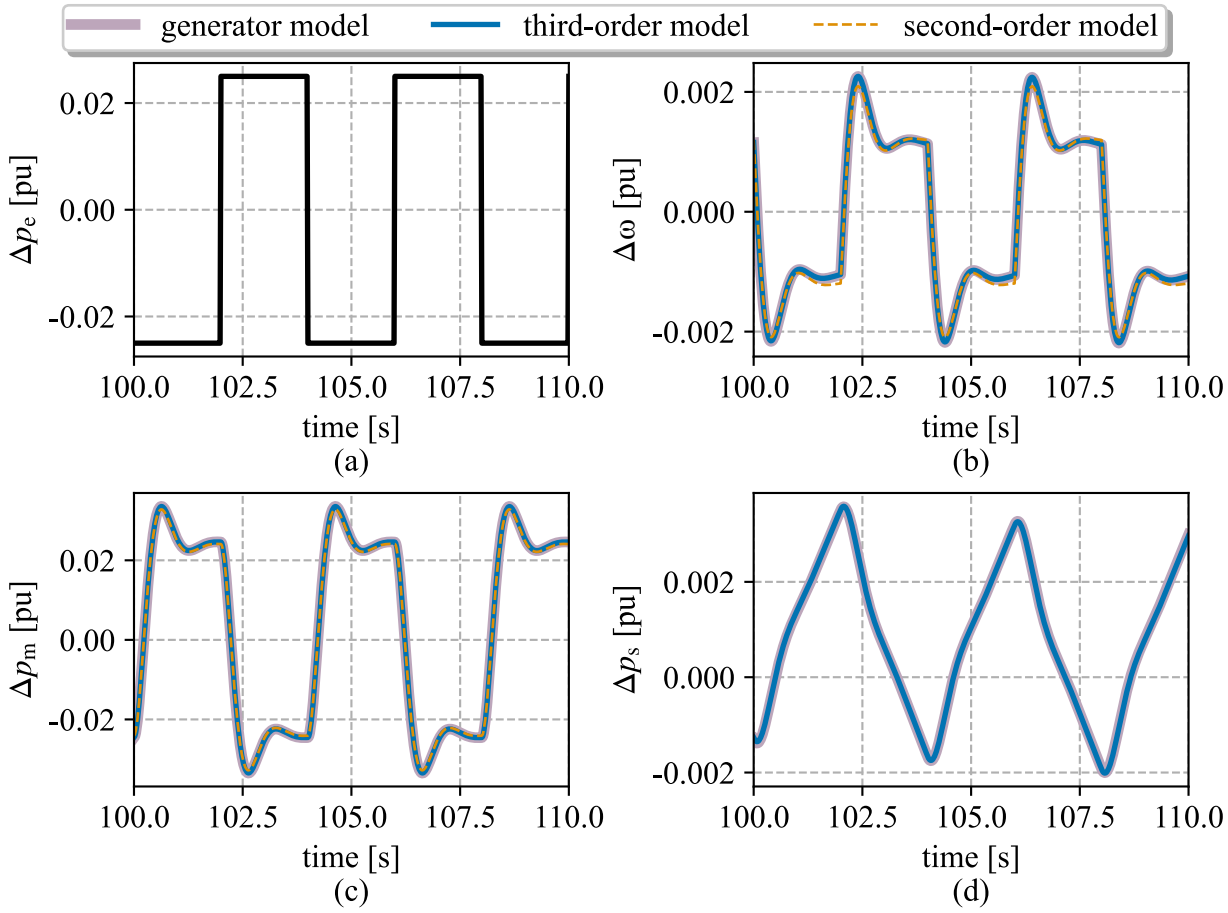

Figure 3.6. Comparison of response from Simulink generator model and mathematical model.

NRMSE of $\Delta\omega$ from third-order and second-order model with respect to Simulink model is 0.46% and 6.41%. The NRMSE of Δp_m from third-order and second-order models are 0.31% and 1.97%. The NRMSE of Δp_s from the third-order model is 0.87%. A slightly larger error is observed when the second-order model is used. This is because the dynamics of secondary power are neglected which introduces some error. Further, this error is expected to increase when the frequency of

perturbation is decreased. This is because at lower frequencies, dynamics of secondary power become more significant, and hence neglecting it causes larger errors. Since the second-order model performs satisfactorily, the second-order model will be used in the following chapters.

3.3.3 Time Constant of Frequency Dynamics

In order to find the time constant of frequency dynamics, the eigenvalue of the state matrix of state equation (3.17) is required. Since the secondary controller is slower in response, multiple time constants exist. Since we are interested in the smallest time constant, we can neglect the dynamics of secondary power. Then, the state matrix from (3.17) is given by

$$A_\omega = \begin{bmatrix} -\frac{D}{M} & \frac{1}{M} \\ -\frac{1}{R_p T_g} & -\frac{1}{T_g} \end{bmatrix}. \tag{3.18}$$

The eigenvalues of A_ω is given by

$$\text{eig}(A_\omega) = -\frac{D}{2M} - \frac{1}{2T_g} \pm \frac{\sqrt{D^2T_g^2 - 2MDT_g + M^2 - \frac{4MT_g}{R_p}}}{2MT_g} \tag{3.19}$$

The $\frac{4MT_g}{R_p}$ term within the square root is much larger than the other terms, allowing us to approximate the frequency dynamics time constant by

$$T_\omega = \frac{2MT_g}{M + DT_g}. \tag{3.20}$$

For a typical value used in Subsection 3.3.2, we get a time constant value of approximately 0.377 s.

3.4 Benchmark Description

This section will describe the simulation benchmark that will be used in the remaining chapter. The benchmark considered here is a modified Cordova benchmark from Alaska. Two substations are considered: ORCA and HBC. ORCA substation has a voltage level of 12.47 kV with four generators. HBC substation has a voltage level of 0.48 kV with three generators. A load of value P_L is connected along with another load of ΔP_L which can be switched on/off to create a step change in load. Finally, an ESS of size about 30% of total generation size is connected near the

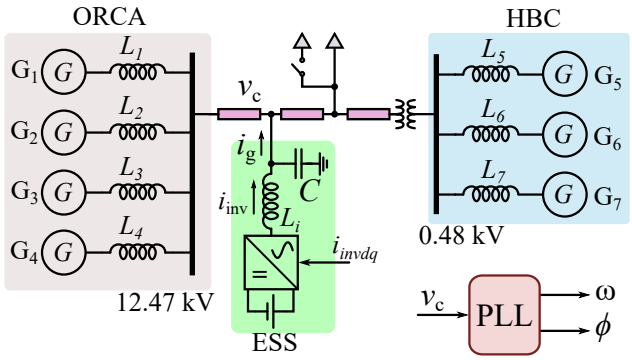

Figure 3.7. Modified benchmark from Cordova, Alaska.

ORCA substation. This ESS can be utilized to provide different types of grid ancillary services. The ESS also serves as creating perturbation in the system to estimate the system parameters as well as to provide voltage and frequency support. The voltage at the connection point of ESS (also known as Point of Common Coupling (PCC)), v_c is used as a reference voltage to calculate frequency and phase via Phase Locked Loop (PLL). The parameters of generators are summarized in Table 3.1. The droop coefficient and governor time constant are 0.05 and 0.2 s respectively for all generators.

Table 3.1. Summary of generator parameters.

Generators	M [s]	D	X_d [pu]	X'_d	X''_d	X_q	X'_q	X_l
G_1	1.88	1.0	1.38	0.227	0.12	0.76	0.120	0.1
G_2	1.88	1.0	1.38	0.227	0.12	0.76	0.120	0.1
G_3	3.3	1.0	1.76	0.46	0.248	1.06	0.248	0.05
G_4	3.3	1.0	1.76	0.46	0.248	1.06	0.248	0.05
G_5	6	0.3	1.20	0.22	0.20	0.8	0.20	0.16
G_6	6	0.3	1.20	0.22	0.20	0.8	0.20	0.16
G_7	6	0.3	1.20	0.22	0.20	0.8	0.20	0.16

3.5 Chapter Conclusions

In this chapter, the model for voltage and frequency dynamics was developed. The developed models were validated in the simulation environment, using NRMSE as an error metric to assess the accuracy of the developed models. The NRMSEs were found to be very small (less than 10%), demonstrating the efficacy of the developed models. Furthermore, mathematical expressions for

the time constants corresponding to the dynamics were derived from the developed models and calculated for typical values encountered in microgrids. Finally, the description of the benchmark is also provided which will be used in the following chapters.

CHAPTER 4

MOVING HORIZON ESTIMATION BASED STATE AND PARAMETER ESTIMATION OF MICROGRIDS FOR VOLTAGE AND FREQUENCY DYNAMICS

The increase of converter-based generation in power systems and microgrids is leading to a greater variation of power system parameters. This in turn makes the control of voltage and frequency more challenging. Furthermore, monitoring system states and parameters can be a valuable tool for microgrid operators to ensure stable and reliable operation. There is a need for the design of parameter and state estimators that operate under noisy conditions and that are subject to unknown disturbances. Microgrid parameter estimation is crucial for enabling optimal voltage and frequency control using Distributed Energy Resources (DER). The parameters of the microgrid can vary over time, such as during generation re-dispatch or commitment and microgrid reconfiguration. Additionally, sensor measurements are prone to noise. Using a low-pass filter could potentially filter out fast dynamic measurements. Thus, a robust states and parameter estimation method is necessary. In this work, MHE has been employed to perform state and parameter estimation. The proposed approach estimates the states, including frequency, rate of change of frequency, grid voltage, and current, as well as system parameters like inertia, damping, and equivalent impedance. The MHE is formulated as an optimization problem using data over a fixed past horizon and solved online, aiming to minimize the sum of the square of measurement noise and process noise.

4.1 Chapter Objectives and Contributions

The main objective of this chapter is to develop a state and parameter estimation framework for microgrid voltage and frequency dynamics. The specific contributions are:

- Parameter identifiability analysis for parameter estimation of the model developed in Chapter 3
- Moving horizon estimation framework to perform state and parameter estimation

4.2 Parameter Identifiability Analysis

Parameter identifiability analysis is a valuable tool to check necessary conditions on perturbation signals to be able to estimate the unknown parameters. Let $x \in \mathbb{R}^{n_x}$ be the state of the system, $u \in \mathbb{R}^{n_u}$ be the input to the system, $p \in \mathbb{R}^{n_p}$ be the unknown parameter of the system, and $y \in \mathbb{R}^{n_y}$ be the measurement output variable of the system. Let $f_c : \mathbb{R}^{n_x} \times \mathbb{R}^{n_u} \times \mathbb{R}^{n_p} \rightarrow \mathbb{R}^{n_x}$ and $h_c : \mathbb{R}^{n_x} \times \mathbb{R}^{n_p} \rightarrow \mathbb{R}^{n_y}$ are continuous-time state equation and output equation. Then, the system can be written as

$$\dot{x} = f_c(x, u, p) \tag{4.1a}$$

$$y = h_c(x, p). \tag{4.1b}$$

The observability matrix can be written as [35]

$$\mathcal{O} = \begin{bmatrix} \frac{\partial}{\partial \tilde{x}} h_c(x, p) \\ \frac{\partial}{\partial \tilde{x}} (L_{f_c} h_c(x, p)) \\ \frac{\partial}{\partial \tilde{x}} (L_{f_c}^2 h_c(x, p)) \\ \vdots \\ \frac{\partial}{\partial \tilde{x}} (L_{f_c}^{n_x+n_p-1} h_c(x, p)) \end{bmatrix} \tag{4.2}$$

where $\tilde{x} = [x^\top \ p^\top]^\top$ represents augmented state vector and $L_{f_c}^i h_c(\tilde{x}) = \frac{\partial L_{f_c}^{i-1} h_c(\tilde{x},u)}{\partial \tilde{x}} f_c(\tilde{x}, u) + \sum_{j=0}^{i} \frac{\partial L_{f_c}^{i-1} h_c(\tilde{x},u)}{\partial u^{(j)}} u^{(j+1)}$ represents the i^{th} Lie derivative of h with respect to $\tilde{x}$ along f, and $u^{(j)}$ represents j^{th} derivative of u with respect to t. The Lie derivative can be calculated recursively as [35]

$$L_{f_c}^i h_c(x, p) = \frac{\partial L_{f_c}^{i-1} h_c(x, p)}{\partial \tilde{x}} f_c(x, u, p) + \sum_{j=0}^{i-2} \frac{\partial L_{f_c}^{i-1} h(x, p)}{\partial u^{(j)}} u^{(j+1)} \tag{4.3}$$

with $L_{f_c} h_c(x, p) = \frac{\partial h_c(x,p)}{\tilde{x}} f_c(x, u, p)$. The system is fully observable (all states and parameters can be estimated) only if the rank of $\mathcal{O}$ is equal to the number of elements in $\tilde{x}$. If the matrix $\mathcal{O}$ is rank-deficit, then each column can be removed at a time, and the rank of the resulting matrix can be calculated to check which column does not contribute to the rank. The variable (state or parameter) that corresponds to the column that does not contribute to the rank of $\mathcal{O}$ is unobservable.

4.3 Moving Horizon Estimation

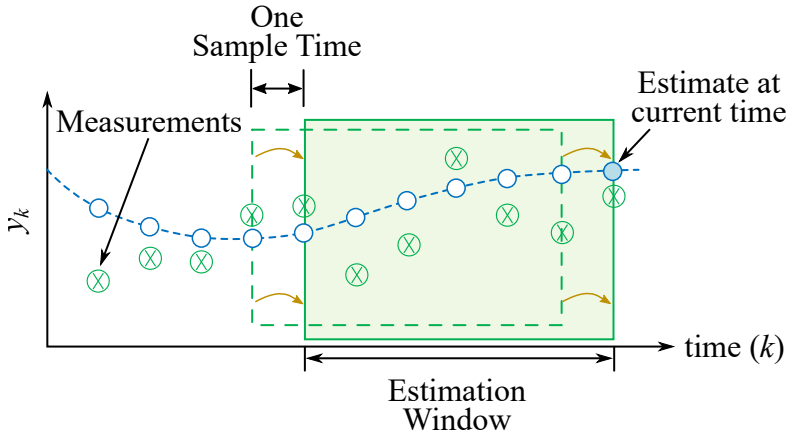

Figure 4.1. Basic concept of MHE.

MHE is an online optimization-based approach for states and parameter estimation. Past measurements over finite horizon are collected which are used to estimate states and parameters at the current discrete time. Recent developments in highly efficient Quadratic Programming (QP) solvers have made the real-time implementation of the MHE problem feasible [36]. The concept of MHE is illustrated in Fig. 4.1. The crosses ($\otimes$) represent the measurements from the system while the circles ($\circ$) represent the predicted system output based on the measurement and the prediction model. The measurement horizon is set to a fixed length of M i.e., the measurement from M discrete time instants are considered. At each discrete time, the optimization problem is solved that provides the estimate of states and parameters. At the next time-step, the window is moved forward i.e., the oldest measurement is discarded and the newest is added. Since the most recent data of fixed timesteps is considered, the information from the data behind the horizon window is completely lost. To solve this issue, arrival cost is used. Arrival cost is a technique to incorporate the information from data before the starting point of the window by using an approximate function. This allows us to estimate the state and parameters accurately even with smaller horizon lengths.

4.3.1 General Formulation of MHE

Let M represent the horizon length of the MHE. This M represents a number of past data measurements to be considered for estimation. Let us also define $\mathcal{L} = q - M$. If $\mathcal{H} = \{q - M, q - M + 1, ..., q\} = \{\mathcal{L}, \mathcal{L} + 1, ..., q\}$ represents the set of sampling instant, then MHE can be formulated as shown in eq. 4.4:

$$\min_{x_k, p} J_H = \phi_{\mathcal{L}}(x_{\mathcal{L}}) + \sum_{k=\mathcal{L}}^{q} \left\| y_k - h(x_k, p) \right\|_V^2 + \sum_{k=\mathcal{L}}^{q-1} \left\| w_k \right\|_W^2 \tag{4.4a}$$

subject to

$$x_{k+1} = f(x_k, u_k, p) + w_k \; \forall \; k \in \mathcal{H}/\{q\} \tag{4.4b}$$

$$p_{\min} \leq p \leq p_{\max} \tag{4.4c}$$

where $||a||_A^2 := a^\top A^\top A a$, $p_{\min}$ and $p_{\max}$ represents minimum and maximum possible value of parameters p. This $p_{\min}$ and $p_{\max}$ can also be used to force the parameters value. This is useful when we already have an estimation of parameters and want to perform state estimation only. The first term in the cost function i.e., $\phi_{\mathcal{L}}(\cdot)$ represents the arrival cost at sample instant q. Since we consider data from $k = \mathcal{L}, ..., q$ only, the data information from $k = 0, ..., \mathcal{L} - 1$ would be lost. Incorporating that data directly would increase the size of the optimization problem. Arrival cost is the technique to summarize the information contained in data from $k = 0, ..., \mathcal{L}$ with approximate function. The second term in the cost function represents the residual due to measurement noise and the third term represents the residual due to process noise where $V \in \mathbb{R}^{n_x \times n_x}$ and $W \in \mathbb{R}^{n_y \times n_y}$ represents their corresponding weights. The first constraint (4.4b) represents the discretized state equation of the system and the second constraint (4.4c) represents reasonable limits on the value of parameters. The solution to the above optimization problem gives the value of x_k and p which are the estimates of states and parameters and are respectively denoted by $\hat{x}_{k|q}$ and $\hat{p}_q$.

4.3.2 Arrival Cost in MHE

The objective of the arrival cost is to approximate the information contained in data from $k = 0, ..., q - \mathcal{L}$ i.e., to find the approximate representation of the following function:

$$\min \sum_{k=-\infty}^{\mathcal{L}} ||y_k - h(x_k, p_k)||_V^2 + \sum_{k=-\infty}^{\mathcal{L}-1} ||w_k||_W^2 \tag{4.5}$$

subject to

$$x_{\mathcal{L}} = f(x_{\mathcal{L}-1}, u_{\mathcal{L}-1}, p_{\mathcal{L}-1}) + w_{\mathcal{L}-1} \tag{4.6}$$

Different technique exists to approximate the above function. For a constrained estimation problem, it is nearly impossible to calculate the exact arrival cost. Thus, a lot of research has been focused on approximating the arrival by a suitable function that is computationally tractable. For example, extended Kalman filter-based approach has been proposed in [37]. Unscented Kalman filter-based implementation has been proposed in [38]. QR factorization-based approach is proposed in [26]. In this paper, we have used the method proposed in [26]. In this method, the arrival cost (4.5) is approximated by

$$\phi_{\mathcal{L}}(x_{\mathcal{L}}) = \left\| \begin{matrix} x_{\mathcal{L}} - \bar{x}_{\mathcal{L}} \\ p_q - \bar{p}_{\mathcal{L}} \end{matrix} \right\|_{P_{\mathcal{L}}}^2 . \tag{4.7}$$

Value of $\bar{x}_{\mathcal{L}}$ and $\bar{p}_{\mathcal{L}}$ gives estimation summary of states and parameters while $P_{\mathcal{L}}$ gives uncertainty in the estimation summary. The recursive update relation for $\bar{x}_{q-\mathcal{L}}$, $\bar{p}_{\mathcal{L}}$ and $P_{\mathcal{L}}$ is given in [26]. First, $f(\cdot)$ and $h(\cdot)$ are expanded as

$$f = \tilde{x} + X_x x_{\mathcal{L}} + X_p p_{\mathcal{L}} \tag{4.8}$$

$$h = \tilde{h} + H_x x_{\mathcal{L}} + H_p p_{\mathcal{L}} \tag{4.9}$$

where

$$X_x = \left.\frac{\partial f}{\partial x}\right|_{x=\hat{x}_{\mathcal{L}|q-1}, p=\hat{p}_{q-1}} ; X_p = \left.\frac{\partial f}{\partial p}\right|_{x=\hat{x}_{\mathcal{L}|q-1}, p=\hat{p}_{q-1}}$$

$$H_x = \left.\frac{\partial h}{\partial x}\right|_{x=\hat{x}_{\mathcal{L}|q-1}, p=\hat{p}_{q-1}} ; H_p = \left.\frac{\partial h}{\partial p}\right|_{x=\hat{x}_{\mathcal{L}|q-1}, p=\hat{p}_{q-1}}$$

We define a matrix $S \in \mathbb{R}^{(2n_x+2n_p+n_y)\times(2n_x+2n_p)}$ and vector $s \in \mathbb{R}^{2n_x+2n_p+n_y}$ as :

$$S := \left(\begin{array}{c|c} P_{\mathcal{L}} & 0 \\ -(VH_x \mid VH_p) & 0 \\ -\bar{W}\begin{pmatrix} X_x & X_p \\ 0 & \mathbb{I} \end{pmatrix} & \bar{W} \end{array}\right) \tag{4.10}$$

$$s := \begin{pmatrix} -P_{\mathcal{L}}\begin{pmatrix} \bar{x}_{\mathcal{L}} \\ \bar{p}_{\mathcal{L}} \end{pmatrix} \\ V(y_{\mathcal{L}} - \tilde{h}) \\ -\bar{W}\begin{pmatrix} \tilde{x} \\ 0 \end{pmatrix} \end{pmatrix} \tag{4.11}$$

where $\bar{W} = \begin{pmatrix} W & 0 \\ 0 & W_p \end{pmatrix}$ and $W_p \in \mathbb{R}^{n_p \times n_p}$ is the weight for parameter noise. Then, QR decomposition of S is taken i.e.,

$$\mathcal{Q}\mathcal{R} = S \tag{4.12}$$

where $\mathcal{Q}$ is unitary matrix and $\mathcal{R}$ is upper triangular matrix. Then,

$$\rho = \begin{pmatrix} \rho_1 \\ \rho_2 \\ \rho_3 \end{pmatrix} = \mathcal{Q}^\top s \tag{4.13}$$

$$\mathcal{R} = \begin{pmatrix} \mathcal{R}_1 & \mathcal{R}_{12} \\ 0 & \mathcal{R}_2 \\ 0 & 0 \end{pmatrix} \tag{4.14}$$

where $\rho_1, \rho_2 \in \mathbb{R}^{n_x+n_p}$, $\rho_3 \in \mathbb{R}^{n_y}$ and $\mathcal{R}_1, \mathcal{R}_2, \mathcal{R}_{12} \in \mathbb{R}^{(n_x+n_p)\times(n_x+n_p)}$. Then, arrival cost update can be written as

$$P_{\mathcal{L}+1} = \mathcal{R}_2 \text{ and } \begin{pmatrix} \bar{x}_{\mathcal{L}+1} \\ \bar{p}_{\mathcal{L}+1} \end{pmatrix} = -\mathcal{R}_2^{-1}\rho_2. \tag{4.15}$$

The recursive update (4.15) is used to update the arrival cost function every timestep.

4.3.3 Weight Selection in MHE

The proper value of weights in eq. (4.4a) i.e., V and W should be chosen to ensure good performance of MHE. These weights are based on errors in their corresponding term. Modeling error decides the value of W and measurement noise decides the value of V. Those weights are inverse of their corresponding noise i.e., $W = Q_w^{-1/2}$ and $V = R_v^{-1/2}$. The values of Q_w and R_v are not readily available. Thus, proper estimation of Q_w and R_v is required. We have used the autocovariance least square (ALS) estimation technique to estimate Q_w and R_v [39]. In this method, an observer is designed with the following as the error dynamics of the observer

$$\varepsilon_k = \bar{A}\varepsilon_{k-1} + \bar{G}\bar{w}_{k-1} \tag{4.16a}$$

$$\mathcal{Y}_k = y_k - C\hat{x}^- \tag{4.16b}$$

where $\hat{x}_k^- = A\hat{x}_{k-1} + Bu_{k-1}$, $\bar{A} = A - ALC$, $\bar{G} = [G, \ -AL]$, $\bar{w}_k = [w_k^\top, \ v_k^\top]^\top$ and G in this work is an identity matrix of dimension $n_x \times n_x$. Matrices A, B and C are state, input, and output matrices of the linearized model respectively. This observer does not need to be optimal; it only needs to be stable. Estimate of autocovariance of $\mathcal{Y}_k$ is calculated as

$$\widehat{\mathscr{C}}_j = \frac{1}{N_d - j} \sum_{i=1}^{N_d-1} \mathcal{Y}_i \mathcal{Y}_{i+j}^\top \tag{4.17}$$

where j represents lag and N_d represents the number of data. From the estimate of autocovariance for $j = 0, 1, ..., N-1$, autocovariance matrix (ACM) is created as

$$\widehat{\mathscr{R}}(N) = \begin{pmatrix} \widehat{\mathscr{C}}_0 & \dots & \widehat{\mathscr{C}}_{N-1} \\ \vdots & \ddots & \vdots \\ \widehat{\mathscr{C}}_{N-1}^\top & \dots & \widehat{\mathscr{C}}_0 \end{pmatrix} \tag{4.18}$$

where N is maximum lag chosen. For stationary data, autocovariance approaches zero at higher lag. Thus, value of N is chosen such that autocovariance at lag greater than N is non-significant.

The expression for autocovariances and hence, ACM can be derived from observer dynamics equation (4.16). The expression for ACM will be matrix with number of elements determined by the value of N. Thus equating $\widehat{\mathscr{R}}(N)$ with an expression of ACM results in N^2 number of equations which, generally, is greater than the total number of unknown elements in Q_w and R_v matrices. Hence, it is formulated as a least square optimization problem such that the sum of squares of difference in each of the equations is minimized. As shown in [39], the least square optimization problem can be written as

$$\min_{\mathscr{X}} \quad \left\| \mathscr{A}\mathscr{X} - \hat{b} \right\|_2^2 \tag{4.19}$$

where

$$\mathscr{A} = \left(D(G \otimes G) | D(AL \otimes L) + [\Psi \oplus \Psi + I_{n_y^2 N^2}] \mathscr{J}_{n_y,N} \right),$$

$$D = [(\mathscr{O} \otimes \mathscr{O})(I_{n_x^2} - \bar{A} \otimes \bar{A})^{-1} + (\Gamma \otimes \Gamma)\mathscr{J}_{n_x,N}],$$

$$\mathscr{O} = \begin{pmatrix} C \\ C\bar{A} \\ \vdots \\ C\bar{A}^{N-1} \end{pmatrix}, \Gamma = \begin{pmatrix} 0 & 0 & 0 & 0 \\ C & 0 & 0 & 0 \\ \vdots & \ddots & & \vdots \\ C\bar{A}^{N-2} & \dots & C & 0 \end{pmatrix},$$

$$\hat{b} = \text{vec}\left(\widehat{\mathscr{R}}(N) \right), \Psi = \Gamma \left[\bigoplus_{j=1}^{N} (-AL) \right],$$

$$\text{and } \mathscr{X} = \begin{pmatrix} \text{vec}(Q_w) \\ \text{vec}(R_v) \end{pmatrix}$$

The solution to optimization problem (4.19) gives estimates of Q_w and R_v which are denoted by $\widehat{Q}_w$ and $\widehat{R}_v$. Thus, $W = \widehat{Q}_w^{-1/2}$ and $V = \widehat{R}_v^{-1/2}$ are chosen as weights for MHE.

4.4 Implementation of MHE

MHE, when parameter estimations are involved, is generally a nonlinear optimization problem. Generalized Gauss-Newton (GGN) is a method to solve nonlinear optimization problems by transforming it into a sequence of quadratic problems. GGN solves the nonlinear problem of the following form:

$$\min_{r} ||J(r)||_2^2 \tag{4.20a}$$

subject to

$$G(r) = 0 \tag{4.20b}$$

$$H(r) \leq 0 \tag{4.20c}$$

where r is an unknown variable for which the problem needs to be solved. The problem (4.20) is solved successively with quadratic approximation. The approximated quadratic problem is

$$\min_{\Delta r_k} ||J(r_k) + \nabla_r J(r_k)^\top \Delta r_k||_2^2 \tag{4.21a}$$

subject to

$$G(r_k) + \nabla_r G(r_k)^\top \Delta r_k = 0 \tag{4.21b}$$

$$H(r_k) + \nabla_r H(r_k)^\top \Delta r_k \leq 0. \tag{4.21c}$$

The above problem is solved for Δr_k and r_k is updated as $r_{k+1} = r_k + \Delta r_k$. This process is continued till some termination criteria are reached (e.g., $||\Delta r_k||_2 < \epsilon$). With a good initial guess, the solution can be achieved in a very small number of iterations. In MHE, solutions from previous time steps can be shifted with one timestep to get an initial guess. This initial guess can be utilized to make the MHE computationally efficient.

The qpOASES solver is used to solve the optimization problem. The qpOASES solver solves the optimization problem of the following form:

$$\min_{z} \frac{1}{2} z^\top H z + g^\top z \tag{4.22a}$$

subject to

$$z_l \leq x \leq z_u \tag{4.22b}$$

$$a_l \leq Az \leq a_u. \tag{4.22c}$$

where z is an unknown variable for which the optimization problem has to be solved. It should be noted that only inequality constraint is supported in qpOASES directly. Equality constraint can be written as inequality constraint with equal upper and lower bounds. The qpOASES is used to solve the optimization problem (4.21) with following:

$$z := \Delta r_k \tag{4.23}$$

$$H := 2\nabla_r J(r_k)^\top \nabla_r J(r_k) \tag{4.24}$$

$$g := 2\nabla_r J(r_k)^\top J(r_k). \tag{4.25}$$

Constraints can be rewritten accordingly. The important part is the computation of jacobians ($\nabla_r J(r_k)$, $\nabla_r G(r_k)$, etc). CasADi [40] offers algorithmic differentiation which can be utilized to compute the jacobians. Further, CasADi offers C-code generation which makes the computation of Jacobians efficient. It should be noted that this approach can be used for MPC as well.

4.5 State/Parameter Estimation for Voltage Dynamics

MHE for voltage dynamics (named 'V-MHE') will be discussed in this section. For state and parameter estimation of voltage dynamics of microgrids, the model developed in Chapter 3 for voltage dynamics is used. The Runge-Kutta method of order 4 is used to discretize the state equation (3.8). The state variables are $x = \begin{bmatrix} i_{gd} & i_{gq} & v_{cd} & v_{cq} \end{bmatrix}^\top$ and input variables are $u = \begin{bmatrix} i_{invd} & i_{invq} \end{bmatrix}^\top$. The unknown parameters to be estimated is $p = \begin{bmatrix} R & L & v_{gd} & v_{gq} \end{bmatrix}^\top$. Further,

all four state variables are measurable. Thus,

$$h(x, p) = x. \tag{4.26}$$

4.5.1 Simulation Setup

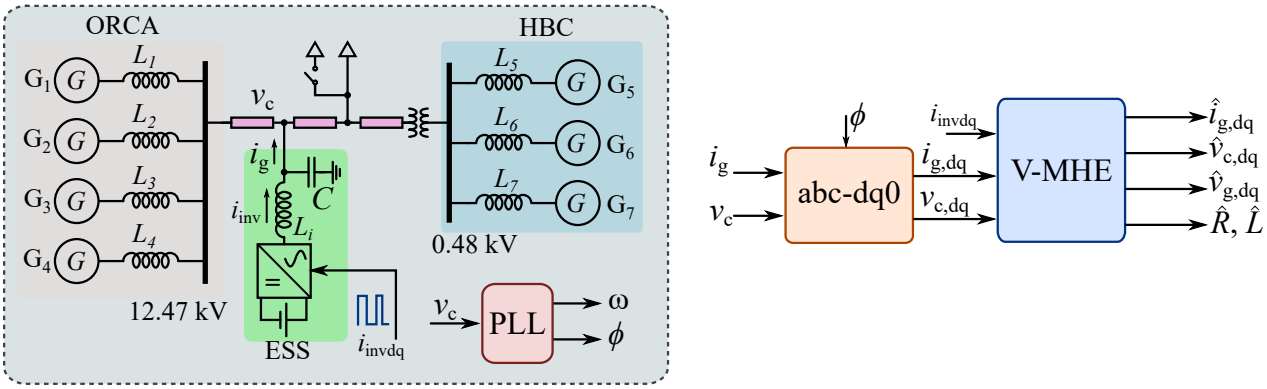

Figure 4.2. Setup of microgrid benchmark for V-MHE.

To test the proposed estimation framework, the benchmark described in Chapter 3 is used. The setup is shown in Fig. 4.2. The measured i_{g} and v_{c} (which are in abc frame) is transformed into dq frame. The phase calculated by PLL is used for the transformation. The perturbation is provided via ESS which varies the d and q components of inverter current. The measured $i_{g,dq}$ and $v_{c,dq}$ along with the perturbation signal are passed to V-MHE that provides the estimates of $i_{g,dq}$, $v_{c,dq}$, $v_{g,dq}$, R and L. The noise added in the measurement has standard deviations of 0.02 pu which makes the measurement noise covariance $\mathrm{diag}(4, 4, 4, 4) \times 10^{-4}$. The horizon length of V-MHE is set to 16 (which is two times the number of variables to be estimated as recommended in [41]). The sample time should be chosen 10-20 times smaller than the system time constant. In Chapter 3, the typical time constant for voltage dynamics was calculated as 1.06 ms. Thus, a sample time of 0.1 ms was chosen which is approximately 10 times smaller than the typical sample time.

4.5.2 Results and Analysis

This section will first analyze the identifiability of the system to check whether it is possible to estimate the parameters of interest. This also gives information about the minimum requirements

for the perturbation signal. Then, the weight selection of MHE cost function is discussed. Finally, the performance of MHE in terms of accuracy of state estimation is performed.

4.5.2.1 Identifiability Analysis

Identifiability analysis was performed using a mathematical model of voltage dynamics developed in Chapter 3 and output equation (4.26). First, the observability matrix was calculated which whose rank was found to be 8 which is the same as $n_x + n_p = 4 + 4 = 8$. This shows that it is possible to estimate all 4 states and 2 parameters. After that, the maximum derivative order of the input signal (i_{invd} and i_{invq}) is checked which was found to be 6. Then, the 6^{th} derivative of the input signal was set to zero and rank was rechecked. This is followed by setting 6^{th} and 5^{th} derivative of the input signal to zero and the rank was rechecked. This is repeated till all the order of derivatives of the input signal is set to zero. In all the cases, the rank of the observability matrix was found to be 8. A signal with all orders of derivative zero means it is a constant signal. With a constant signal, the system goes to a steady state. The value of state variables at steady state can be found by setting $f(x, u, p) = 0$ and solving for x. With the value of steady state x, we can recalculate the rank of the observability matrix for steady-state conditions under constant excitation. Now, the rank was found to be reduced to 6. This shows that the system should not go to a steady state although excitation can be constant (temporarily to avoid a steady state condition). Square wave is a good candidate to fulfill this criterion. The observability matrix can be further inspected for the column that does not contribute to rank by removing one column at a time and rechecking the rank. It was found that 5^{th} and 6^{th} columns do not contribute to the rank. This column corresponds to R and L. This shows that the estimation of R and L requires an excitation signal and when R and L are known, the estimation of v_{gd} and v_{gq} does not require an excitation signal.

4.5.2.2 Weight Selection

To identify noise covariances, the microgrid is perturbed with a square wave of frequency 100 Hz for both d and q components and amplitude 0.05 pu and 0.15 pu for d and q components respectively of inverter current. The initial guess of Q_w and R_v are chosen to be $\text{diag}(5, 3, 2, 2) \times 10^{-3}$ and

$\text{diag}(2, 2, 5, 5) \times 10^{-3}$. It should be noted that this initial guess can be chosen arbitrarily. The only requirement is that it should make the observer stable.

With the above settings, the simulation was run for 0.5 seconds (after the system attained a steady state). The simulation was run 200 times with different random seed values for the noise generator. First, the autocovariance matrix for different values of lag was calculated using (4.17). For most of the cases, it was found that the value of autocovariance is very small after the lag of 5. Thus value of maximum lag was chosen to be $N = 5$. With this value of N, covariances are estimated for all 200 simulation datasets. The mean of estimated covariances (a diagonal term only) is found to be $\widehat{Q}_w = \text{diag}(3.18, 5.11, 10.9, 2.64) \times 10^{-5}$ and $\widehat{R}_v = \text{diag}(2.3, 5.7, 3.1, 4.49) \times 10^{-4}$. Then, $W = \widehat{Q}_w^{-1/2}$ and $V = \widehat{R}_v^{-1/2}$ are chosen as weights for MHE cost function. It should be noted that the value of estimated measurement noise ($\widehat{R}_v$) is close to the injected noise covariances $\text{diag}(4, 4, 4, 4) \times 10^{-4}$ which is obtained as the square of the standard deviation of measurement noise injected.

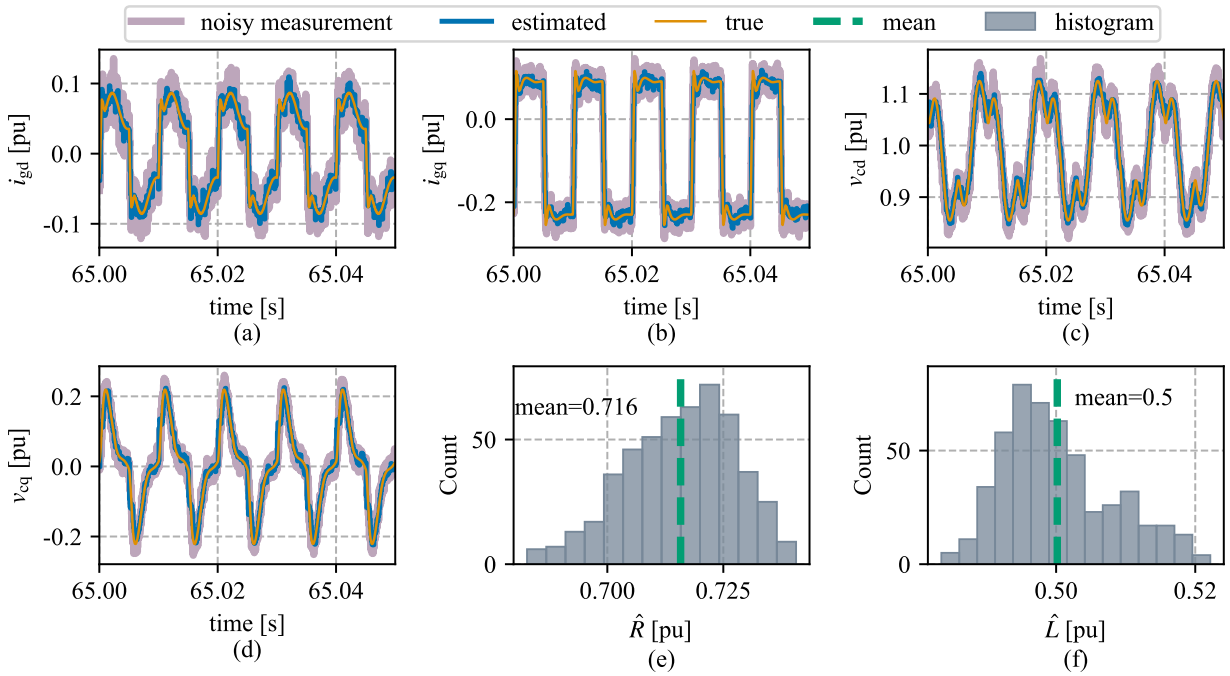

Figure 4.3. Estimation of state variables and estimated parameters. The time domain plot of state variables is shown whereas a histogram of estimated parameters is shown.

4.5.2.3 States and Parameter Estimation

To assess the performance of MHE, the value of the load is set to 0.5 pu. Since parameter estimation is also performed, a perturbation signal is required. The microgrid is perturbed with a square wave of frequency 100 Hz for both d and q components and amplitude 0.05 pu and 0.15 pu for d and q components respectively of inverter current. The larger q component was required to create a large variation in the q component of state variables.

The results of the estimation are shown in Fig. 4.3. Estimation of i_{gd} and i_{gq} is shown in Fig. 4.3(a) and Fig. 4.3(b) respectively. It can be observed that the noise in these variables is largely reduced. The NRMSE of estimated value with respect to true are 15.76%, 12.89%, 13.25% and 18.84% for i_{gd}, i_{gq}, v_{cd} and v_{cq} respectively. The mean value of estimated parameters are 0.716 pu and 0.500 pu for R and L respectively. RMSE of estimated parameters against mean value is 1.63% and 1.58% respectively.

4.6 State/Parameter Estimation for Frequency Dynamics

For state and parameter estimation of frequency dynamics of microgrids, the model developed in Chapter 3 for frequency dynamics is used. The Runge-Kutta method of order 4 is used to discretize the state equation (3.17). The state variables are $x = \begin{bmatrix} \Delta\omega & \Delta p_m^* \end{bmatrix}^\top$ and input variables are $u = \begin{bmatrix} i_{invd} \end{bmatrix}^\top$. The unknown parameters to be estimated is $p = \begin{bmatrix} M & D & \Delta p_L^* \end{bmatrix}^\top$. Further, only $\Delta\omega$ is measurable. Thus,

$$h(x, p) = \begin{bmatrix} 1 & 0 \end{bmatrix} x = \Delta\omega. \tag{4.27}$$

4.6.1 Simulation Setup

To test the proposed estimation framework, the benchmark described in Chapter 3 is used. The setup is shown in Fig. 4.4. The frequency is measured by using PLL (from which frequency deviation is calculated as $\Delta\omega = 1 - \omega$). A Gaussian noise with a variance of 10^{-7} is added to emulate real-world scenarios. The horizon length of F-MHE is set to 10 (which is two times the number of variables to be estimated as recommended in [41]). The sample time should be chosen

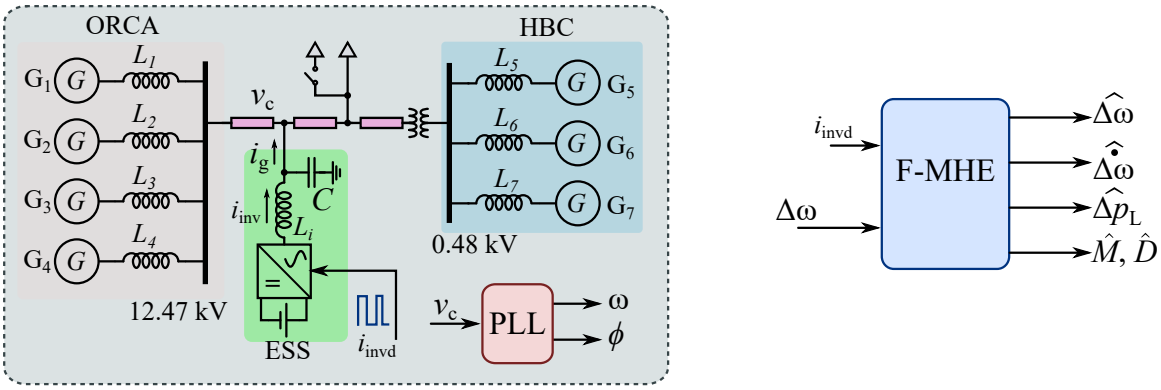

Figure 4.4. Setup of microgrid benchmark for F-MHE.

10-20 times smaller than the system time constant. In Chapter 3, the typical time constant for frequency dynamics was calculated as 0.377 s. Thus, a sample time of 20 ms was chosen which is approximately 18 times smaller than the typical sample time.

4.6.2 Results and Analysis

4.6.2.1 Identifiability Analysis

Identifiability analysis was performed using a mathematical model of frequency dynamics developed in Chapter 3 and output equation (4.27). The rank of the observability matrix was found to be 5 which is the same as $n_x + n_p = 2 + 3 = 5$. Then, the maximum order of derivative of the input signal (i_{invd}) was checked and found to be 3. Starting from higher order, the derivative of the signal was set to zero (similar as done for the case of voltage dynamics). It was found that the rank of the observability matrix remains at 5 even for constant excitation. However, when a steady state condition was imposed, the rank was reduced to 3. This shows that it is not possible to estimate all states and parameters when the system is in a steady state. Thus, constant excitation can be only temporary. The square wave is a good candidate that fulfills this criterion. However, $\Delta\omega$, Δp_m, and w_d can be estimated at all conditions of the excitation signal.

4.6.2.2 Weight Selection

To identify noise covariances, the microgrid is perturbed with a square wave of frequency 1 Hz amplitude of 0.05 pu for d component of inverter current. The initial guess of Q_w and R_v are

chosen to be diag$(10^{-7}, 10^{-7})$ and 10^{-7}. It should be noted that this initial guess can be chosen arbitrarily. The only requirement is that it should make the observer stable.

With the above settings, the simulation was run for 100 seconds (after the system attained a steady state). The simulation was run 200 times with different random values of seed for the noise generator. First, the autocovariance matrix for different values of lag was calculated using (4.17). For most of the cases, it was found that the value of autocovariance is very small after the lag of 8. Thus value of maximum lag was chosen to be $N = 8$. With this value of N, covariances are estimated for all 200 simulation datasets. The mean of estimated covariances (a diagonal term only) is found to be $\widehat{Q}_w = \text{diag}(0.018, 0.061) \times 10^{-7}$ and $\widehat{R}_v = 0.87 \times 10^{-7}$. Then, $W = \widehat{Q}_w^{-1/2}$ and $V = \widehat{R}_v^{-1/2}$ are chosen as weights for MHE cost function. It should be noted that the value of estimated measurement noise ($\widehat{R}_v$) is close to the injected noise covariances 1×10^{-7}.

4.6.2.3 States and Parameter Estimation

To assess the performance of MHE for frequency dynamics, the value of the load is set to 0.5 pu. A square wave of 1 Hz and amplitude of 0.05 pu for d component of inverter current is used as a perturbation signal. The q component of inverter current is set to zero since the q component corresponds to reactive power and reactive power has a non-significant effect on frequency dynamics. The results of the estimation is shown in Fig. 4.5.

Fig. 4.5(a) shows the perturbation signal. Fig. 4.5(b) shows the comparison of estimated value against noisy measurement. It can be observed that the estimated frequency is very close to the true value. Further, the effect of noise can be observed to be reduced. The NRMSE of $\Delta\omega$ was found to be 17.7%. Similarly, $\Delta\dot{\omega}$ was estimated from estimated value of $\Delta\omega$, Δp_m, Δp_e and Δp_L using (3.17)(a). The reason for comparing $\Delta\dot{\omega}$ is that frequency support (to be discussed in Chapter 6) required both $\Delta\omega$ and $\Delta\dot{\omega}$ to be reduced. The estimated value is then compared with the calculated value of $\Delta\dot{\omega}$ as shown in Fig. 4.5(c). The value was calculated using a derivative of $\Delta\omega$. The NRMSE was found to be 44.98%. The larger NRMSE is because the derivative was used and the derivative amplifies the noise/distortion even if it is very small. Fig. 4.5(d) shows the estimation of

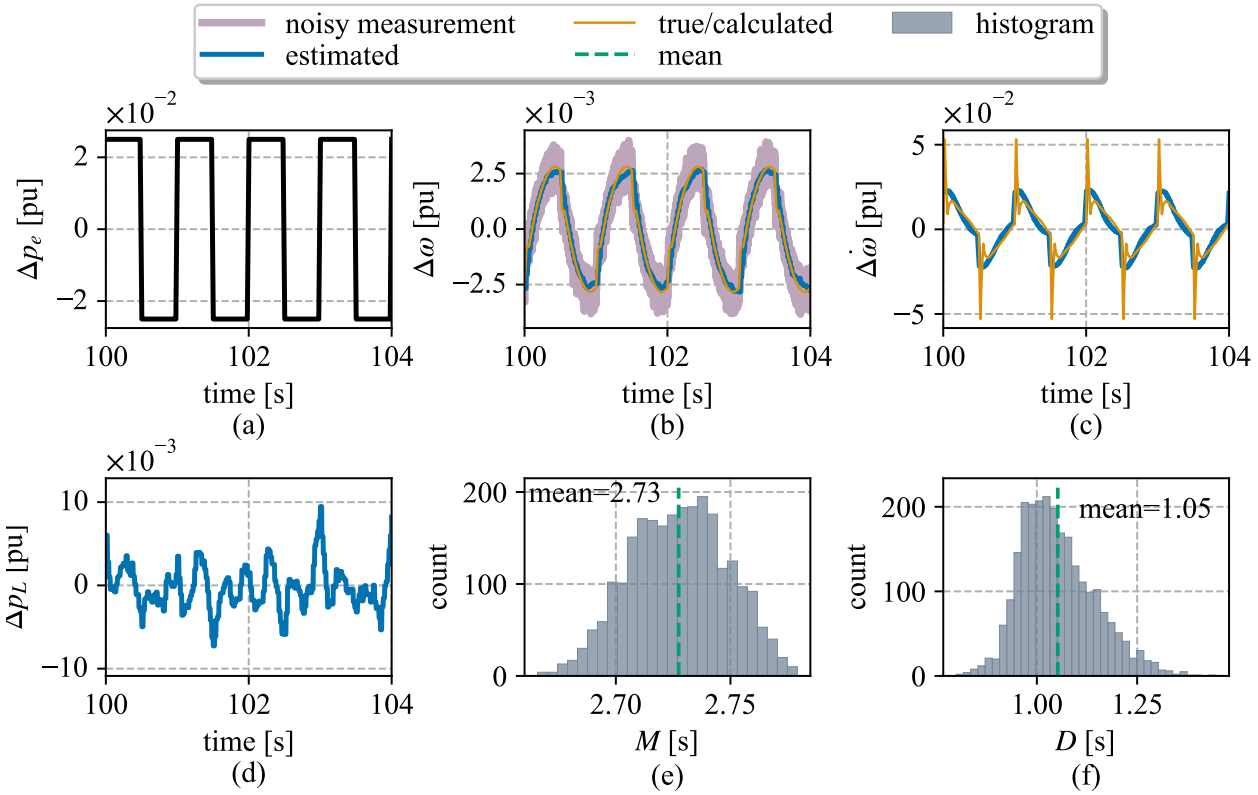

Figure 4.5. Estimation of state variables and estimated parameters. The time domain plot of state variables is shown whereas a histogram of estimated parameters is shown.

Δp_L which is nearly zero since the parameter estimation was performed after the system reached a steady state. The scenario where estimation is performed with load change will be discussed in Chapter 6. Fig. 4.5(e) and (f) show the histogram of M and D estimates. The mean of M and D were found to be 2.72 s and 1.27. Their corresponding Root Mean Square Error (RMSE) with respect to the mean was found to be 0.76% and 8.8% respectively.

4.6.2.4 Effects of Noise

The above simulation was run by increasing the noise covariance by 10 times (from 10^{-7} to 10^{-6}). With this, the value of V was reduced by $\sqrt{10}$. The NRMSE of $\Delta\omega$ and $\Delta\dot{\omega}$ are found to be 20.4% and 44.54% respectively which are slightly larger than the case where noise covariance was 10^{-7}. The RMSE against mean value was found to be 0.66% and 22.85% for M and D respectively.

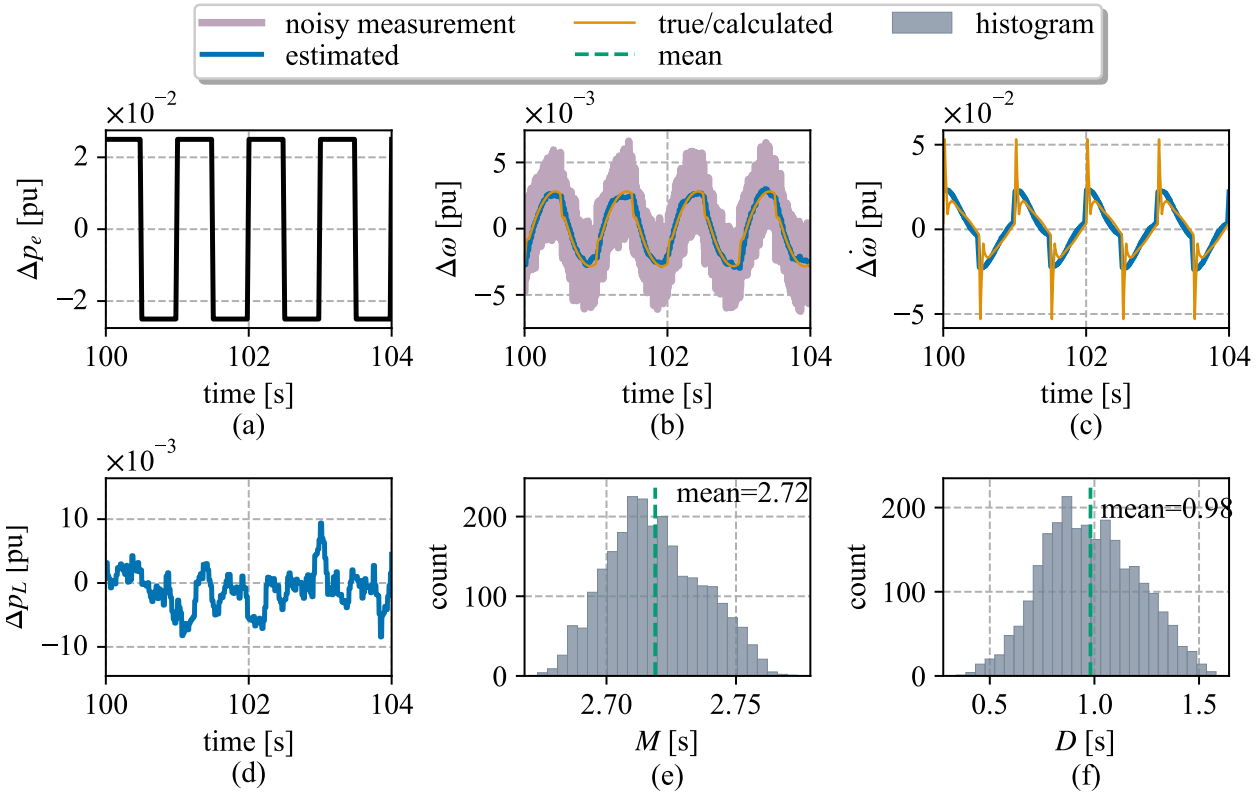

Figure 4.6. Estimation of state variables and estimated parameters when noise covariance is increased by 10 times.

Other than the estimation of D, there is no significant change in error even if noise covariance was increased by 10 times. This shows the robustness of the proposed approach against noise.

4.7 Computational Tractability

The C-code for the V-MHE and F-MHE are run on i7 11^{th} generation with 16 GB of RAM on Windows 11. The C-code was compiled with `GCC` compiler with level three optimization enabled. The average computation time to solve the V-MHE for one timestep was found to be 0.0193 ms. Similarly, the computation time of F-MHE was found to be 0.0152 ms. Both of these times are very small compared to their corresponding sample time.

4.8 Chapter Conclusions

In this chapter, parameter identifiability analysis for microgrid parameter estimation was performed which was used to check whether the parameters of interest can be estimated. It also gave the necessary criteria for perturbation signals. Then, an online method to estimate state and parameters related to voltage and frequency dynamics was introduced. The proposed approach was able to provide estimates from noisy measurements. The MHE showed good performance with a smaller value of error metrics (RMSE and NRMSE). These state and parameter estimates will be utilized to provide voltage and frequency support as presented in Chapters 5 and 6.

CHAPTER 5

MODEL PREDICTIVE CONTROL BASED DYNAMIC VOLTAGE SUPPORT

The rapid integration of renewable energy sources (RES) into the power system is revolutionizing the energy landscape, offering significant advantages such as reduced greenhouse gas emissions and improved energy sustainability. However, this integration also poses voltage stability challenges, including fluctuations, harmonics, flickering, imbalanced loads, and power oscillation. Microgrids face increased vulnerability to voltage instability due to the presence of diverse generation sources, reactive power limitations, and load dynamics [42]. In microgrids, voltage instability occurs in a major event like a sudden change in power demand or output from RES or when a generator stops working. Even small changes in demand can cause voltage instability, especially in systems already operating near their limits. In conventional power systems, the R/X ratio of the transmission/distribution lines is lower, and the voltage is sensitive to reactive power only; hence, reactive power management techniques ensure a reliable power supply by reducing fluctuations. In contrast, microgrids typically operate at low to medium voltage ranges and have a high R/X ratio [5], resulting in high voltage sensitivity to both active and reactive power. Depending on the ratio, the voltage could be more sensitive to active power. Thus, the traditional voltage control approach used in conventional power systems is not applicable to microgrids. The control approach should consider both active and reactive power as control signals. This chapter is devoted to developing a MPC based approach for dynamic voltage support.

5.1 Chapter Objectives and Contributions

The main objective of this chapter is to develop a control framework based on model predictive control for dynamic voltage support. The specific contribution is:

- Design of dynamic voltage support framework that achieves required performance while incorporating physical constraints of the ESS

5.2 Proposed MHE-MPC Framework

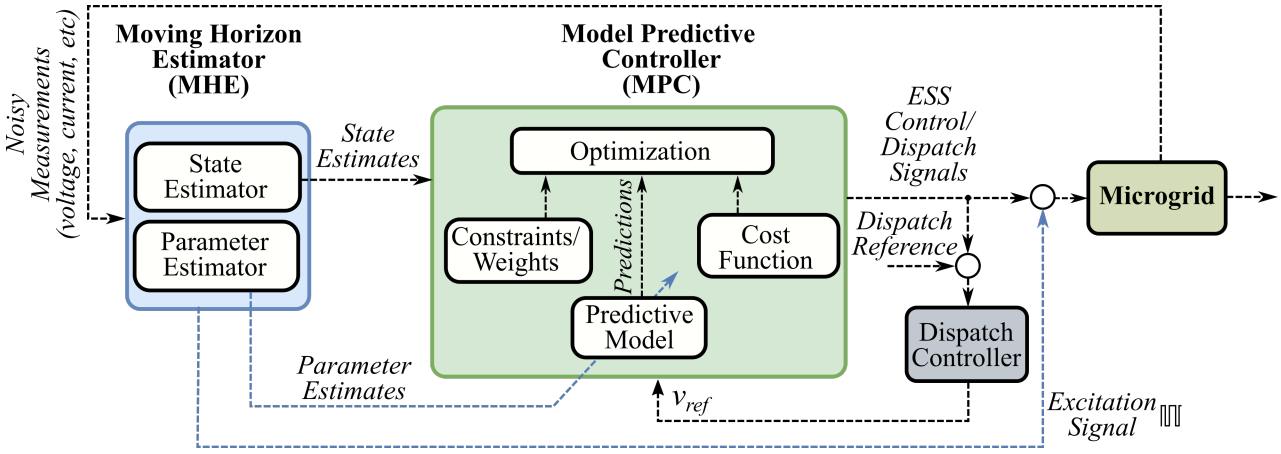

Figure 5.1. Proposed MHE-MPC framework for voltage support. The MHE provides estimates of states and MPC provides ESS control signals.

The proposed MHE-MPC framework is shown in Fig. 5.1. The proposed approach contains integrated MHE and MPC. The MHE performs states and parameter estimation from the noisy measurement. MHE can also estimate the effect of unknown disturbance of the system e.g., the effect of change in load. These estimates are used in MPC to generate a control signal for ESS. The MHE and MPC are formulated as an optimization problem that uses a simplified model of the system voltage dynamics, informational/operational constraints, and cost function. The solution to the MHE optimization problem at each time step gives state and parameter estimates and the solution to the MPC optimization problem gives control signals to be applied to the system. Further, an external dispatch controller is also included so that the proposed scheme provides voltage support at transient only and supplies normal dispatch power in a steady state.

5.3 Model Predictive Control

MPC is an online optimization-based control approach where a mathematical model is used to predict the future trajectory and compute the control signal such that the trajectory of the system is close to the desired trajectory. The period up to which prediction is made is called prediction horizon. The cost function is defined as how close the trajectory is to the desired trajectory. The

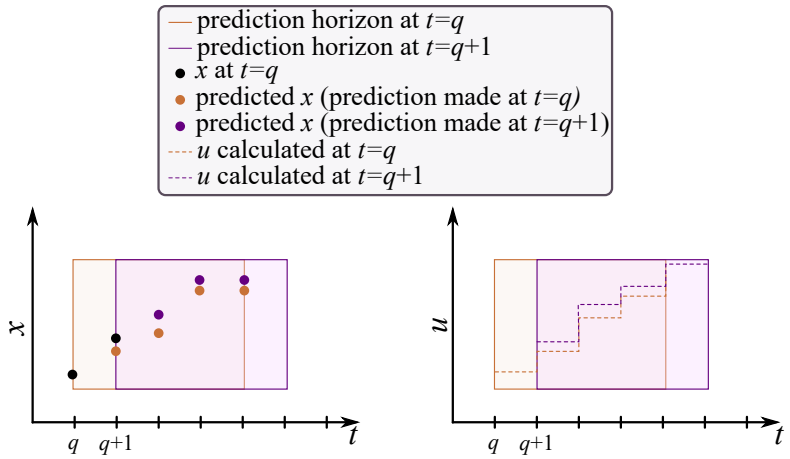

Figure 5.2. Illustration of MPC concept.

control problem takes the form of an optimization problem which is solved at every time step. The concept is illustrated in the Fig. 5.2. At any given instant (e.g $t = q$), the actual value of state (x) which the state estimator generally provides is passed to MPC problem to solve for control input. MPC calculates the value of control input for the entire horizon from which the first one is applied at $t = q$. At the next timestep ($t = q + 1$), a new value of x is obtained which is passed to MPC to calculate the control signal again. It should be noted that actual x at $t = q + 1$ might be slightly different than the one predicted in the previous timestep because of some error in the prediction model. Thus, control input, although calculated for entire horizon, cannot be used for future timesteps and has to be recalculated at every timesteps.

5.3.1 Formulation of MPC

Let N represent the horizon length of MPC. This N represents the number of timesteps in the future for which a prediction is made. Let us also define $K = q + N$. Let $\Gamma = \{q, q + 1, ..., q + N\}$ represents the set of sampling instants where q represents the current timestep. Then, MPC can be

formulated as

$$\min_{x_k,u_k} J_\Gamma = \sum_{k=q}^{K} \left\| l_k(x_k,u_k) \right\|_2^2 + \psi_K(x_K) \tag{5.1a}$$

$$x_q = \hat{x}_q \tag{5.1b}$$

$$x_{k+1} = f(x_k,u_k,\hat{p}_q)\ \forall\ k \in \Gamma/\{K\} \tag{5.1c}$$

$$g_{lk} \le g(x_k,u_k) \le g_{uk}\ \forall\ k \in \Gamma/\{K\} \tag{5.1d}$$

$$g_{lK} \le g(x_K) \le g_{uK}. \tag{5.1e}$$

Here, $\left\| l_k(x_k,u_k) \right\|_2^2$ represents stage cost. The stage cost is written in terms of the square of the L2 norm because this makes the implementation using GGN easier as explained in Chapter 4. The stage cost represents the error between the desired and actual trajectory. The function $\psi_K(x_K)$ represents a terminal cost. This cost represents approximate value of the sum of stage cost from $k = K$ to $k \to \infty$. Equation 5.1b represents the state variable at the current timestep q must be equal to the externally provided value, which comes from measurement or state estimator. The equation (5.1c) represents a discrete-time state equation that is utilized to make predictions. The equation (5.1d) represents the general constraint of the system such as the physical limit of the actuator. The equation 5.1e represents terminal constraint.

For MPC that provides dynamic voltage support, the following is the formulation:

$$\min_{i_{\text{invd,k}},i_{\text{invq,k}},x_k} J_\Gamma = \sum_{k=q}^{K-1} \left[\left\| v_{\text{cdk}} - v_{\text{ref}} \right\|_Q^2 + \left\| u_k \right\|_S^2 \right] + \psi_K(x_K) \tag{5.2a}$$

subject to

$$x_q = \hat{x}_q \tag{5.2b}$$

$$x_{k+1} = f(x_k,u_k,\hat{p}_q)\ \forall\ k \in \Gamma/\{K\} \tag{5.2c}$$

$$|i_{\text{invd},k}| \le I_{\text{dmax}}\ \forall\ k \in \Gamma/\{K\} \tag{5.2d}$$

$$i_{\text{invd},k}^2 + i_{\text{invq},k}^2 \le I_{\text{max}}^2\ \forall\ k \in \Gamma/\{K\} \tag{5.2e}$$

where v_{ref} is the reference voltage, I_{max} and I_{dmax} are maximum inverter current (based on kVA rating) and maximum d-component of inverter current (based on available active power for voltage

support), $\hat{x}_q$ represents estimate of states at current discrete-time provided by MHE, and Q and S are 1×1 and 2×2 matrix respectively which are the weights for their corresponding term. The first term in eq. 5.2a represents the control error penalty and the second term represents the cost of utilizing ESS power. Matrices Q and S are weighting matrices that can be used to set different priorities. For example, a higher value of Q prioritizes good QoS over ESS utilization and vice versa.

5.3.2 Terminal Cost

The objective of the terminal cost is to approximate the cost function for $k = \{q + N, ..., \infty\}$ i.e., to find an approximate representation of the following function:

$$\min \sum_{k=K}^{\infty} \left\| v_{\text{cdk}} - v_{\text{ref}} \right\|_Q^2 + \sum_{k=K}^{\infty} \left\| u_k \right\|_S^2 \text{ subject to (5.1c)} \tag{5.3}$$

Different technique exists to approximate the above function. In this work, a process similar to MHE arrival cost will be followed to derive MPC terminal cost. Further, we will represent the terminal cost with a quadratic approximation of the following form

$$\psi_K(x_K) = \left\| x_K - \bar{x}_K \right\|_{P_K}^2. \tag{5.4}$$

From standard dynamic programming, we can write

$$\psi_K(x_K) = \min_{u_K} \left[\left\| v_{\text{cdK}} - v_{\text{ref}} \right\|_Q^2 + \left\| u_K \right\|_S^2 + \psi_{K+1}(x_{K+1}) \right] \tag{5.5}$$

subject to

$$x_{K+1} = f(x_K, u_K, p_K). \tag{5.6}$$

A linear approximation of state equation is desired for closed form solution and thus $x_{K+1} = \tilde{x} + X_x x_K + X_u u_K$. Then, the terminal cost $\psi_K(x_K)$ can be written as

$$\psi_K(x_K) = \min_{u_K} \left\| \begin{matrix} Q(v_{\text{cdK}} - v_{\text{ref}}) \\ Su_K \\ P_{K+1}(x_{K+1} - \bar{x}_{K+1}) \end{matrix} \right\|_2^2 \tag{5.7}$$

$$= \min_{u_K} \left\| s + S \begin{pmatrix} u_K \\ x_K \end{pmatrix} \right\|_2^2 \tag{5.8}$$

where $S = \left(\begin{array}{c|c} 0 & Q \begin{pmatrix} 0 & 0 & 1 & 0 \end{pmatrix} \\ S & 0 \\ P_{K+1}X_u & P_{K+1}X_x \end{array} \right)$ and $s = \begin{pmatrix} -Qv_{\text{ref}} \\ 0 \\ P_{K+1}(\tilde{x} - \bar{x}_{K+1}) \end{pmatrix}$. With $Q\mathcal{R} = S$ being QR decomposition of S, we can write

$$\psi_K(x_K) = \min_{u_K} \left\| Q^\top s + Q^\top Q \mathcal{R} \begin{pmatrix} u_K \\ x_K \end{pmatrix} \right\|_2^2 \tag{5.9}$$

$$= \min_{u_K} \left\| \begin{pmatrix} \rho_1 \\ \rho_2 \\ \rho_3 \end{pmatrix} + \begin{pmatrix} \mathcal{R}_1 & \mathcal{R}_{12} \\ 0 & \mathcal{R}_2 \\ 0 & 0 \end{pmatrix} \begin{pmatrix} u_K \\ x_K \end{pmatrix} \right\|_2^2 \tag{5.10}$$

$$= \left\| \rho_2 + \mathcal{R}_2 x_K \right\|_2^2 \tag{5.11}$$

$$\tag{5.12}$$

where $\begin{pmatrix} \rho_1 \\ \rho_2 \\ \rho_3 \end{pmatrix} = Q^\top s$. Note that constant term is neglected. Then,

$$P_K = \mathcal{R}_2 \text{ and } \bar{x}_K = -\mathcal{R}_2^{-1} \rho_2 \tag{5.13}$$

This calculates P_K and $\bar{x}_K$ from the value of P_{K+1} and $\bar{x}_{K+1}$. This process should be done recursively till P_K and $\bar{x}_K$ converge.

5.3.3 External Controller

An external dispatch controller is required since we need ESS to support voltage at transients only. In a steady state, the active power should be the same as the dispatch reference (i_{dref}). To do this, an external integral controller is added. This controller varies the value of v_{ref} until i_{invd} is the same as i_{dref}. Time scale for this controller must be very slow as compared to the dynamics of the system and MPC. The structure of this controller is shown in Fig. 5.3. where K_e is the gain of the

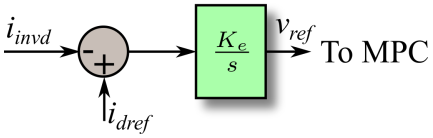

Figure 5.3. Structure of external controller.

controller that determines the time-scale of the controller. The approximate time constants can be derived with the following assumptions:

1. external controller operates at a very slower time scale compared to dynamics of the system and MPC

2. steady-state value of v_{gd} and v_{gq} are constant

The first assumption allows us to discard the q-component to derive time constants and the second assumption allows us to represent the transfer function of the system and MPC with constant gain. Further, with the second assumption, $v_{ref} \approx v_{cd}$ also holds true. With these assumptions, we can derive the time constant of the external controller which can be used to select the proper value of gain K_e. First, we set the left-hand side of (3.8) zero (steady state of the system) and solve for $i_{invd}, i_{invq}, i_{gd}, i_{gq}$. The expression for i_{invd} we get is given by

$$i_{\text{invd}} = \frac{-CL^2\omega^3 v_{\text{cq}} - CR^2\omega v_{\text{cq}} + L\omega v_{\text{cq}} - L\omega v_{gq} + Rv_{\text{cd}} - Rv_{\text{gd}}}{R^2 + \omega^2 L^2} \tag{5.14}$$

For steady state, $v_{\text{cq}} = 0$. Thus, we can write

$$i_{\text{invd}} = \frac{-\omega L v_{\text{gq}} + Rv_{\text{cd}} - Rv_{\text{gd}}}{R^2 + \omega^2 L^2} \tag{5.15}$$

Further, we can neglect $\omega L v_{gq}$ as compared to $R v_{gd}$ since $R > \omega L$ and $v_{gd} >> v_{gq}$. This gives,

$$i_{invd} = \frac{R v_{cd} - R v_{gd}}{R^2 + \omega^2 L^2} \tag{5.16}$$

Thus, we can write gain $\frac{\Delta i_{invd}}{\Delta v_{cd}} = \frac{\Delta i_{invd}}{\Delta v_{ref}} = \frac{R}{R^2+\omega^2 L^2}$. Then, the closed-loop transfer function with the external controller can be derived as

$$G(s) = \frac{K_e R}{K_e R + \omega^2 L^2 s + R^2 s} \tag{5.17}$$

From above equations, the time constant can be written as

$$\tau = \frac{R^2 + \omega^2 L^2}{K_e R}. \tag{5.18}$$

Thus, the value of K_e determines the time for which dynamic voltage support is to be provided. Larger K_e gives a smaller time constant which means dynamic voltage support is provided for a smaller amount of time during transient and vice-versa.

5.4 Simulation Setup

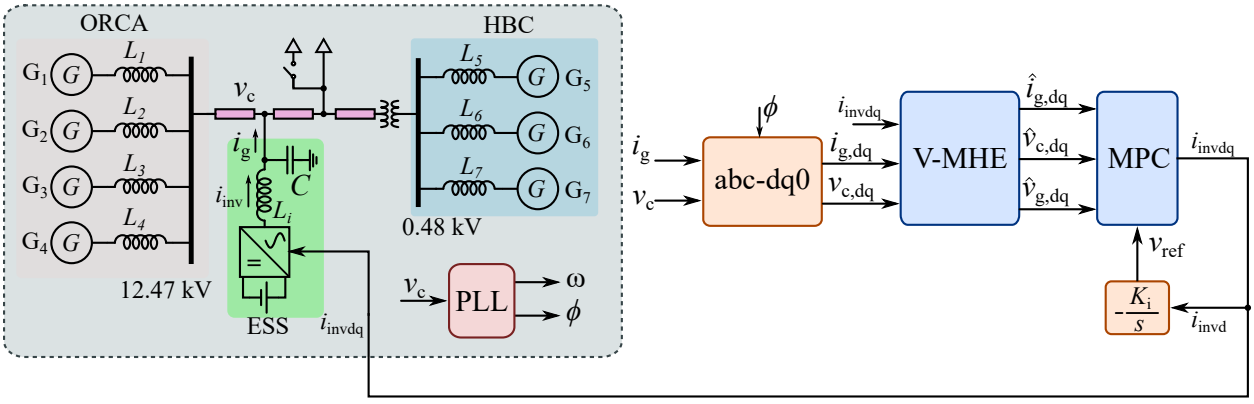

Figure 5.4. Simulation setup of MHE-MPC based dynamic voltage support.

To assess the performance of the proposed approach, the benchmark described in Chapter 3 is used. The voltage at PCC is used as a reference to transform the voltage and current in abc frame to dq frame. The noise of same amount used in Chapter 4 was used to emulate real-world scenarios. The state estimates provided by V-MHE (discussed in Chapter 4) is passed to MPC which computes

the d and q component of inverter current. The sample time of MPC was set to 0.1 ms which is about 10 times smaller than the typical sample time computed in Chapter 3. The horizon length of MPC was set to 12 timesteps. The initial load of 0.3 pu is connected along with the step load of 0.15 pu. The step load is used to create voltage deviation in the system to test the performance of the proposed approach. The weights of MPC are tuned based on desired performances. The effect of the weight of MPC has been analyzed in the following sections.

5.5 Results and Analysis

In this section, the performance of the proposed approach is discussed. First, the performance with different weights of MPC is discussed. After that, the effect of different components of the proposed approach is discussed.

5.5.0.1 Performance of Voltage Support

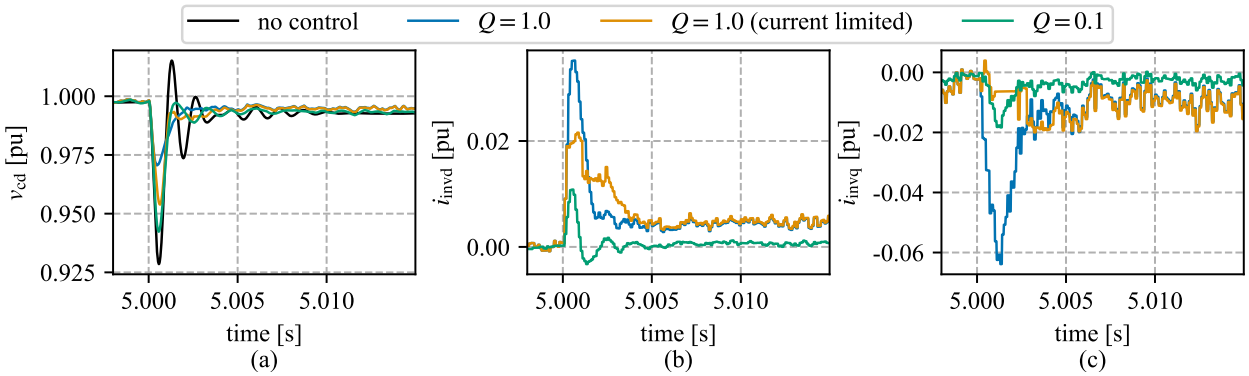

Figure 5.5. Plot showing the performance of MPC under difference scenarios. Scenarios with different values of weight and limits on ESS currents are considered.

The performance of MPC under different scenarios is shown in Fig. 5.5. Three cases with MPC is considered. In all scenarios, value of s_{11} and s_{22} are set to 0.5 and 0.05. In the first scenario, value of Q is set to 1.0 with no limit in currents i.e., constraints from (5.2d) and (5.2e) are deactivated. This makes MPC utilize large amount of inverter current; however, at the same time, it provides better voltage support. In the second scenario, constraints from (5.2d) and (5.2e) are activated with value of I_{dmax} and I_{max} set to 0.02 pu. The results show that voltage support

is compromised (voltage deviation has increased) since the inverter current is limited. In the real world, this scenario may represent the situation when limited inverter power is available for voltage support. The third scenario is derived from first scenario by setting the value of Q to 0.1. Reducing the value of Q means we give less priority to the voltage support and more priority to reducing inverter currents. Thus, in this scenario, inverter currents are highly reduced and as a result, voltage support is also compromised.

In all the scenarios, it can be noticed that oscillation in the voltage is reduced. Also, it can be noticed that the magnitude of i_{invq} in steady state is larger than i_{invd}. It is because we provided smaller weight for i_{invq} (s_{22}) and as a result, a larger magnitude of i_{invq} is utilized. Thus, depending on the available power and required performance of voltage support, the ESS operator can tune the weights to find the right balance between them.

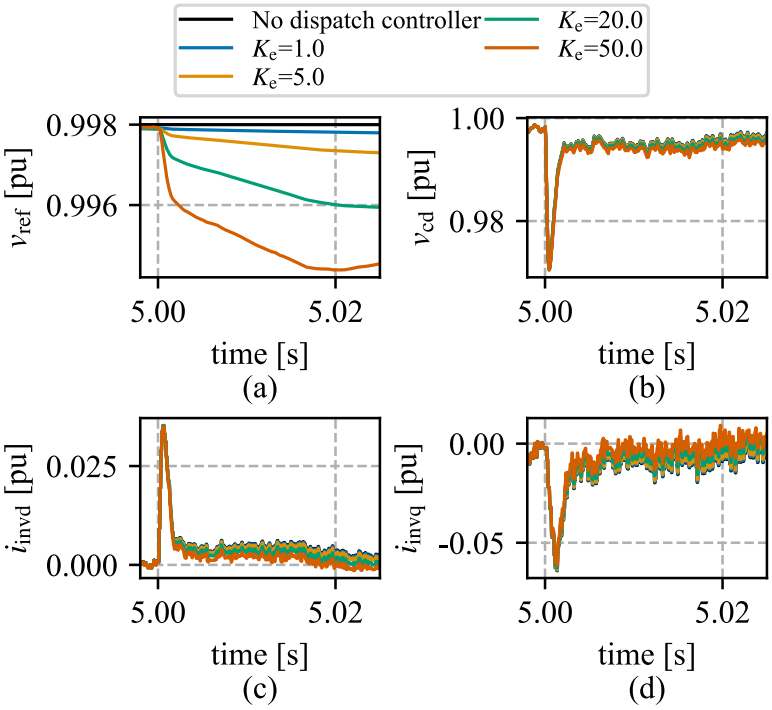

Figure 5.6. Response of voltage support for different value of external controller gain.

5.5.0.2 External Dispatch Controller

To assess the performance of the external dispatch controller, the value of K_e is set to 0, 1.0, 5.0 and 20.0. The values of Q, s_{11} and s_{22} are set to 1.0, 0.5, and 0.05 respectively. The limits on inverter current are deactivated. The initial value of v_{ref} was set to 0.998 pu (the steady state voltage before load change). The response of voltage support for different values of K_e is shown in the Fig. 5.6. When no dispatch controller is used, value of v_{ref} remains constant and as a result, some amount of inverter currents are utilized in the steady state. When dispatch controller is used v_{ref} is goes to the value of voltage when no controller is used in a steady state. The rate at which v_{ref} approaches that value of voltage is determined by value of K_e. For smaller value of K_e, v_{ref} changes very slowly and as a result, i_{invd} approaches zero slowly. On the other hand, with the larger value of K_e, the inverter currents (i_{invd} and i_{invq}) go to zero faster. The ESS operator can use different values of K_e to provide dynamic voltage support for the desired amount of time during transient. If voltage support is required even in the steady state, the value of K_e can be set to zero.

Generally, there are other voltage controllers in the microgrid that can regulate the voltage at a slower timescale. Based on timescale of this controller, the ESS operator can choose the value of k_e such that the proposed approach slowly give up the voltage control task and other slower control can take over.

5.5.1 Effects of Arrival Cost

To assess the performance of using arrival cost (of MHE), two scenarios, one with arrival cost and another without arrival cost are considered. The values of Q, s_{11} and s_{22} are set to 1.0, 0.5, and 0.05 respectively. The limits on inverter current are deactivated. The results of using arrival cost and not using arrival cost is shown in Fig. 5.7. Fig. 5.7 (a) shows the voltage when there is a load change whereas Fig. 5.7 (b) shows ESS currents. When arrival cost is not used, there are slightly more oscillations in i_{invdq} and significantly more oscillations in i_{invdd} than when arrival cost is used. This is because, with no arrival cost, the performance of MHE is compromised. This compromise results in MPC getting state estimates with more noise components. This noise results in calculated

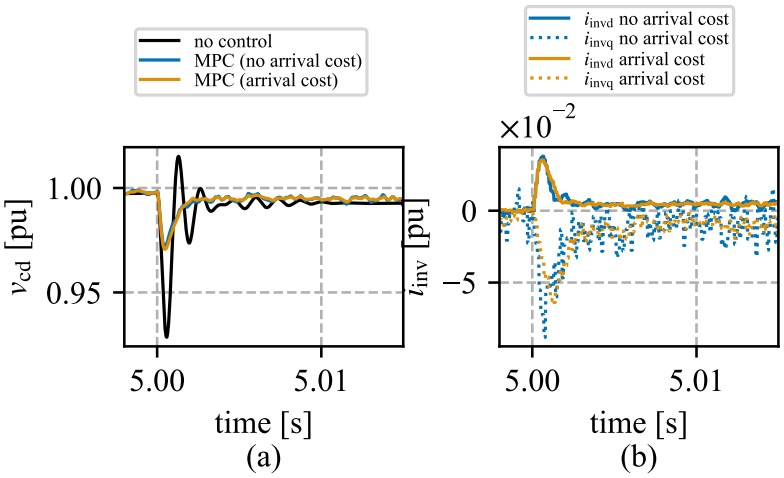

Figure 5.7. Performance of MPC when arrival cost is activated and deactivated.

ESS currents being oscillatory. With no arrival cost, MHE would required larger horizon length which is not suitable for fast voltage support because of tight constraint on computational time.

5.5.2 Effects of Terminal Cost

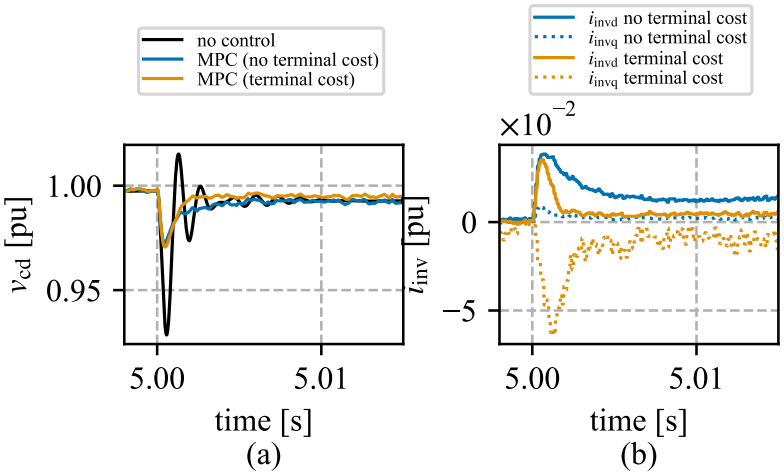

Figure 5.8. Performance of MPC when terminal cost is activated and deactivated.

Two scenarios, one with terminal cost and another without terminal cost are considered to assess the performance of using terminal cost. The values of Q, s_{11} and s_{22} are set to 1.0, 0.5, and 0.05 respectively. The limits on inverter current are deactivated. The results of using terminal cost and not using terminal cost is shown in Fig. 5.8. Fig. 5.8 (a) shows the voltage when there is a load change whereas Fig. 5.8 (b) shows ESS currents. There is no significant difference in

maximum voltage deviation although overall voltage deviation is reduced. During steady state, the voltage deviations are 0.0072 pu and 0.0050 pu for the case with no terminal cost and terminal cost respectively which might not be very significant however, there is a significant difference in the ESS currents. When there is no terminal cost, a large magnitude of d-component current and a small magnitude of q-component current are utilized. However, when the terminal cost is used, there is a reduction in the magnitude of d-component current. The d-component corresponds to active power; hence, a magnitude reduction is desirable.

5.5.3 Computational Performance

The average computation time of the proposed MPC was found to be 0.0129 ms which is significantly smaller than the sample time (0.1 ms). This shows that the proposed approach is computationally feasible.

5.5.4 Effect of Computational Delay

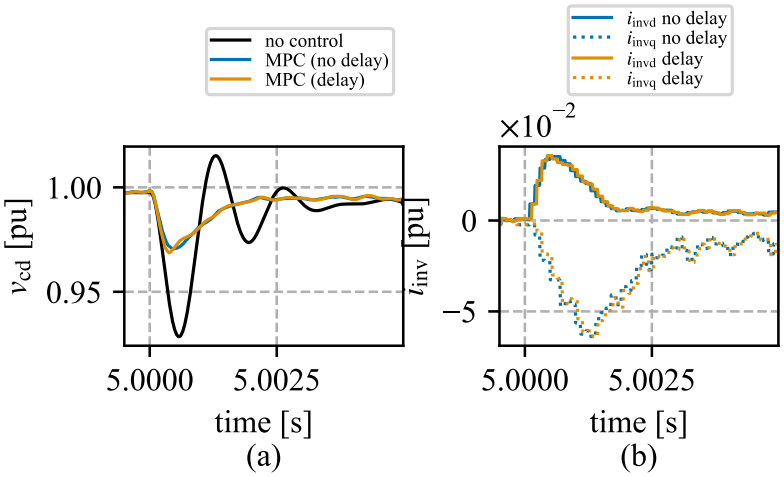

Figure 5.9. Plot showing effect of computational delay on the performance of voltage support.

To assess the effect of computational delay on the voltage support performance, the values of Q, s_{11}, and s_{22} are set to 1.0, 0.5, and 0.05 respectively. The limits on inverter current are deactivated. The output of MHE and MPC are delayed by their corresponding computation time. The performance comparison is shown in Fig. 5.9. It can be seen that the voltage deviation has

increased slightly but the difference is very small. This shows that the proposed approach is robust against delay which usually arises in the real world.

5.6 Chapter Conclusions

In this chapter, a control framework for dynamic voltage support for microgrids was developed. The framework used MHE to get state estimates which was utilized by MPC to achieve a flexible framework. Through the simulations performed in a Cordova benchmark from Alaska, it was illustrated that the MPC can achieve significant reductions in voltage deviation. Further, oscillation was also found to be improved. The different weights provided in MPC could also adjust the performance which allows the ESS operator to tune the Quality of Service (QoS) provided. Also, the effects of different components of the proposed approach (terminal cost, external dispatch controller, etc) were also discussed.

CHAPTER 6

INTEGRATED VOLTAGE-FREQUENCY SUPPORT FOR MICROGRIDS

Microgrids have been proposed as a solution to achieve reliable and resilient grids of the future [43]. In isolated/islanded microgrids, synchronous generators are often responsible for maintaining the voltage and frequency of the system. The distributed energy resources (DERs), such as solar and energy storage systems (ESSs), typically act as passive elements or might have a secondary supporting role regarding voltage and frequency control. The large-scale integration of renewable DERs brings various challenges regarding dynamic voltage and frequency control. Microgrids have intrinsic differences compared to traditional interconnected power systems in terms of size, feeder type, high cross-coupling between voltage and frequency dynamics, a high share of converter-based renewable sources, and low inertia [3, 5]. Furthermore, microgrids operating in isolated/islanded mode are starting to become more common in distribution networks. In an isolated/islanded mode of operation, the primary controller is responsible for maintaining the voltage and frequency of the system. The loss of a single generator, inverter, or load, without proper coordination, can cause significant power imbalance and lead to large voltage and frequency deviations that compromise power quality and reliability. Thus, improved control techniques for DERs are required to maintain proper operation.

Traditionally, the voltage and frequency controllers are designed independently under the assumption that the voltage and frequency dynamics of the system are decoupled [4]. However, microgrids are typically operated at low to medium voltage ranges, hence the R/X ratio is typically very high [5]. Furthermore, changes in the system voltage will also be reflected as changes in the system load owing to the relatively small size of the microgrid. All these factors contribute to a stronger coupling between voltage and frequency dynamics in microgrids as compared to traditional grids. For combined voltage and frequency control, droop-based controllers have been traditionally used [23]. In this approach, the d and q components of the current are used to support the frequency and voltage, respectively, as a proxy for active and reactive power support. In general, droop-based

approaches assume that voltage and frequency dynamics are decoupled. Another proposed method is to utilize the voltage dependency of active power to control frequency [2]. In this method, voltage is modulated to regulate the frequency, but this does not work when the majority of load power is insensitive to voltage deviations. Furthermore, a voltage-based frequency controller often conflicts or interferes with a voltage controller, making it difficult to achieve both control goals simultaneously. Model predictive control (MPC)-based approaches have been previously proposed in [44, 21, 45] under the assumption that the voltage and frequency dynamics are decoupled. Because of the ability of MPC to handle operational constraints and operational flexibility, this project proposes using MPC for integrated voltage and frequency support.

6.1 Chapter Objectives and Contributions

The main objective of this chapter is to develop a control framework based on droop and model predictive control for integrated voltage and frequency support. The specific contribution is:

- Design of integrated voltage and support framework that achieves required performance while incorporating physical constraints of the ESS

6.2 Preliminary Study on Integrated Voltage-Frequency Support

In previous work, MPC based approach was employed to provide integrated voltage and frequency support, as tested on a simplified system [25]. This study utilized an extensive MPC horizon length, approximately 1250 timesteps, due to the sample time being determined by the time constant of voltage dynamics. It was essential for the MPC horizon to encompass a substantial portion of the frequency dynamics, which have a larger time constant, thereby necessitating a significant number of timesteps. The performance of the MPC, as depicted in Fig. 6.1, demonstrated its capability to provide concurrent frequency and voltage support. The findings of this study confirmed the theoretical possibility of achieving simultaneous voltage and frequency support. However, the computational load associated with this approach is substantial, rendering

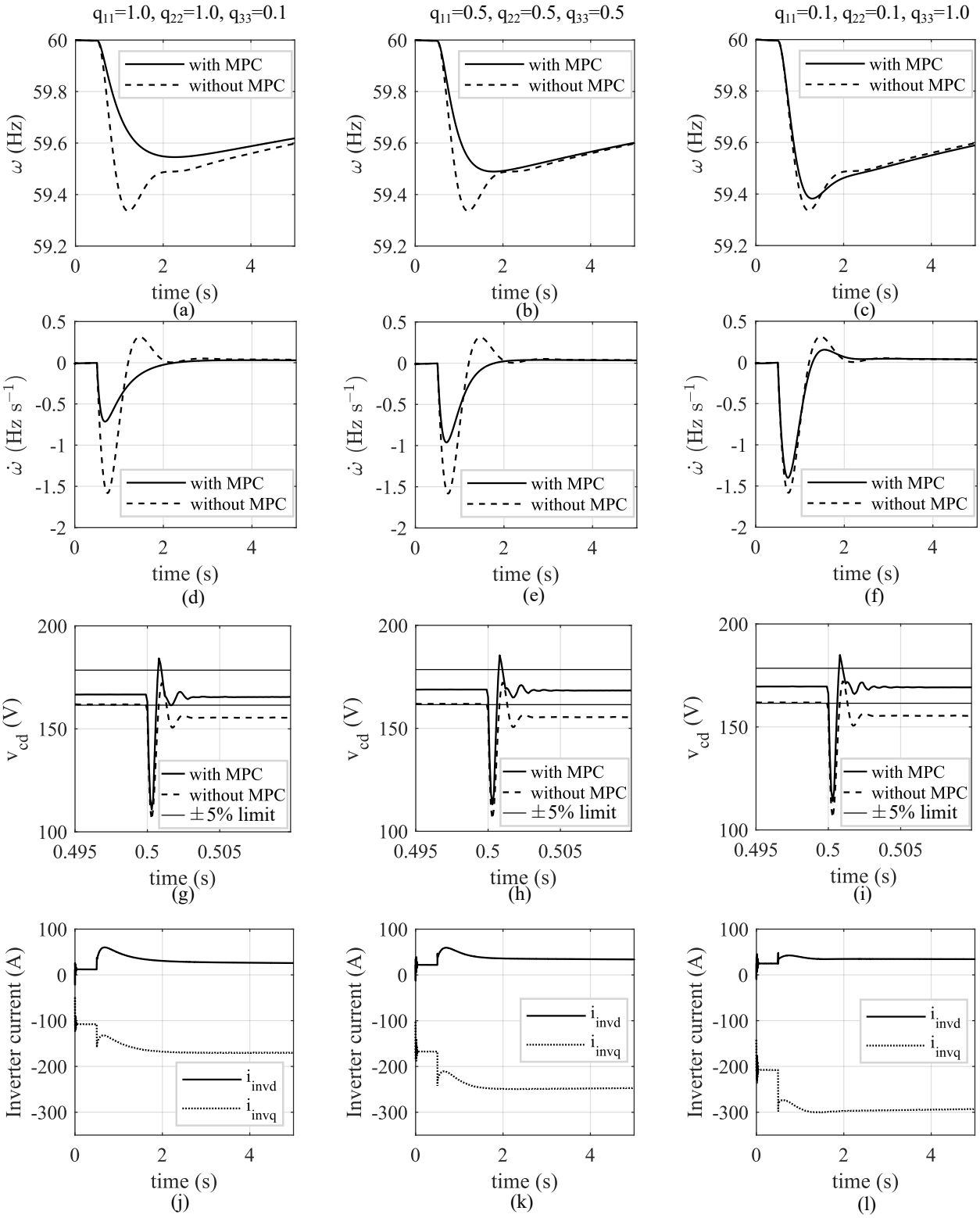

Figure 6.1. Comparison of voltage and frequency support for different weighting parameters.

real-time operation infeasible. Consequently, this necessitates the exploration of unconventional methodologies.

6.3 Proposed Framework

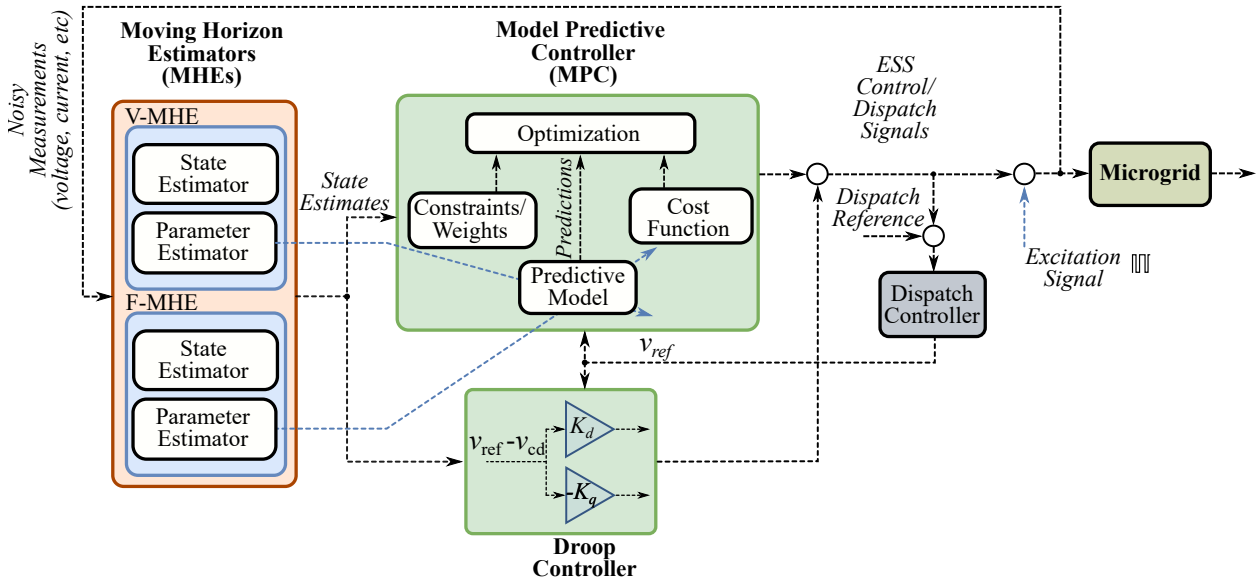

Figure 6.2. Proposed MHE-Droop-MPC framework for voltage support. The MHE provides estimates of states and MPC provides ESS control signals.

The proposed framework for MHE-Droop-MPC for integrated voltage and frequency support is shown in Fig. 6.2. The proposed approach contains two MHEs: one for voltage dynamics estimation (named V-MHE) and the other for frequency dynamics estimation (named F-MHE). They are described in detail in Chapter 4. The MHEs estimate states (and parameters occasionally). The droop is utilized to provide voltage support (especially dynamic) and MPC is utilized to provide frequency support and steady-state voltage support.

6.4 Droop Control

The droop is one of the simplest control approaches. As described in Chapter 2, the droop is a proportional control where some saturation and deadband might also be incorporated. In this

work, droop is formulated as follows

$$i_{\text{inv,dq}}^{\text{droop}} = (v_{ref} - v_{cd}) \begin{bmatrix} K_d \\ -K_q \end{bmatrix} \tag{6.1}$$

where v_{ref} is the reference voltage, and K_d and K_q are the droop coefficients for the d and q components of inverter current, respectively. Larger values of droop coefficients provide better voltage support; however, the system can become oscillatory and even unstable. Thus, it is necessary to select the proper value of droop coefficients. Since droop has just a proportional gain, it can be designed similarly to a proportional controller.

6.5 Model Predictive Control

MPC is an online optimization-based control approach where a mathematical model is used to predict the future trajectory and compute the control signal such that the trajectory of the system is close to the desired trajectory. The basic concept of MPC and its generic formulation is described in the Chapter 5. Here, MPC for integrated voltage-frequency support is described.

6.5.1 Steady State Voltage Behavior

Since MPC provides steady-state voltage support as well, a mathematical equation representing steady-state voltage behavior is required. At a steady state, a derivative of state variables with respect to time is zero. Thus, we can set the right-hand side of (3.8) to zero and solve for v_{cd}. AFter some approximation, we get

$$v_{\text{cd}} = v_{\text{gd}} + Ri_{\text{invd}} - \omega Li_{\text{invq}}. \tag{6.2}$$

This equation will be used as a constraint within the MPC formulation.

6.5.2 Formulation of MPC

Let N be the horizon length of MPC, and $\Gamma = \{q, ..., q+N-1\}$ be the discrete time steps throughout the forward prediction horizon. Then, the MPC formulation takes the following form:

$$\min_{u_k \forall k \in \Gamma} \sum_{k=q}^{q+N-1} \left[\left\| \begin{matrix} v_{\text{cd},k} - v_{\text{ref}} \\ \Delta\omega_k \\ \Delta\dot{\omega}_k \end{matrix} \right\|_Q^2 + \left\| u_k \right\|_S^2 \right] + \psi_K(x_K) \tag{6.3a}$$

subject to

$$x_{k+1} = f(x_k, u_k, w_d) \; \forall \; k \in \Gamma \tag{6.3b}$$

$$\Delta\dot{\omega}_k = -\frac{D}{M}\Delta\omega_k + \frac{1}{M}\Delta p^*_{m,k} + \frac{1}{M} i_{invd,k} - \frac{1}{M}\hat{\Delta p}^*_{L,q} \tag{6.3c}$$

$$v_{\text{cd},k} = \hat{v}_{\text{gd,q}} + R i_{\text{invd},k} - \omega L i_{\text{invq},k} \; \forall \; k \in \Gamma \tag{6.3d}$$

$$|i_{\text{invd},k}| \leq I_{\text{d},max} \; \forall \; k \in \Gamma \tag{6.3e}$$

$$i^2_{\text{invd},k} + i^2_{\text{invq},k} \leq I^2_{max} \; \forall \; k \in \Gamma \tag{6.3f}$$

$$i_{\text{invd},k} = i^{\text{mpc}}_{\text{invd},k} + i^{\text{droop}}_{\text{invd},k} \; \forall \; k \in \Gamma \tag{6.3g}$$

$$i_{\text{invq},k} = i^{\text{mpc}}_{\text{invq},k} + i^{\text{droop}}_{\text{invq},k} \; \forall \; k \in \Gamma \tag{6.3h}$$

$$i^{\text{droop}}_{\text{invd},k} = K_d(v_{\text{ref}} - v_{\text{cd},k}) \; \forall \; k \in \Gamma \tag{6.3i}$$

$$i^{\text{droop}}_{\text{invq},k} = -K_q(v_{\text{ref}} - v_{\text{cd},k}) \; \forall \; k \in \Gamma \tag{6.3j}$$

$$|i^{\text{droop}}_{\text{invd},k}| \leq I_{\text{d},max} \; \forall \; k \in \Gamma \tag{6.3k}$$

$$i^{\text{droop}\;2}_{\text{invd},k} + i^{\text{droop}\;2}_{\text{invq},k} \leq I^2_{max} \; \forall \; k \in \Gamma \tag{6.3l}$$

where matrices $Q = \text{diag}(q_{11}, q_{22}, q_{33})$ and $S = \text{diag}(s_{11}, s_{22})$ represent the respective weights of each term in the cost function. A higher value of q_{11} prioritizes better voltage support, q_{22} prioritizes a better reduction in frequency deviation, and q_{33} prioritizes the reduction in ROCOF. Similarly, s_{11} and s_{22} prioritize minimizing the use of ESS current (d and q components, respectively). Equation (6.3b) represents the state equations for frequency dynamics, (6.3d) represents steady-state voltage behavior, (6.3e) and (6.3f) represent limits on inverter currents, (6.3g) and (6.3h) represent the fact that the total current to the system is the sum of droop and MPC, and (6.3i) and (6.3j) represent

droop. Note that w_d and v_{gdq} have no discrete-time index k. This is because these variables act like disturbances (their dynamics are unknown), and hence, they are assumed to be constant throughout the prediction horizon. The value of $i^{\text{mpc}}_{\text{invdq},q}$ obtained by solving the above optimization problem is used as the control input.

6.6 Simulation Setup

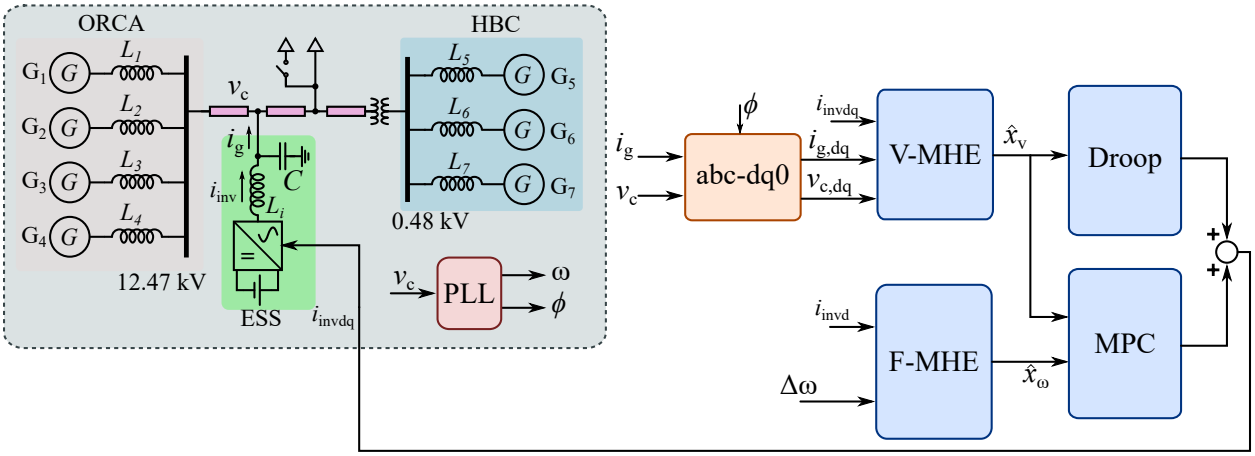

Figure 6.3. Simulation setup for integrated voltage and frequency support using droop and MPC on modified Cordova benchmark.

To assess the performance of the proposed approach, the benchmark described in Chapter 3 is used. The voltage at PCC is used as a reference to transform the voltage and current in abc frame to dq frame. The noise of the same amount used in Chapter 4 was used to emulate real-world scenarios. The state estimates provided by V-MHE and F-MHE (discussed in Chapter 4) are passed to droop and MPC which computes the d and q component of inverter current. The sample time of Droop was set to 0.1 ms and that of MPC was set to 20 ms. The sample time of droop was set based on the time constant of voltage dynamics while that of MPC was set based on the time constant of frequency dynamics which are discussed in Chapter 3. The horizon length of MPC was set to 12 timesteps. The weights of MPC are tuned based on desired performances. The effect of the weight of MPC has been analyzed in the following sections.

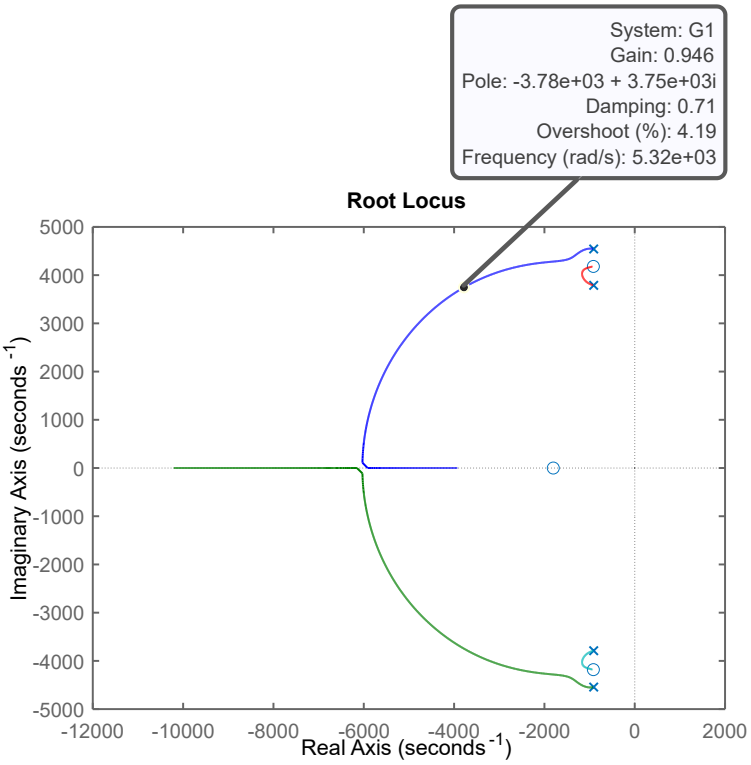

(a) Root-locus of $G_d(s)$

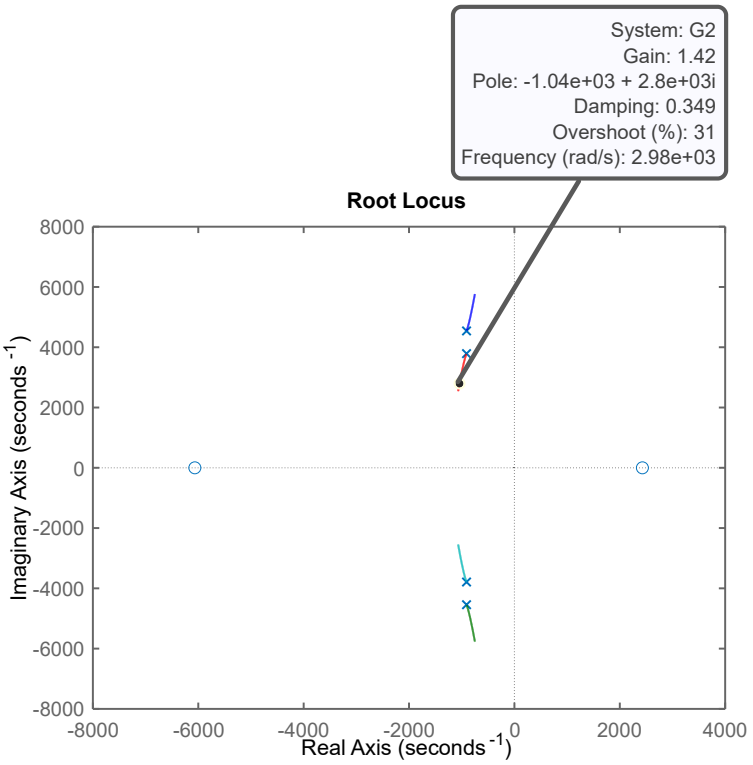

(b) Root-locus of $G_q(s)$

Figure 6.4. Root-locus plot for $G_d(s)$ and $G_q(s)$.

6.7 Results and Analysis

In this section, the performance of the proposed approach is discussed. First, the design of droop based on the root-locus method is presented. Then, the performance of the proposed approach with different weights of MPC is discussed.

6.7.1 Design of Droop

Design of droop using the root-locus method requires obtaining the transfer function of the voltage dynamics. This can be obtained by using the state-space model developed in Chapter 3. The state-space model can be converted to a transfer function as

$$G(s) = C(sI - A)^{-1}B + D. \tag{6.4}$$

The obtained transfer functions are

$$G_d(s) = \frac{6188s^3 + 2.25 \times 10^7 s^2 + 1.339 \times 10^{11} s + 2.046 \times 10^{14}}{s^4 + 3636s^3 + 3.995 \times 10^7 s^2 + 6.663 \times 10^{10} s + 3.259 \times 10^{14}} \tag{6.5}$$

$$G_q(s) = \frac{2.333 \times 10^6 s^2 + 8.483 \times 10^9 s - 3.437 \times 10^{13}}{s^4 + 3636s^3 + 3.995 \times 10^7 s^2 + 6.663 \times 10^{10} s + 3.259 \times 10^{14}} \tag{6.6}$$

where $G_d(s)$ and $G_q(s)$ represents transfer function of voltage with respect to d and q component of inverter current respectively. The root locus of each transfer function was obtained. For each case, the range of gain used was from 0 to 3. The maximum gain of 3 was chosen because it gives maximum ESS current for a typical voltage deviation of 0.1 pu. The result of the root locus is shown in Fig. 6.4. For $G_d(s)$, the damping of around 0.71 was achieved at the gain of 0.946 where the overshoot was 4.19%. For $G_q(s)$, the gain of 1.42 was chosen where damping was found to be 0.349. No better point on the root locus was found, so the gain of 1.42 will be chosen.

6.7.2 Performance of Voltage-Frequency Support

To analyze the performance of the proposed integrated voltage-frequency support approach, the simulation was performed for different values of weight parameters (i.e., q_{11}, q_{22}, and q_{33}). In the first case, frequency support was prioritized over the voltage support by setting

$Q = \text{diag}(0.001, 10.0, 10.0)$. Note that a very small weight for voltage deviation is considered. This is because the magnitude of the voltage deviation is large (about 10 times greater than the frequency deviation). Thus, it is necessary to compensate for that scale as well. In the second case, equal emphasis was placed on both voltage and frequency support by setting $Q = \text{diag}(0.01, 1.0, 1.0)$. The final case prioritized voltage support over frequency support by setting $Q = \text{diag}(0.1, 0.1, 0.1)$. For all three cases, the value of S was set to $\text{diag}(0.01, 0.001)$. This parameter selection assumes that voltage and frequency support have a higher priority over ESS utilization. Furthermore, a larger weight for the d component of the inverter was chosen because active power is more expensive than reactive power. A step load change from 0.3 pu to 0.45 pu at $t = 80$ s was considered for all three cases to analyze the system's response. Fig. 6.5 shows the simulation results for all cases.

In the first case, significant reductions in the frequency deviation and ROCOF are observed (Fig.6.5(d) and (g)). It can be observed that there is only slight improvement in steady-state voltage response (Fig.6.5(a)) because of its lower priority. There is some steady-state voltage deviation, although it is within ±5%. Fig. 6.5(j) shows the d and q components of inverter currents (overall control action of MPC and droop). It can be sees that there is some initial spike. It is because the droop is providing dynamic voltage support, which occurs at a very fast time-scale. Also, it can be observed that a large value of i_{invd} and a small value of i_{invd} are utilized initially. It is because frequency can be supported by i_{invd} only. As the frequency goes to steady state, the magnitude of i_{invd} decreases, and that of i_{invq} increases. Voltage support can be provided by both i_{invd} and i_{invq}, thus their values at steady state are non-zero, although i_{invq} has a larger magnitude because of its smaller weight (s_{22}).

In the second case, priorities for both voltage and frequency support are equal. Here, the frequency deviation and ROCOF (Figs. 6.5(e) and (h)) are larger, but voltage response (Fig. 6.5(b)) is better than in the first case. Fig. 6.5(k) shows the d and q components of inverter currents. It can be observed that the initial spike has the same magnitude as in the first case. It is because the droop coefficient has not changed, and hence, magnitudes of the spike are expected to be the same. Also, the initial magnitude of i_{invd} is smaller than in the first case, but that of i_{invq} is larger. It is

because frequency support is less prioritized, and hence, a smaller magnitude of i_{invd} is sufficient. The reduction in i_{invd} must be compensated by i_{invq} to provide voltage support.

Finally, in the last case, voltage support is largely prioritized over frequency support. In this case, it can be seen that voltage deviation (Fig. 6.5(c)) has been largely reduced, but there is very small to no improvement in the frequency response (Figs. 6.5(f) and (i)). Fig.6.5(l) shows the d and q components of inverter currents. The initial, as well as steady-state value of i_{invd}, is very small compared to i_{invq}. It is because frequency support is no longer a priority, and hence, a large value of i_{invq} is utilized owing to its smaller weight. Results of all cases are summarized in table 6.1 (all quantities are in per unit).

Table 6.1. Summary of the results

Performance metrics	no control	Case I	Case II	Case III
Maximum $\lvert\Delta v_{cd}\rvert$	0.071	0.039	0.039	0.039
Steady state $\lvert\Delta v_{cd}\rvert$ ($\times 10^{-3}$)	8.37	3.07	2.71	1.67
Maximum $\lvert\Delta\omega\rvert$ ($\times 10^{-3}$)	6.2	4.26	5.13	5.68
Maximum $\lvert i_{invd}\rvert$	-	0.07	0.043	0.042
Maximum $\lvert i_{invq}\rvert$	-	0.047	0.049	0.064

6.7.3 Constraints Handling

The proposed approach allows ESS operator to impose constraints on inverter currents (and hence, power) based on available resources, market incentives, etc. For this case, the first case from the previous Subsection is considered. The limits of inverter currents are reduced to 0.02 pu. The performance comparison is shown in the Fig. 6.6. The reduction in frequency and voltage deviation is larger when there is no limits on inverter currents. When limits are imposed, both frequency and voltage deviation increase. These are the tradeoffs: inverter current can be reduced by imposing constraint; however, compromise in voltage and frequency deviation reduction should be expected. These limits can be imposed when limited power for voltage and frequency support is available (remaining power might be required for other grid services). Further, this also helps reduce power/energy usage per voltage/frequency events increasing ESS lifetime.

6.7.4 Computational Performance

The average computation time of the proposed MPC was found to be 0.0237 ms which is significantly smaller than the sample time (20 ms). This shows that the proposed approach is computationally feasible.

6.7.5 Effect of Computational Delay

To assess the effect of computational delay on the voltage support performance, the case from previous subsection is considered. The limits on inverter current are deactivated. The output of MHEs and MPC are delayed by their corresponding computation time. The performance comparison is shown in Fig. 5.9. It can be seen that the voltage and frequency deviation has increased slightly but the difference is very small. This shows that the proposed approach is robust against delay which usually arises in the real world.

6.8 Chapter Conclusions

In this chapter, a control framework for integrated voltage and frequency support was developed. The framework utilized two MHEs developed in Chapter 4. The state estimates from the two MHEs were passed to droop and MPC controller to provide voltage and frequency support. Through simulations perfromed in the test microgrid system, it was illustrated that the proposed droop-MPC approach can provide both voltage and frequency support. Furthermore, the operational flexibility of our approach was also explored by varying weight parameters. These customizable weights allows ESS operator to tailor the strategy based on diverse considerations, such as available power resources and market incentives. It was also shown that the proposed approach could incorporate physical constraints of an ESS (maximum inverter currents). Further, computation time was assessed and the computational delay was introduced to assess the performance of the proposed approach. The effect of computation time on performance was found to be very small. This shows the robustness of the proposed approach under computational delay.

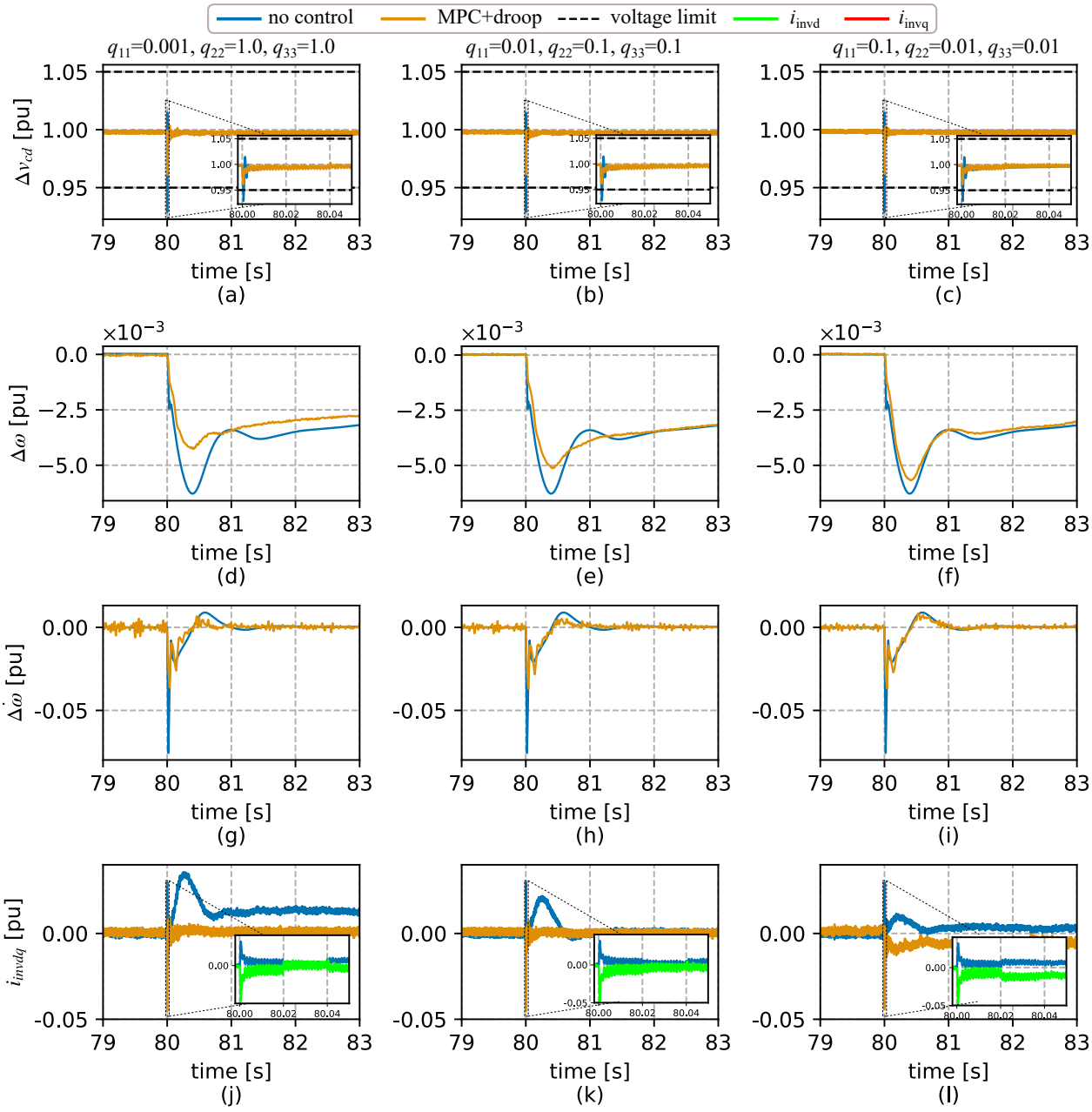

Figure 6.5. Comparison of voltage and frequency support for different cases (different weighting parameters)

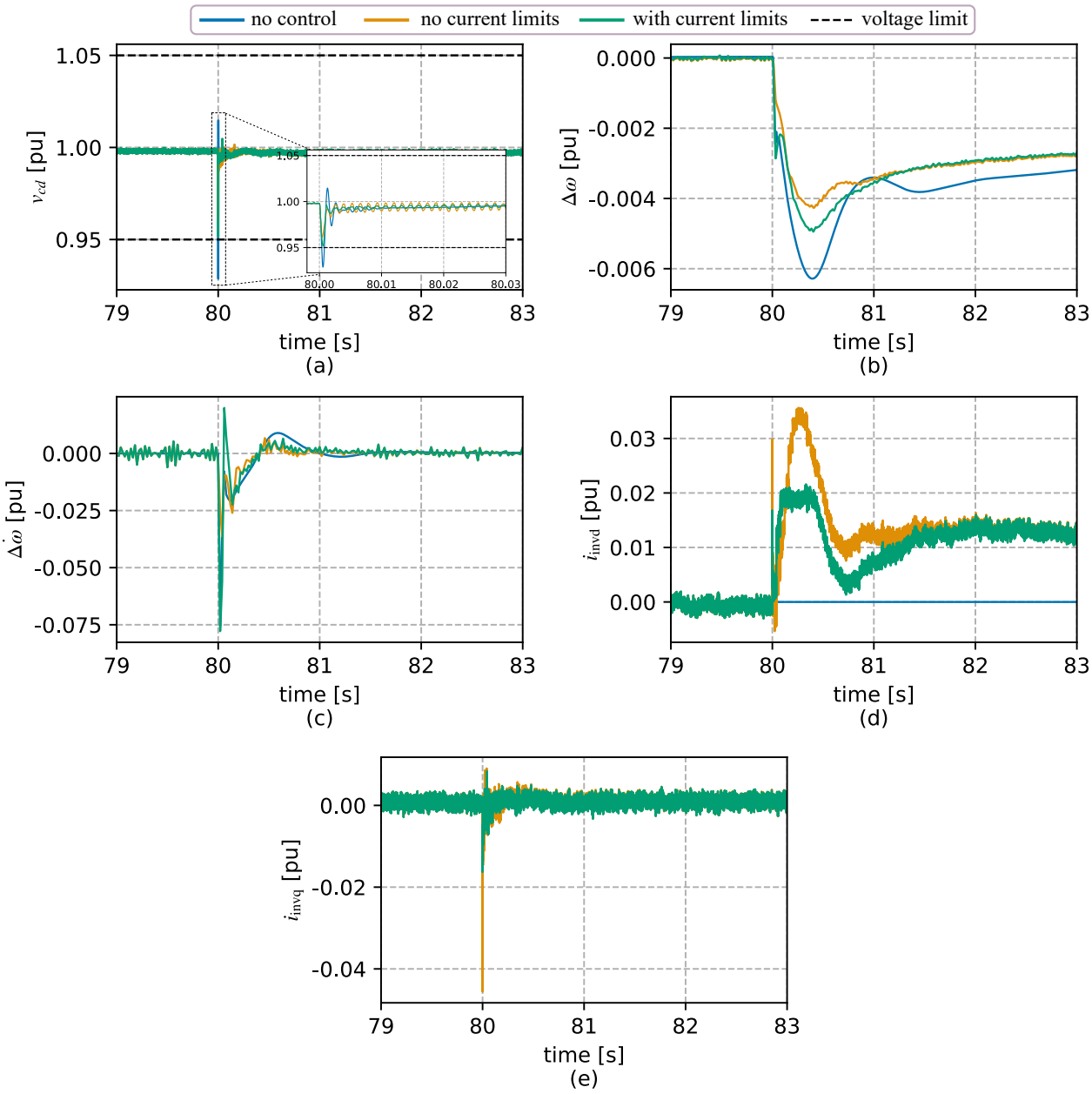

Figure 6.6. Comparison of performance with unconstrained and constrained inverter currents.

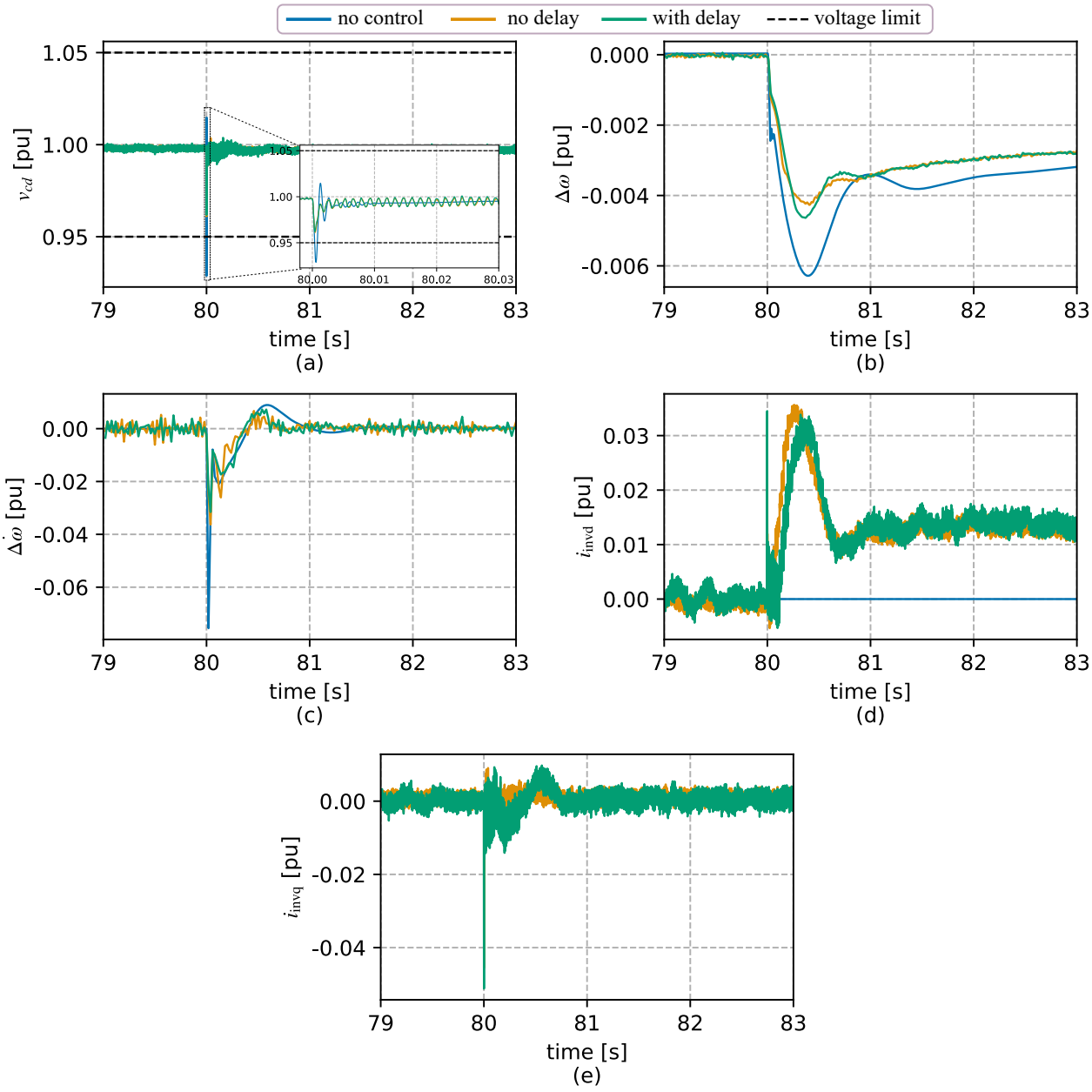

Figure 6.7. Comparison of performance with computational delay.

CHAPTER 7

CONCLUSIONS AND FUTURE RESEARCH DIRECTION

7.1 Conclusions

Microgrids, due to their numerous advantages such as the integration of renewable energy, resilience, autonomous operation, and energy security, have emerged as a promising solution for ensuring the reliability of future power grids. However, unlike traditional power systems that have separate voltage and frequency controllers assuming decoupled dynamics, microgrid systems exhibit a closer coupling between voltage and frequency dynamics.

Microgrids have a high R/X ratio, as they operate at low to medium voltage levels. Due to the coupling between voltage and frequency with active power, the sensitivity of voltage to active power depends on the R/X ratio. Further, because of high R/X, voltage is sensitive to both active and reactive power. In contrast, frequency remains primarily sensitive to variations in active power.

The timescale of voltage dynamics in microgrids is in the range of milliseconds, while that of frequency dynamics is in the range of seconds, representing a significant difference between the two. Therefore, the sample time should be based on the time constant of the voltage dynamics, while the time horizon should be based on the time constant of the frequency dynamics.

Chapter 1 discusses recent voltage and frequency events, as well as trends in microgrids. It also introduces standards concerning Voltage-Frequency limits specific to microgrids, highlighting differences between grid-connected and isolated/islanded configurations. Furthermore, the chapter presents the concept of fast voltage and frequency support using an energy storage system. Given that voltage dynamics occur in the range of milliseconds, the support mechanism should operate within this range. Additionally, recognizing the importance of energy storage systems in voltage support, frequency support, load leveling, etc., the Federal Energy Regulatory Commission (FERC) has issued orders that permit these roles, which are briefly discussed in Chapter 1.

Chapter 2 presents the state-of-the-art in voltage and frequency support, offering a detailed comparison of current approaches in power systems. One of the simplest strategies discussed is droop-based control, which allows for coordination between multiple resources to provide voltage/frequency support. However, this method is noted for its lower precision, reduced system stability, and poor performance when dealing with non-linear and/or asymmetrical loads. Another approach discussed is the PID-based control approach, which offers greater accuracy compared to just proportional or droop control. Additionally, PID control requires fewer computational resources. However, tuning a PID controller for nonlinear systems can be complex and may present adaptability issues. Another approach discussed is reinforcement learning (RL), where the model is trained to make a sequence of decisions. The main advantage of RL is that it doesn't require a model, which is useful when dealing with complex systems. However, the major drawbacks of RL are that it requires a large number of samples to learn effectively and is computationally expensive.

LQR (Linear Quadratic Regulator) and MPC (Model Predictive Control) are model-based control approaches where a cost function is minimized over a finite horizon. LQR is known for its simplicity and computational efficiency. However, it is limited to linear systems and cannot impose constraints. On the other hand, MPC is a more versatile approach as it can handle nonlinear systems and accommodate physical constraints. Also, in Chapter 2, different approaches applied for combined voltage-frequency support are presented.

Control approaches rely on knowing the values of state variables at each timestep, but since not all states are directly measurable, a state estimator is necessary to estimate these states using input and output measurements. State estimators can also be used to estimate parameters. In Chapter 2, various state estimation approaches are discussed. The first approach introduced is the Luenberger observer, which requires a linear model of the system. The Kalman filter (KF) is also discussed as a superior alternative to the Luenberger observer. While the KF is a simple and effective estimator, it does not estimate parameters. Additionally, the chapter covers the Extended Kalman Filter (EKF) and Unscented Kalman Filter (UKF). Furthermore, Chapter 2 introduces a machine learning-based state estimator called the neural state estimator, proposed for estimating the states of power system

frequency dynamics. The estimator is accurate however, it is computationally expensive. The other estimator is MHE which is an optimization-based technique. MHE is superior to KFs in the case of handling nonlinear systems and estimating the states and parameters of the system. A comparative analysis of various Kalman filters and moving horizon estimators for power system frequency dynamics showed that the MHE excels in estimation accuracy when compared to Kalman filters.

Chapter 3 delves into the development of models for voltage and frequency dynamics. The section on voltage dynamics explores the changes in voltage and other state variables over time, particularly focusing on the impact of network dynamics. A Thevenin equivalent model representing the line resistance, inductance, and the Thevenin voltage is described. Additionally, for ESS assumed to be grid-following, the chapter describes their representation using a controlled current source and capacitance as an inverter filter. The chapter extensively covers the modeling and validation processes, including the calculation of time constants for voltage dynamics.

In a parallel manner, the modeling approach for frequency dynamics involves the utilization of an equivalent single-generator model, which effectively represents the behavior of multiple generators within the power system. This model encompasses a swing equation, a fundamental component in power system dynamics that describes the rate of change of rotor angle with respect to time, and a differential equation that characterizes the dynamics of the turbine-governor system. Similar to the voltage dynamics, the frequency dynamics are also modeled and validated. Moreover, the calculation of the time constant associated with frequency dynamics is a critical aspect of this modeling process. The time constant provides insight into the system's response to changes in frequency and helps in understanding the overall stability and performance of the power system under various operating conditions. The chapter concludes by detailing the simulation benchmark employed for the study. It provides a concise overview of the generators involved and their respective parameters.

The rise of converter-based generation in power systems and microgrids is increasing parameter variability and challenging voltage and frequency control. Monitoring system states and parameters

are crucial for stable operation. Robust estimators are needed for noisy conditions and unknown disturbances. Microgrid parameter estimation is vital for optimal voltage and frequency control with DERs, as parameters can change during re-dispatch or reconfiguration. MHE is used here for state and parameter estimation, optimizing system stability by minimizing noise in an online, fixed-past-horizon optimization problem.

Chapter 4 introduces the parameter identifiability analysis developed in Chapter 3 and establishes the necessary criteria for perturbation signals. Furthermore, it elaborates on the Moving Horizon Estimation (MHE) framework for conducting state and parameter estimation, elucidating its working principle and general formulation. The chapter also discusses the incorporation of an arrival cost in the MHE cost function, which aims to approximate the information inherent in the data. Additionally, the chapter emphasizes the importance of proper weight selection for MHE to achieve accurate parameter estimation, providing criteria for this selection process. Lastly, it offers detailed insights into the implementation of the MHE framework.

The simulation setup for estimating both voltage and frequency dynamics, including state and parameter estimation, is meticulously described in this chapter. The results of the simulations are thoroughly analyzed for both cases, showcasing the effectiveness of the proposed approach. Despite the presence of noise in the measurements, the MHE framework demonstrates robust performance, achieving smaller error metrics such as RMSE and NRMSE. This indicates that the MHE approach is capable of providing accurate estimates even in the presence of noisy measurements, highlighting its potential as a reliable tool for state and parameter estimation in power systems and microgrids.

Chapter 5 discusses MHE-MPC based dynamic voltage support approach for microgrid using ESS. The MHE developed in Chapter 4 was used to provide state estimates. These state estimates are passed to MPC which computes the control signal. The ESS injects inverter currents based on the calculated control signal to provide voltage support. The physical constraints (inverter currents) were also discussed. This constraint allows an ESS operator to limit the power usage for voltage support. Further, the effect of the computational delay was also assessed to show the robustness of the proposed approach.

Finally, in Chapter 6 a framework that provides integrated voltage and frequency support is proposed. The framework utilized two MHEs developed in chapter 4 along with droop and MPC. Droop provides dynamic voltage support whereas MPC provides steady state voltage support as well as dynamic frequency support. Droop operates at the timescale of voltage dynamics whereas MPC operates at the timescale of frequency dynamics. The model of the droop is also incorporated inside MPC so that MPC sees the microgrid and droop as a system. The performance of proposed approach was illustrated under different scenarios: different weights of MPC, constraints on the inverter currents, and the presence of computational delay. These scenarios showed that with different values of weights, ESS operator can strike the right balance between performance of voltage/frequency support and ESS utilization. Further, limits on inverter currents can be imposed which is useful when limited power is available for voltage and frequency support. Finally, effect of computational delay was assessed which showed that the effect is very small.

7.2 Future Research Directions

Potential directions for future research include the application of the developed estimation and control framework to a real power system benchmark. The framework could be further extended to accommodate multi-area power systems, which may necessitate modifications to the underlying prediction model of the system.

Additionally, the design of the perturbation signal warrants further investigation. While the evaluation of various perturbation signals has been conducted to identify an effective signal in the literature, it does not guarantee the identification of the optimal perturbation signal. This area could be further explored.

The proposed control approach, encompassing both voltage support and integrated voltage and frequency support, models the ESS as a controlled current source. However, the dynamics of the State of Charge (SoC) and the impedance of the ESS have not been taken into account. The incorporation of these factors could potentially enhance the performance of the proposed approaches.

REFERENCES

[1] Jul 2023. [Online]. Available: https://www.c2es.org/content/microgrids/

[2] M. Farrokhabadi, C. A. Cañizares, and K. Bhattacharya, "Frequency control in isolated/islanded microgrids through voltage regulation," *IEEE Transactions on Smart Grid*, vol. 8, no. 3, pp. 1185–1194, 2015.

[3] G. Delille, L. Capely, D. Souque, and C. Ferrouillat, "Experimental validation of a novel approach to stabilize power system frequency by taking advantage of load voltage sensitivity," in *2015 IEEE Eindhoven PowerTech*, 2015, pp. 1–6.

[4] K. W. Joung, T. Kim, and J. Park, "Decoupled frequency and voltage control for stand-alone microgrid with high renewable penetration," in *IEEE/IAS* 54^{th} *Industrial and Commercial Power Systems Technical Conference (ICPS)*, 2018, 8 pp.

[5] M. Farrokhabadi, C. A. Cañizares, J. W. Simpson-Porco, E. Nasr, L. Fan, P. A. Mendoza-Araya, R. Tonkoski, U. Tamrakar, N. Hatziargyriou, D. Lagos *et al.*, "Microgrid stability definitions, analysis, and examples," *IEEE Transactions on Power Systems*, vol. 35, no. 1, pp. 13–29, 2019.

[6] M. Diaz-Aguiló, J. Sandraz, R. Macwan, F. de León, D. Czarkowski, C. Comack, and D. Wang, "Field-validated load model for the analysis of cvr in distribution secondary networks: Energy conservation," *IEEE Transactions on Power Delivery*, vol. 28, no. 4, pp. 2428–2436, 2013.

[7] R. Tonkoski, D. Turcotte, and T. H. M. EL-Fouly, "Impact of high pv penetration on voltage profiles in residential neighborhoods," *IEEE Transactions on Sustainable Energy*, vol. 3, no. 3, pp. 518–527, 2012.

[8] "Transport chaos across england and wales after major power cuts," Aug 2019. [Online]. Available: https://www.theguardian.com/business/2019/aug/09/power-cut-hits-london-and-south-east-england

[9] R. Yan, N.-A. Masood, T. Kumar Saha, F. Bai, and H. Gu, "The anatomy of the 2016 south australia blackout: A catastrophic event in a high renewable network," *IEEE Transactions on Power Systems*, vol. 33, no. 5, pp. 5374–5388, 2018.

[10] K. Dayton, "Hart agrees to install equipment to mitigate electricity issues," Dec 2021. [Online]. Available: https://www.civilbeat.org/2021/12/hart-agrees-to-install-equipment-to-mitigate-electricity-issues/#:~:text=The%20trains%20may%20cause%20voltage,equipment%20to%20stabilize%20the%20power.

[11] N. Bhujel, U. Tamrakar, T. M. Hansen, R. H. Byrne, and R. Tonkoski, "Optimization-Based Estimation of Microgrid Equivalent Parameters for Voltage and Frequency Dynamics," in *IEEE Powertech*, 2021.

[12] N. Bhujel, A. Rai, T. M. Hansen, R. Tonkoski, and U. Tamrakar, "A model predictive approach for voltage support in microgrids using energy storage systems," in *2021 IEEE Power & Energy Society General Meeting (PESGM)*, 2021, pp. 1–5.

[13] M. Dashtdar, A. Flah, S. M. S. Hosseinimoghadam, and A. El-Fergany, "Frequency control of the islanded microgrid including energy storage using soft computing," *Scientific Reports*, vol. 12, no. 1, p. 20409, Nov 2022. [Online]. Available: https://doi.org/10.1038/s41598-022-24758-6

[14] A. B. Siddique, M. S. Munsi, S. K. Sarker, S. K. Das, and M. R. Islam, "Voltage and current control augmentation of islanded microgrid using multifunction model reference modified adaptive pid controller," *International Journal of Electrical Power & Energy Systems*, vol. 113, pp. 492–501, 2019. [Online]. Available: https://www.sciencedirect.com/science/article/pii/S0142061518336706

[15] J.-F. Toubeau, B. Bakhshideh Zad, M. Hupez, Z. De Greve, and F. Vallee, "Deep reinforcement learning-based voltage control to deal with model uncertainties in distribution networks," *Energies*, vol. 13, no. 15, p. 3928, 2020.

[16] N. Bhujel, A. Rai, U. Tamrakar, Y. Zhu, T. M. Hansen, D. Hummels, and R. Tonkoski, "Soft actor-critic based voltage support for microgrid using energy storage systems," in *2023 IEEE PES Innovative Smart Grid Technologies Latin America (ISGT-LA)*, 2023, pp. 125–129.

[17] M. Adibi and J. van der Woude, "A reinforcement learning approach for frequency control of inverted-based microgrids∗∗this work was supported by the nwo (netherlands organization for scientific research) program uncertainty reduction in smart energy systems (urses) under the support of the project en-bark." *IFAC-PapersOnLine*, vol. 52, no. 4, pp. 111–116, 2019, iFAC Workshop on Control of Smart Grid and Renewable Energy Systems CSGRES 2019. [Online]. Available: https://www.sciencedirect.com/science/article/pii/S2405896319305002

[18] P. Aslami, T. Aryal, N. Bhujel, A. Rai, H. M. Rekabdarkolaee, and T. M. Hansen, "A soft actor-critic approach for power system fast frequency response," in *2023 North American Power Symposium (NAPS)*, 2023, pp. 1–6.

[19] A. Luna, U. Tamrakar, R. Tonkoski, and S. Hietpas, "Linear quadratic regulator controller to improve transient frequency stability through virtual inertia," in *2020 IEEE Power & Energy Society Innovative Smart Grid Technologies Conference (ISGT)*, 2020, pp. 1–5.

[20] A. Sibilska-Mroziewicz, A. Ordys, J. Możaryn, P. Alinaghi Hosseinabadi, A. Soltani Sharif Abadi, and H. Pota, "Lqr and fuzzy logic control for the three-area power system," *Energies*, vol. 14, no. 24, 2021. [Online]. Available: https://www.mdpi.com/1996-1073/14/24/8522

[21] U. Tamrakar, T. M. Hansen, R. Tonkoski, and D. A. Copp, "Model predictive frequency control of low inertia microgrids," in *2019 IEEE 28th International Symposium on Industrial Electronics (ISIE)*, 2019, pp. 2111–2116.

[22] U. Tamrakar, S. Member, D. A. Copp, T. Nguyen, and S. Member, "Optimization-Based Fast-Frequency Estimation and Control of Low-Inertia Microgrids," *IEEE Transactions on Energy Conversion (submitted)*, vol. XX, no. Xx, pp. 1–9, 2020.

[23] M. Ramezani and S. Li, "Voltage and frequency control of islanded microgrid based on combined direct current vector control and droop control," in *IEEE Power and Energy Society General Meeting (PESGM)*, 2016, 5 pp.

[24] M. S. Pilehvar and B. Mirafzal, "Frequency and voltage supports by battery-fed smart inverters in mixed-inertia microgrids," *Electronics*, vol. 9, no. 11, 2020. [Online]. Available: https://www.mdpi.com/2079-9292/9/11/1755

[25] N. Bhujel, U. Tamrakar, T. M. Hansen, R. H. Byrne, and R. Tonkoski, "Model Predictive Integrated Voltage and Frequency Support in Microgrids," in *2020 52nd North American Power Symposium (NAPS)*, 2021, pp. 1–6.

[26] P. Kühl, M. Diehl, T. Kraus, J. P. Schlöder, and H. G. Bock, "A real-time algorithm for moving horizon state and parameter estimation," *Computers and Chemical Engineering*, vol. 35, no. 1, pp. 71–83, 2011.

[27] D. Simon, *Optimal State Estimation: Kalman, H infinity and nonlinear approaches*. Wiley-Interscience, 2006.

[28] B. Poudel, P. Aslami, T. Aryal, N. Bhujel, A. Rai, M. Rauniyar, H. M. Rekabdarkolaee, U. Tamrakar, T. M. Hansen, and R. Tonkoski, "Comparative analysis of state and parameter estimation techniques for power system frequency dynamics," in *2022 International Symposium on Power Electronics, Electrical Drives, Automation and Motion (SPEEDAM)*, 2022, pp. 754–761.

[29] Q. Li, R. Li, K. Ji, and W. Dai, "Kalman filter and its application," in *2015 8th International Conference on Intelligent Networks and Intelligent Systems (ICINIS)*, 2015, pp. 74–77.

[30] A. Rai, N. Bhujel, T. M. Hansen, R. Tonkoski, and U. Tamrakar, "Implementation of model predictive control for frequency support in a real-time digital simulator," in *2022 IEEE Electrical Energy Storage Application and Technologies Conference (EESAT)*, 2022, pp. 1–5.

[31] A. Rai, N. Bhujel, U. Tamrakar, D. Hummels, and R. Tonkoski, "Data-driven model predictive control for fast-frequency support," in *2023 IEEE Energy Conversion Congress and Exposition (ECCE)*, 2023, pp. 222–229.

[32] E. Wan and R. Van Der Merwe, "The unscented Kalman filter for nonlinear estimation," in *Proceedings of the IEEE 2000 Adaptive Systems for Signal Processing, Communications, and Control Symposium (Cat. No.00EX373)*, 2000, pp. 153–158.

[33] N. Bhujel, A. Rai, U. Tamrakar, D. Hummels, and R. Tonkoski, "Neural network-based dynamic state estimation for fast frequency support using energy storage systems," in *2024 IEEE Electrical Energy Storage Applications and Technologies (EESAT)*, 2024.

[34] U. Tamrakar, D. A. Copp, T. A. Nguyen, T. M. Hansen, and R. Tonkoski, "Real-time estimation of microgrid inertia and damping constant," *IEEE Access*, vol. 9, pp. 114 523–114 534, 2021.

[35] A. F. Villaverde, N. D. Evans, M. J. Chappell, and J. R. Banga, "Input-dependent structural identifiability of nonlinear systems," *IEEE Control Systems Letters*, vol. 3, no. 2, pp. 272–277, 2019.

[36] J. V. Frasch, S. Sager, and M. Diehl, "A Parallel Quadratic Programming Method for Dynamic Optimization Problems," *Mathematical Programming Computation*, 2013, (submitted). [Online]. Available: http://www.optimization-online.org/DB_HTML/2013/11/4114.html

[37] M. Tenny and J. Rawlings, "Efficient moving horizon estimation and nonlinear model predictive control," in *Proceedings of the 2002 American Control Conference (IEEE Cat. No.CH37301)*, vol. 6, 2002, pp. 4475–4480 vol.6.

[38] C. C. Qu and J. Hahn, "Computation of arrival cost for moving horizon estimation via unscented Kalman filtering," *Journal of Process Control*, vol. 19, no. 2, pp. 358–363, 2009. [Online]. Available: http://dx.doi.org/10.1016/j.jprocont.2008.04.005

[39] B. J. Odelson, M. R. Rajamani, and J. B. Rawlings, "A new autocovariance least-squares method for estimating noise covariances," *Automatica*, vol. 42, no. 2, pp. 303–308, 2006. [Online]. Available: https://www.sciencedirect.com/science/article/pii/S0005109805003262

[40] J. A. E. Andersson, J. Gillis, G. Horn, J. B. Rawlings, and M. Diehl, "CasADi – A software framework for nonlinear optimization and optimal control," *Mathematical Programming Computation*, vol. 11, no. 1, pp. 1–36, 2019.

[41] C. V. Rao and J. B. Rawlings, "Constrained process monitoring: Moving-horizon approach," *American Institute of Chemical Engineers. AIChE Journal*, vol. 48, no. 1, p. 97, Jan 2002.

[42] Y. Al Jabri, N. Hosseinzadeh, R. Al Abri, and A. Al Hinai, "Voltage stability assessment of a microgrid," in *2015 IEEE 8th GCC Conference & Exhibition*, Feb 2015, pp. 1–6.

[43] F. Katiraei, R. Iravani, N. Hatziargyriou, and A. Dimeas, "Microgrids management," *IEEE power and energy magazine*, vol. 6, no. 3, pp. 54–65, 2008.

[44] S. K. Sarkar, F. R. Badal, S. K. Das, and Y. Miao, "Discrete time model predictive controller design for voltage control of an islanded microgrid," in 3^{rd} *International Conference on Electrical Information and Communication Technology (EICT)*, 2017, 6 pp.

[45] Y. Shan, J. Hu, Z. Li, and J. M. Guerrero, "A model predictive control for renewable energy based AC microgrids without any PID regulators," *IEEE Transactions on Power Electronics*, vol. 33, no. 11, pp. 9122–9126, 2018.

LIST OF PUBLICATIONS DURING PH.D. STUDY

Journals

1. **N. Bhujel**, N. Guruwacharya, U. Tamrakar, T. M. Hansen, R. H. Byrne, D. Hummels, and R. Tonkoski, “Optimization-based Dynamic Voltage Support of Microgrids using Energy Storage Systems," *IEEE Access* [to be submitted].

2. U. Tamrakar, **N. Bhujel**, T. Nguyen, R. H. Byrne, and B. Chalamala, “A Model Predictive Control Framework for Combining Energy Arbitrage and Power Quality Applications from Energy Storage Systems," *IEEE Transactions on Energy Conversion* [submitted].

3. C. Shah, J. D. Vasquez-Plaza, D. D. Campo-Ossa, J. F. Patarroyo-Montenegro, N. Guruwacharya, **N. Bhujel**, R. D. Trevizan, F. A. Rengifo, M. Shirazi, R. Tonkoski, R. Wies, T. M. Hansen, and P. Cicilio, “Review of Dynamic and Transient Modeling of Power Electronic Converters for Converter Dominated Power Systems, ” *IEEE Access*, vol. 9, pp. 82094-82117, 2021, doi: 10.1109/ACCESS.2021.3086420.

Conferences

1. J. D. Vasquez-Plaza, **N. Bhujel**, R. Tonkoski and F. A. Rengifo, "Parameter Identification for Grid Voltage Support Function of Aggregated DER_A Model," *2024 IEEE Industrial Electronics Conference (IECON)*, Chicago, IL, USA, 2024 [submitted].

2. A. Rai, **N. Bhujel**, U. Tamrakar, R. H. Byrne, D. Hummels and R. Tonkoski, "Frequency Security Index-Based State of Health Monitoring of a Microgrid using Energy Storage Systems," *2024 IEEE Symposium on Power Electronics, Electrical Drives, Automation and Motion (SPEEDAM)*, Ischia, Italy, 2024 [accepted].

3. P. Ghimire, S. Poudel, **N. Bhujel**, V. Dhiman, D. Hummels and R. Tonkoski, "Data-Driven Modeling of Commercial Off-the-shelf Photovoltaic Inverters Using Neuromancer," *2024 IEEE Symposium on Power Electronics, Electrical Drives, Automation and Motion (SPEEDAM)*, Ischia, Italy, 2024 [accepted].

4. **N. Bhujel**, A. Rai, U. Tamrakar, D. Hummels and R. Tonkoski, "Integrated Voltage and Frequency Support in Microgrids Using Droop and Model Predictive Control with Energy Storage Systems," *2024 IEEE Symposium on Power Electronics, Electrical Drives, Automation and Motion (SPEEDAM)*, Ischia, Italy, 2024 [accepted].

5. A. Rai, **N. Bhujel**, U. Tamrakar, V. Dhiman, D. Hummels, R. H. Byrne and R. Tonkoski, "A Physics-Informed Neural Network Modeling Approach for Energy Storage-Based Fast Frequency Support in Microgrids," 2024 IEEE Electrical Energy Storage Application and Technologies Conference (EESAT), San Diego, CA, USA, 2024, pp. 1-5, doi: 10.1109/EESAT59125.2024.10471220.

6. **N. Bhujel**, A. Rai, D. Hummels, U. Tamrakar and R. Tonkoski, "Neural Network-Based Dynamic State Estimation for Fast Frequency Support Using Energy Storage Systems," 2024

IEEE Electrical Energy Storage Application and Technologies Conference (EESAT), San Diego, CA, USA, 2024, pp. 1-5, doi: 10.1109/ EESAT59125.2024.10471218.

7. A. Rai, **N. Bhujel**, U. Tamrakar, D. Hummels and R. Tonkoski, "Data-Driven Model Predictive Control for Fast-Frequency Support," *2023 IEEE Energy Conversion Congress and Exposition (ECCE)*, Nashville, TN, USA, 2023, pp. 222-229, doi: 10.1109/ ECCE53617. 2023.10362777.

8. **N. Bhujel**, A. Rai, U. Tamrakar, Y. Zhu, T. M. Hansen, D. Hummels and R. Tonkoski, "Soft Actor-Critic Based Voltage Support for Microgrid Using Energy Storage Systems," *2023 IEEE PES Innovative Smart Grid Technologies Latin America (ISGT-LA)*, San Juan, PR, USA, 2023, pp. 125-129, doi: 10.1109/ISGT-LA56058.2023.10328313.

9. P. Aslami, T. Aryal, **N. Bhujel**, A. Rai, H. M. Rekabdarkolaee and T. M. Hansen, "A Soft Actor-Critic Approach for Power System Fast Frequency Response," *2023 North American Power Symposium (NAPS)*, Asheville, NC, USA, 2023, pp. 1-6, doi: 10.1109/NAPS58826. 2023.10318617.

10. T. Aryal, P. Aslami, **N. Bhujel**, H. M. Rekabdarkolaee, K. Fu and T. M. Hansen, "Application of Neural Ordinary Differential Equations to Power System Frequency Dynamics," *2023 North American Power Symposium (NAPS)*, Asheville, NC, USA, 2023, pp. 1-6, doi: 10.1109/NAPS58826.2023.10318565.

11. A. Rai, **N. Bhujel**, T. M. Hansen, R. Tonkoski and U. Tamrakar, "Implementation of Model Predictive Control for Frequency Support in a Real-time Digital Simulator," *2022 IEEE Electrical Energy Storage Application and Technologies Conference (EESAT)*, Austin, TX, USA, 2022, pp. 1-5, doi: 10.1109/EESAT55007.2022.9998027.

12. B. Poudel, P. Aslami, T. Aryal, **N. Bhujel**, A. Rai, M. Rauniyar, H. M. Rekabdarkolaee, U. Tamrakar, T. M. Hansen, and R. Tonkoski, "Comparative Analysis of State and Parameter Estimation Techniques for Power System Frequency Dynamics," *2022 International Symposium on Power Electronics, Electrical Drives, Automation and Motion (SPEEDAM)*, Sorrento, Italy, 2022, pp. 754-761, doi: 10.1109/SPEEDAM53979.2022.9842272.

13. **N. Bhujel**, A. Rai, U. Tamrakar, T. M. Hansen, and R. Tonkoski, "Identification of Noise Covariances for Voltage Dynamics Estimation in Microgrids," *2022 IEEE Power Energy Society General Meeting (PESGM)*, Denver, CO, USA, 2022, pp. 1-5, doi: 10.1109/PESGM 48719.2022.9916663.

14. N. Guruwacharya, **N. Bhujel**, T. M. Hansen, S. Suryanarayanan, R. Tonkoski, U. Tamrakar, and F. Wilches-Bernal, "Modeling inverters with grid support functions for power system dynamics studies," *2021 IEEE Power Energy Society Innovative Smart Grid Technologies Conference (ISGT)*, Washington, DC, USA, 2021, pp. 1-5, doi: 10.1109/ISGT49243.2021. 9372183.

15. M. Rauniyar, **N. Bhujel**, T. M. Hansen, R. Fourney, H. M. Rekabdarkolaee, R. Tonkoski, P. Cicilio, M. Shirazi, and U. Tamrakar, "Diesel generator model development and validation using moving horizon estimation," *IECON 2021 – 47th Annual Conference of the IEEE*

Industrial Electronics Society, Toronto, ON, Canada, 2021, pp. 1-6, doi: 10.1109/IECON48115.2021.9589981.

16. **N. Bhujel**, T. M. Hansen, R. Tonkoski, U. Tamrakar and R. H. Byrne, "Optimization-Based Estimation of Microgrid Equivalent Parameters for Voltage and Frequency Dynamics," *2021 IEEE Madrid PowerTech*, 2021, pp. 1-6, doi: 10.1109/PowerTech46648.2021.9494858.

17. **N. Bhujel**, A. Rai, T. M. Hansen, R. Tonkoski and U. Tamrakar, "A Model Predictive Approach for Voltage Support in Microgrids using Energy Storage Systems," *2021 IEEE Power & Energy Society General Meeting (PESGM)*, 2021, pp. 1-5, doi: 10.1109/PESGM46819.2021.9638037.

18. **N. Bhujel**, T. M. Hansen, R. Tonkoski, U. Tamrakar and R. H. Byrne, "Model Predictive Integrated Voltage and Frequency Support in Microgrids," *2020 52nd North American Power Symposium (NAPS)*, 2021, pp. 1-6, doi: 10.1109/NAPS50074.2021.9449640.

19. U. Tamrakar, N. Guruwacharya, **N. Bhujel**, F. Wilches-Bernal, T. M. Hansen, and R. Tonkoski, "Inertia estimation in power systems using energy storage and system identification techniques," *2020 International Symposium on Power Electronics, Electrical Drives, Automation and Motion (SPEEDAM)*, Sorrento, Italy, 2020, pp. 577-582, doi: 10.1109/SPEEDAM48782.2020.9161919.

20. N. Guruwacharya, **N. Bhujel**, U. Tamrakar, M. Rauniyar, S. Subedi, S. Berg, T. M. Hansen, and R. Tonkoski, "Data-driven power electronic converter modeling for low inertia power system dynamic studies," *2020 IEEE Power Energy Society General Meeting (PESGM)*, Montreal, QC, Canada, 2020, pp. 1-5, doi: 10.1109/PESGM41954.2020.9281783.

BIOGRAPHY OF THE AUTHOR

Niranjan Bhujel received a B.E. degree in electrical engineering from Tribhuvan University, Nepal, in 2017. Currently, he is a Ph.D. candidate in electrical engineering at the University of Maine at Orono, Maine, USA, and also a year-round intern at Sandia National Laboratories, Albuquerque, New Mexico, USA. His research interests include optimization, control, dynamic state estimation, and machine learning applications for power systems. Niranjan Bhujel is a candidate for the Doctor of Philosophy degree in Electrical Engineering from the University of Maine in May 2024.